

**INSTITUTO TECNOLOGICO Y DE ESTUDIOS  
SUPERIORES DE MONTERREY**

CAMPUS MONTERREY

SCHOOL OF ENGINEERING AND SCIENCES  
GRADUATE PROGRAMS



---

**Advanced Manufacturing Techniques for the Fabrication  
and Surface Modification of Carbon Nanowires**

---

A thesis presented by

Braulio Cárdenas Benítez

Submitted to the

School of Engineering and Sciences

in partial fulfillment of the requirements for the degree of

Master of Science

in

Electronic Systems

Monterrey Nuevo León, November 13<sup>th</sup>, 2017

**Instituto Tecnológico y de Estudios Superiores de Monterrey**

**Campus Monterrey**

**School of Engineering and Sciences**

The committee members, hereby, certify that have read the thesis presented by Braulio Cárdenas Benítez and that it is fully adequate in scope and quality as a partial requirement for the degree of Master of Science in Electronic Systems.

---

**Dr. Sergio Omar Martínez Chapa**  
Tecnológico de Monterrey  
School of Engineering and Sciences  
Principal Advisor

---

**Dr. Israel de León Arizpe**  
Tecnológico de Monterrey  
Committee Member

---

**Dr. Héctor Alán Aguirre Soto**  
Tecnológico de Monterrey  
Committee Member

---

**Dr. Rubén Morales Menéndez**  
Director Nacional de Posgrados  
Tecnológico de Monterrey

Monterrey Nuevo León, November 13<sup>th</sup>, 2017

### Declaration of Authorship

I, Braulio Cárdenas Benítez declare that this thesis titled, ‘Carbon Nanowire Devices for Biosensing Applications’ and the work presented in it are my own. I confirm that:

- This work was done wholly or mainly while in candidature for a research degree at this University.
- Where any part of this thesis has previously been submitted for a degree or any other qualification at this University or any other institution, this has been clearly stated.
- Where I have consulted the published work of others, this is always clearly attributed.
- Where I have quoted from the work of others, the source is always given. With the exception of such quotations, this thesis is entirely my own work.
- I have acknowledged all main sources of help.
- Where the thesis is based on work done by myself jointly with others, I have made clear exactly what was done by others and what I have contributed myself.

---

Braulio Cárdenas Benítez  
Monterrey Nuevo León, November 13<sup>th</sup>, 2017

@2017 by Braulio Cárdenas Benítez  
All rights reserved

## **DEDICATION**

*To Tity, the love of my life. You are the one person that listened to it all, my ups and downs; you understood me and kept my motivation alive, day after day. Tity, it is your unconditional love and support that has made me come this far.*

*To my parents, who believed in me no matter the outcome. Mom, dad, this work is possible because of you, for always telling me to believe in my wildest dreams.*

*To my brother, Aurelio, for all the love and caring. Brother, this is for the bittersweet struggle of building our dreams into a reality.*

## ACKNOWLEDGEMENTS

I would like to thank to my teacher, supervisor, mentor and friend, Prof. Sergio Omar Martínez Chapa for his guidance and knowledgeable advice, both in life and in my career. Under his mentorship I learned the particulars of paper writing, which is an invaluable tool in my scientific career. But most importantly, he welcomed me into his research group, fully believing in my potential to become a scientist and for that I will be forever in his debt.

I would like to express my gratitude to Prof. Marc Madou, one of the most important mentors to my work and career as a scientist. The insightful conversations we had motivated my work and guided it towards completion. I also thank his Bio-MEMS team at University of California, Irvine (UCI), as they helped us solve many challenges we faced in our laboratory at Tecnológico de Monterrey.

I am also thankful to my thesis committee members, Dr. Israel De León Arizpe and Dr. Héctor Álan Aguirre Soto for their contributions to this work. Each of them has not only provided insight and suggestions to this dissertation, but also demonstrated interest in my work. I also thank the former committee member Dr. Hyundoo Hwang for the meetings and scientific discussions we had over my thesis work.

I would also like to thank the people and institutes that made possible my successful work abroad in Germany. In particular, I would like to express my gratitude to Dr. Jean Korvink and Dr. Dario Mager from the Institute of Microstructure Technology (IMT) in Karlsruhe Institute of Technology (KIT), who provided me with support, funding and scientific guidance. I also thank Dr. Swati Sharma from IMT and her graduate student Nayancee Pandey for helping me complete my experimental work.

I would like to acknowledge the experimental work performed in the cleanrooms of the Light Technology Institute (LTI), under the supervision of Dr. Uli Lemmer. I appreciate the support and mentoring that Dr. Carsten Eschenbaum, from LTI, gave towards the completion of my objectives and experiments; I also thank his Ph.D. student Anne Habermehl that cheerfully gave some of her time to aid me in my lab work and made me feel welcomed at Germany.

I would also like to acknowledge the support from Tecnológico de Monterrey and CONACyT (tuiton and living expenses). I also thank Regina Elizabeth Vargas from CIDyT, for the countless hours she helped me with sample characterization.

I am very grateful to my friends and coworkers from the Sensors and Devices research group at Tecnológico de Monterrey, for the incredibly collaborative atmosphere that they have created. I am particularly grateful with Dr. Samira Hosseini for her friendship, advice and mentoring on my career as a scientist. Her teachings go from insight on scientific writing and experimentation, to tips and little tricks in the graduate student life, which are all invaluable to me. I also thank all of my friends from the group, Mario, Sergio, Adrián, Ezequías, Binny, Rute, Lorena, Mehdi, Omar, Bidhan, Matías, Víctor and José Manuel. For your friendship and help, the lunch time talks, the laughs and the joy.

I am especially thankful to Ricardo, Andrés, Martín and Arnoldo, not only for their patience and friendship, but also for the endless hours they gave helping me in the lab which were key in the successful completion of this project.

Finally, I would like to thank my family, who always believed in me. My mom, my dad and my Brother have not the slightest doubt in their minds that I am capable of achieving something big in life, even when I myself have doubted it. I am grateful for their love, caring and patience even in the hardest and restless nights. They always encourage me to following my dreams, and that feeling will always be dear to me.

And last, but certainly not least, thanks to the love of my life, Tity. She always looked after me and continually cheered me up during the long and tiring hours of writing and work. She has made my life brighter, even when challenges seemed too stiff to overcome. Tity, you are my motivation, you celebrate me even when the littlest of things go right and whenever I need you, you are always there for me.

# **Advanced Manufacturing Techniques for the Fabrication and Surface Modification of Carbon Nanowires**

by

Braulio Cárdenas Benítez

## **ABSTRACT**

Over the last couple of decades, Carbon Nanowires (CNWs) have found important applications in the field of rapid label-free biosensing platforms for their excellent electrical, thermal and chemical properties. Despite the growing interest in incorporating these materials into sensitive analytical devices, there has been limited research efforts that explore the realistic incorporation of these structures into broader microsystems. The present dissertation explores two Advanced Additive Manufacturing (AdAM) techniques for the fabrication of CNWs with promising characteristics for sensing applications. The first technique, Electro-Mechanical Spinning (EMS) is a relatively new method for the production of CNWs with highly-oriented patterning capabilities, and is assessed in terms of the minimum feature sizes that it can attain reproducibly. The second method, Multiple Photon Polymerization (MPP) is a mature laser manufacturing technique that offers high repeatability, yet it has remained largely unexplored in the field of carbon materials. This work presents a study of how MPP can be used to create CNWs in terms of micro-fabrication parameters like laser power and scanning velocity. A thorough review study of the surface properties required for carbon materials to become eligible candidates in biosensing is also included in this dissertation. Lastly, an application of CNWs is presented, in which a Joule Heating technique is used to induce controlled breaking of the wires to produce nano-scale separated carbon electrodes, which hold potential for micro/nano particle manipulation in microfluidics.

## LIST OF FIGURES

FIGURE 1-1. IMPEDANCE NANOWIRE BIOSENSOR STRUCTURE ACTING AS A HIGHLY SENSITIVE DEVICE. THE NANOMATERIAL PROVIDES THE INTERFACE AT WHICH A RECOGNITION COMPONENT (SUCH AS AN ANTIBODY) IS LINKED. SUBSEQUENTLY, THE PRESENCE OF AN ANALYTE WILL TRIGGER A SIGNAL THAT CHANGES THE OVERALL CONDUCTANCE OF THE CHANNEL, REVEALING ITS PRESENCE.....	17
FIGURE 2-1. THE C-MEMS TECHNOLOGY MANUFACTURING PROCESS BEGINS WITH (I) COATING OF A POLYMER UNTO A SUBSTRATE, FOLLOWED BY (II) PATTERNING WITH UV-EXPOSURE PHOTOLITHOGRAPHY. (III) AFTERWARDS, FEATURES ARE DEVELOPED WITH A SOLVENT; (IV) SUBSEQUENTLY, THEY ARE CARBONIZED IN A PYROLYSIS FURNACE AT HIGH TEMPERATURES (900°C) AND AN INERT ENVIRONMENT. (BOTTOM, A) PATTERNED SU-8 PHOTORESIST (POLYMER) STRUCTURES BEFORE CARBONIZATION. (B) THE SAME STRUCTURES, AFTER THE CARBONIZATION STEP, FEATURING CONFORMAL SHRINKAGE IN POST HEIGHT AND DIAMETER. IMAGES ADAPTED FROM REF. [62] R. SRIKANTH, ET AL., J. ELECTROCHEM. SOC., 147.1, 2000, 277-282.....	25
FIGURE 2-2. (A-B) "MASK 1": SIX-ELECTRODE MASK DESIGN FOR PHOTOLITHOGRAPHY USED IN THE FABRICATION OF THE C-MEMS STRUCTURES. THE LOWER LEFT CORNER SHOWS A CODE THAT INDICATES THE SEPARATION BETWEEN THE ELECTRODES (20 AND 40MM, RESPECTIVELY). (C-D) "MASK 2": FOUR-ELECTRODE MASK DESIGN, WHERE TWO OF THE ELECTRODES HAVE BEEN REPLACED BY A SINGLE REFERENCE ELECTRODE. SEPARATIONS OF (C) 20 AND (D) 40MM. ....	27
FIGURE 2-3. TWO VIEWS OF THE RESULTING PATTERNED PHOTORESIST USING "MASK 1" FROM FIGURE 2-2(A-B). AS SEEN IN THE IMAGE, SU-8 PHOTOLITHOGRAPHY ALLOWS WAFER SCALE PRODUCTION OF MICROELECTRODES.....	28
FIGURE 2-4 PLOTTING OF THE PYROLYSIS SET TEMPERATURE AGAINST TIME IN MINUTES (DWELL TIMES: $\Delta t_1 = \Delta t_2 = 60$ MIN). THE FILLED PORTION OF THE PLOT INDICATES THE PARTS OF THE PROCESS IN WHICH HEAT CONTROL WAS APPLIED BY THE AUTOMATED FURNACE. NOTE THAT THE FINAL RAMP GOING DOWN IS JUST AN INDICATION OF WHAT THE TEMPERATURE OF THE FURNACE SHOULD BE. NONETHELESS, THE FURNACE IS COOLED DOWN NATURALLY, AND THUS, COOLDOWN COULD TAKE SLIGHTLY LONGER TIME IN PRACTICE.....	30
FIGURE 2-5. (A) CARBON MICRO-ELECTRODES OBTAINED FROM PYROLYSIS AT 900°C OF DESIGN "MASK 1". (B) EDS SPECTRUM ANALYSIS OF ELECTRODE NUMBER 3 IN (A). SPECTRUM IS PRESENTED IN THE RANGE OF 0.1 TO 1 KEV, SHOWING PEAKS CORRESPONDING TO CARBON AND OXYGEN. THE INSET TABLE SHOWS THE ATOMIC PERCENTAGE MEASURED FROM THE SPECTRUM IN (B)......	31
FIGURE 3-1.COMPARISON OF THE TWO REGIMES UNDER WHICH ELECTROSPINNING OCCURS, SHOWING THE BASIC COMPONENTS: DISPENSING NEEDLE, POLYMER SOLUTION AND COLLECTOR OR TARGET. CLOSE TO THE ELECTROSPUN JET, THE FLOW IS OHMIC AND IS SLOWLY ACCELERATED, RESULTING IN NO BENDING INSTABILITIES (NEAR FIELD ELECTRO-SPINNING, NFES). ON THE CONTRARY, FAR FROM THE NEEDLE THE FLOW IS CONVECTIVE AND IS DOMINATED BY RAPID ACCELERATION WHICH LEADS TO EARNSHAW INSTABILITIES (FAR-FIELD ES, FFES)......	34
FIGURE 3-2. THE DIFFERENT KINDS OF CARBON NANOWIRES. (A,D) SINGLE WALLED CARBON NANOTUBES (SWCNTs), SHOWING THE SEAMLESSLY ROLLED GRAPHENE SHEET IN A CYLINDRICAL CONFIGURATION; IN (A) A SCANNING TUNNELING MICROSCOPY (STM) MICROGRAPH OF AN INDIVIDUAL SWCNT IS SHOWN, WHILE (D) SHOWS THE SCANNING ELECTRON MICROSCOPY (SEM) IMAGE OF THE NANOTUBE. (B) THREE-DIMENSIONAL REPRESENTATION OF THE MULTIPLE GRAPHENE SHEETS EXISTING IN MULTI-WALLED CARBON NANOTUBES (MWCNTs), ALONG WITH A HIGH-RESOLUTION TRANSMISSION ELECTRON MICROSCOPY (HR-TEM) IMAGING OF THE NANOTUBE. (C,F) HR-TEM AND SEM IMAGES OF A SUSPENDED CARBON NANOFIBER. THE TERM CARBON NANOWIRE (CNW) HAS ALSO BEEN USED IN THE LITERATURE. REPRINTED FROM REF [76]., W. ODOM ET AL., J. PHYS. CONDENS. MATTER., 14, 2002, R145-R167. ....	35
FIGURE 3-3. (A) ELECTROSPUN PHOTORESIST (SU-8 2100) ON A FLAT COLLECTOR PLATE WITH TWO DIFFERENT SOLUTION CONCENTRATIONS (IN CYCLOPENTANONE) AND THREE DIFFERENT SPINNING VOLTAGES (9kV, 10kV AND 15 kV). (B) PATTERNING OF A RANDOMLY DEPOSITED NANOFIBER MAT BY EXPOSING SAMPLE TO UV LIGHT AND SUBSEQUENT DEVELOPING. REPRINTED FROM REF. <sup>79</sup> , STEACH, J. K. ET AL., J. APPL. POLYM. SCI., 118, 2010, 405-412.....	37
FIGURE 3-4. (A-H) SUSPENDED CNFs PRODUCED BY PYROLYSIS OF SU-8 POLYMERIC NANOFIBERS PRODUCED BY FFES DIRECTLY ON C-MEMS ELECTRODES. RAMAN SPECTRA OF (I) SU-8 DERIVED CNFs AND (J) PAN DERIVED CNFs. REPRINTED AND ADAPTED FROM REF. <sup>84</sup> , SHARMA, C. S. ET AL., CARBON N. Y., 49, 2011, 1727-32.....	42
FIGURE 3-5. SUSPENDED CNFs DERIVED FROM PYROLYSIS OF PFA PRODUCED POROUS ALUMINA, TEMPLATE TECHNIQUES. (A) CNF SUSPENDED BETWEEN METALLIC CONTACTS. (B) DIFFRACTION PATTERN OF THE CNF. (C,D) TEM MICROGRAPH SHOWING THE DIMENSIONS AND CRYSTALLITE SIZE PRESENT IN HIGHLY AMORPHOUS CNFs. REPRINTED AND ADAPTED FROM REF [56]., B. A. SAMUEL. ET AL., NANOTECHNOLOGY, 19, 2008, 275702. ....	43

FIGURE 3-6. FFES ON A ROTATING DRUM COLLECTOR, WHICH CAN BE USED TO SIMULTANEOUSLY ALIGN AND STRETCH POLYMER NANOFIBERS. ROTATING DRUM SCHEMATIC ADAPTED FROM REF. [39] W. S. LEE ET AL., ACS APPL. MATER. INTERFACES, 2014, 6, 12189–12195. THE SEM MICROGRAPH OF CNW WAS OBTAINED FROM REF. [3] S. SHARMA, ET AL., ACS APPL. MATER. INTERFACES, 2012, 4, 34–39.....	44
FIGURE 3-7. (A-D) HR-TEM IMAGES OF CNFs FABRICATED BY USING A ROTATING DRUM COLLECTOR, SHOWING AN INCREASED GRAPHITIC CONTENT. IN FIGURE (E), THE RAMAN SPECTRA OF SUCH CNFs IS SHOWN, AS WELL AS THEIR X-RAY DIFFRACTION PATTERN IN (F). REPRINTED AND ADAPTED FROM REF. [3], SHARMA, S. ET AL., ACS APPL. MATER. INTERFACES., 4, 2012, 34-39.....	45
FIGURE 3-8. POLYMER MACHINING OF SU-8 WIRES THROUGH EMS TO PRODUCE CNF ARRAYS. (A) DEPOSITION AND PATTERNING OF SU-8. (B) SEM IMAGING OF THE OBTAINED CNWs AFTER CARBONIZATION AT 900°C.....	46
FIGURE 3-9. (TOP, A) SINGLE SUSPENDED SU-8 2000 NANOWIRE STRUCTURE BEFORE PYROLYSIS; (INSET) ANCHORING POINT OF THE NANOWIRE TO THE SUPPORTING WALL. (TOP, B) SINGLE SUSPENDED CNW, AFTER PYROLYSIS; (INSET) BENDING OF THE ANCHORING POINT TO THE SUPPORTING WALL DUE TO ISOMETRIC SHRINKAGE DURING PYROLYSIS. (TOP, C) EXAMPLE OF ELECTRODE STRUCTURES WITH TWO-STEP LITHOGRAPHY PHOTO-PATTERND NANOWIRE NETWORK. (BOTTOM, A) TEM OF A CARBON NANOWIRE AND (BOTTOM, B) CORRESPONDING DIFFRACTION PATTERN. (BOTTOM, C) RAMAN SPECTRUM FROM A CARBON POST, SHOWING ITS GLASSY CARBON COMPOSITION. REPRINTED FROM REF. <sup>38</sup> , LIM, Y. ET AL., NANOSCALE RES. LETT., 8, 2013, 1-9.....	47
FIGURE 3-10. (A) TGA ANALYSIS OF SU-8 AND POLYMIDE C-MEMS PRECURSORS. HR-TEM MICROGRAPH OF (B) SU-8-DERIVED AND (C) POLYMIDE-DERIVED C-MEMS STRUCTURES. REPRINTED AND ADAPTED FROM REF. <sup>103</sup> , SINGH A. ET AL., J. ELECTROCHEM. SOC., 149, 2002, E78-E83.....	49
FIGURE 3-11. SCHEMATIC REPRESENTATION OF THE DEPOSITION PROCESS IN EMS. (A) PATH TAKEN BY THE DEPOSITION NEEDLE RELATIVE TO THE SAMPLE, PORTRAYING A HOVERING SECTION (NO DEPOSITION), CONTACTING POINTS (WHERE THE NEEDLE COMES IN CONTACT WITH THE SAMPLE) AND A DEPOSITION SEGMENT (WHERE THE NANOFIBER IS DEPOSITED). (B) RESULTING SU-8 NANOFIBER FROM (A). (C) CARBONIZED SAMPLE AFTER PYROLYSIS, SHOWING THE POSITION OF THE CNW WITH RESPECT TO THE DEVICE.....	52
FIGURE 3-12. TOP VIEW SEM MICROGRAPHS OF SU-8 FIBERS DEPOSITED ON TOP OF SU-8 MICROSTRUCTURES. (A) SU-8 MICROFIBER DEPOSITED USING “METHOD 1”. (B) SU-8 NANOFIBER DEPOSITED USING “METHOD 2”. (C) DIAMETER PROFILE FOR SU-8 MICROFIBER PRODUCED BY “METHOD 1”. (D) DIAMETER PROFILE FOR SU-8 MICROFIBER PRODUCED BY “METHOD 2”.....	54
FIGURE 3-13. BAR PLOT: DIAMETER REDUCTION OF SU-8 NANOFIBERS PRODUCED BY “METHOD 1”, AS A FUNCTION OF SOFT-BAKE TIME (AT 70°C). (I) AS-DEPOSITED FIBER AT SOFT-BAKE TIME OF 0 S; THE IMAGE WAS RECORDED WITH AN OPTICAL MICROSCOPE AT A MAGNIFICATION OF 200X. (II-V) TIME SEQUENCE OF THE SAME NANOFIBER, SHOWING THE EVOLUTION OF FIBER DIAMETER. ALTHOUGH IT MAY SEEM THAT THERE ARE TWO FIBERS SUSPENDED, THE “SECOND FIBER” IS A REFLECTION ON THE REFLECTIVE SILICON SUBSTRATE. ALL SCALE BARS ARE EQUAL TO 40MM.....	55
FIGURE 3-14. SEM MICROGRAPHS OF SU-8 NANOFIBERS AFTER SOFT-BAKE TREATMENT AT 70°C. (A) MICROGRAPH OF A FIBER SAMPLE THAT IS SUSPENDED IN BETWEEN TWO SU-8 ELECTRODE STRUCTURES (D = 224 NM, SOFT-BAKE TIME: 150s). (B) ZOOMED PORTION OF A NANOFIBER, SHOWING A COLLAPSED END (D = 105 NM, SOFT-BAKE TIME: 180s). (C) FIBER SAMPLE SHOWING BEADS THAT REMAINED EVEN AFTER SOFT-BAKE (D = 270 NM, SOFT-BAKE TIME: 150s). (D) A SAMPLE FIBER THAT COLLAPSED AFTER PROLONGED EXPOSURE TO ELECTRON BEAM (5kV).....	56
FIGURE 3-15. (A) SEM MICROGRAPH (TOP VIEW) OF A PYROLYZED CNW; INSET: ZOOMED PORTION OF THE CNW, WITH A MARK INDICATING THE DIAMETER OF THE SAMPLE. (B) I-V CURVE OF FOUR CNW SAMPLES OF DIFFERENT DIAMETERS; THE CORRESPONDING RESISTANCES ARE 1.727MΩ, 1.371MΩ, 0.731MΩ AND 0.407MΩ, FOR D = 170 NM, 209 NM, 265 NM AND 303 NM, RESPECTIVELY. (C) DIAMETER DISTRIBUTION OF 30 CNW SAMPLES, WITH MEAN 204 NM AND STANDARD DEVIATION OF 41 NM. (D) RESISTANCE DISTRIBUTION OF 64 SAMPLES, WITH MEAN 1.244 MΩ AND STANDARD DEVIATION OF 1.268MΩ.....	58
FIGURE 4-1. TYPES OF PHOTONIC CRYSTALS THAT HAVE BEEN FABRICATED BY MPP. FROM TOP-MOST IMAGE AND IN CLOCKWISE ORDER: SLANTED PORE, SQUARE SPIRAL, CHIRAL, QUASICRYSTAL, ROUND SPIRAL AND WOODPILE CRYSTAL STRUCTURES. ALL SEM IMAGES WERE ADAPTED FROM SEVERAL SOURCES REFERENCED WITHIN THE TEXT [109–117].....	62
FIGURE 4-2. OVERALL MPP FABRICATION SCHEME. (A) A TIGHTLY FOCUSED LASER BEAM (NEAR INFRARED LIGHT) IS ILLUMINATED INTO A PHOTOSENSITIVE RESIN AND THE FOCUS SPOT IS MOVED RELATIVE TO THE SCANNING STAGE TO FABRICATE A FULLY 3D SUSPENDED STRUCTURE. (B,C) AN EXAMPLE STRUCTURE, WHICH ILLUSTRATES THE 3D WRITING CAPABILITIES OF MPP. ADAPTED FROM REF. [125] S. USHIBA ET AL., ADV. MATER., 2014, 26, 5653–5657.....	63

FIGURE 4-3. LIGHT INTENSITY DISTRIBUTION (NORMALIZED) SHOWING THE AIRY PATTERN IN THE (A) X-Y PLANE AND (B) X-Z PLANE. (C) THE INTENSITY PROFILE OF (A) FOR A FIXED Y = 0. (D) PROFILE SHOWN IN (B) FOR Z = 0, WHERE CLEARLY THE WAIST IS BIGGER (3 TIMES MORE) THAN THAT OF CASE (B). PLOTS IN (C) WHERE OBTAINED WITH $\Lambda = 780\text{NM}$ AND NA = 1.4. REPRINTED FROM REF [48], T. BALDACCHINI, THREE-DIMENSIONAL MICROFABRICATION USING TWO-PHOTON POLYMERIZATION, 2015, VOL. 1542.	64
FIGURE 4-4. EXPOSURE REGION EXPERIENCED BY THE PHOTORESIST FOR THE CASE OF ONE-PHOTON POLYMERIZATION (1PP) AT THE LEFT AXIS AND 2PP AT THE RIGHT AXIS. NOTICE THAT THE 2PP POLYMERIZATION THRESHOLD HAS A LOWER LINewidth THAN THE 1PP CASE. REPRINTED FROM REF [48], T. BALDACCHINI, THREE-DIMENSIONAL MICROFABRICATION USING TWO-PHOTON POLYMERIZATION, 2015, VOL. 1542.	65
FIGURE 4-5. SIMPLIFIED SCHEME FOR A PULSE TRAIN, ILLUSTRATING THE PULSE DURATION $T_L$ , REPETITION RATE N, PEAK POWER PPEAK AND ENERGY PER PULSE E.	73
FIGURE 4-6. TRAVELING GAUSSIAN PROFILE REPRESENTING THE MAGNITUDE OF THE PHOTON FLUX, WITH MOVEMENT IN THE Y-AXIS FOR THREE DIFFERENT TIMES OF EXPOSURE. THE POINT OF OBSERVATION CORRESPONDS TO X = 0, Y = 0. AXIS ARE NOT TO SCALE. ADAPTED FROM THESIS DISSERTATION IN REF. [140] C. ESCHENBAUM, 2016.	74
FIGURE 4-7. THEORETICAL VOXEL DIAMETER FOR DIFFERENT VALUES OF PT FOR THE MATERIAL SU-8 2050. (A) DIAMETER OF VOXEL IN THE CASE OF DIRECT EXPOSURE; DOSAGE IS GIVEN BY $D_{VOXEL} = NT_L t \exp{Pt^2}$ . (B) DIAMETER OF VOXEL IN THE CASE OF SCANNING CONFIGURATION; DOSE IS GIVEN BY $D_{LINE} = NT_L t w_0^2 v_y P t^2$ . ADAPTED FROM THESIS DISSERTATION IN REF. [140] C. ESCHENBAUM, 2016.	76
FIGURE 4-8. TPP VERTICAL EXPOSURE SETUP. (I) MICROSCOPE OBJECTIVE (M.O.) WAS DIRECTLY COUPLED TO THE SU-8 2050 FILM USING AN IMMERSION OIL (NA = 1.4). IN ORDER TO FIX STRUCTURES TO THE SUBSTRATE, EXPOSURE WAS STARTED AT THE SU-8/Si INTERFACE. (II) AFTER DEVELOPMENT, THE UNEXPOSED PHOTORESIST IS REMOVED AND ONLY VOXEls REMAIN. (INSET) AN OPTICAL MICROSCOPE IMAGE OF A DOSAGE TEST PERFORMED ON A SILICON SUBSTRATE, FEATURING LINES OF INDIVIDUAL VOXEls PRODUCED WITH DIFFERENT EXPOSURE TIMES.	78
FIGURE 4-9. A) SCHEMATIC REPRESENTATION OF THE EXPERIMENTAL PROCESS VARIABLES USED TO PRODUCE TPP SUSPENDED WIRE STRUCTURES. THE AVERAGE POWER USED TO FABRICATE THE STRUCTURES VARIED FROM 0.2 MW TO 3MW AND SCANNING VELOCITY SPANNED THE RANGE 0.2 TO 2 MM/S. B) SEM MICROGRAPH (TOP VIEW) OF TWO PAIRS OF POSTS, FEATURING THE SUSPENDED WIRES.	79
FIGURE 4-10. INTERFACE SEARCHING PROCEDURE. (A,B) AUTOFLUORESCENCE INTENSITY PROFILE AND CAMERA IMAGE AT THE IMMERSION OIL PHASE, BEFORE DESCENDING THE FOCUS INTO THE PHOTORESIST MATERIAL. LASER POWER WAS SET TO 0.8MW IN ORDER TO ACHIEVE AUTOFLUORESCENCE. (C,D) AN AUTOFLUORESCENCE PEAK IS DETECTED, BUT IT IS STILL NOT COMPLETELY RESOLVABLE FROM BACKGROUND NOISE. (E,F) A WELL-DEFINED FLUORESCENT INTENSITY PEAK EMERGES WHEN THE FOCUS SPOT IS WITHIN THE PHOTORESIST FILM ( $\sim 1$ TO $2\mu\text{M}$ WITHIN THE MATERIAL). ADAPTED FROM REF. [142]. T. WOGGON, 2011.	79
FIGURE 4-11. (A) SEM MICROGRAPH OF A TPP TEST FIELD, SHOWING THE DOSAGE THRESHOLD REQUIRED FOR FABRICATION OF STABLE (NON-COLLAPSED) SUSPENDED SU-8 WIRES (BLURRED LINES ARE DUE TO INSUFFICIENT CONDUCTIVITY DURING IMAGING IN SEM). (I) TYPICAL MICROGRAPH OF PHOTORESIST WIRES BEFORE PYROLYSIS (FABRICATED WITH P = 3.0MW). (II) THE PHOTORESIST WIRES AFTER PYROLYSIS, FEATURING VOLUMETRIC SHRINKAGE AND STRAIGHTENING OF WIRES INTO CNWs. SCALE BARS ARE A) $10\mu\text{M}$ , I) $5\mu\text{M}$ AND II) $5\mu\text{M}$ .	81
FIGURE 4-12. (A) EXPERIMENTALLY OBTAINED WIRE DIAMETER RESULTED FROM TPP AND PYROLYSIS OF TPP STRUCTURES. (B) PERCENTAGE OF DIAMETER SHRINKAGE IN TPP STRUCTURES AFTER PYROLYSIS. THE CURVE DENOTES A MODEL FITTING BASED ON THE THEORETICAL VOXEL LINewidth RESOLUTION.	82
FIGURE 4-13. SEM MICROGRAPHS OF CNWs FABRICATED BY PYROLYSIS OF TPP STRUCTURES. (A) GLASSY CARBON POSTS WITH A SUSPENDED CNW IN BETWEEN THE STRUCTURES; FABRICATION PARAMETERS: $V = 0.2\text{ MM/S}$ , $P = 1.4\text{ MW}$ . (B-D) TEST FIELDS OF CNWs FABRICATED AT DIFFERENT AVERAGE LASER POWER AND VELOCITIES (IN STEPS OF $0.1\text{ MM/S}$ , INDICATED BY ARROW).	83
FIGURE 4-14. DEPENDENCE OF THE DIAMETER (LINewidth RESOLUTION) OF PYROLYZED CNWs AS A FUNCTION OF FABRICATION PARAMETERS (SCAN VELOCITY AND AVERAGE POWER).	84
FIGURE 5-1. EXAMPLES OF DESIRABLE CHEMICAL FUNCTIONALITIES FOR BIOSENSOR APPLICATIONS, PORTRAYING CARBOXYL, AMINE AND HYDROXYL GROUPS.	89
FIGURE 5-2. EFFECT OF THE DISTRIBUTION OF FUNCTIONALITIES ON THE BIOACTIVITY OF THE BIORECEPTOR INTERFACE. (A) FEW FUNCTIONALITIES RESULT IN ACTIVITY LOSS WHEN ANTIBODIES DIRECTLY ENCOUNTER THE SUBSTRATE. (B) CROWDED FUNCTIONALITIES IN THE SURFACE INDUCE STERIC REPULSION THAT PREVENTS POSSIBLE ANTIBODIES FROM MEETING THEIR	

RESPECTIVE BONDING SITES, RESULTING IN ACTIVITY LOSS. (C) EVENLY-SPACED FUNCTIONALITIES YIELDS AN OPTIMAL CONFIGURATION OF ACTIVE ANTIBODIES IN THE BIORECEPTOR INTERFACE.....	90
FIGURE 5-3. EDC/SULFO-NHS PROTOCOL FOR THE IMMOBILIZATION OF BIOMOLECULES WITH AMINE TERMINI ON A SURFACE CONTAINING CARBOXYLIC ACID FUNCTIONALITIES.....	91
FIGURE 5-4. PHYSICAL ATTRACTION METHODS PRESENT IN BIOMOLECULE IMMOBILIZATION. (A) IONIC INTERACTION BETWEEN A NEGATIVELY CHARGED CARBOXYL AND A POSITIVELY CHARGED AMINO GROUP OF A PROTEIN STRUCTURE. (B) HYDROGEN BONDING BETWEEN A WATER MOLECULE AND AN AMMONIA MOLECULE. (C) HYDROPHOBIC INTERACTION BETWEEN TWO NONPOLAR SUBSTANCES PRESENT IN AN AQUEOUS SOLUTION. ....	92
FIGURE 5-5. A) SWCNT FUNCTIONALIZATION SCHEME BY ACID TREATMENT, FOLLOWED BY SHIELDING AND NANOTUBE-DNA CONJUGATION. B) HYBRIDIZATION OF DNA-SWCNT AND AuNP PROBING. REPRINTED FROM REF. [35], Y. WEIZMANN ET AL., J. AM. CHEM. SOC., 132, 2010, 14009.....	101
FIGURE 5-6. PROOF OF CONCEPT OF A SWCNT-BASED SENSOR FOR THE DETECTION OF HORSE RADISH PEROXIDASE (HRP). THE PREPARED SWCNT NETWORK IS USED TO BRIDGE THE TWO METALLIC CONTACTS. ONLY THE SPECIFIC REGIONS CONNECTING THE TUBES ARE FUNCTIONALIZED TO INTERACT WITH THE TARGET BIOMOLECULE. REPRINTED FROM REF. [36] Y. WEIZMANN ET AL., J. AM. CHEM. SOC, 133, 2011, 3238. ....	102
FIGURE 5-7. FUNCTIONALIZATION SCHEME FOR THE FABRICATION OF GRAPHENE OXIDE (GO) IMMUNO-SENSORS. GO IS PRODUCED BY ACID TREATMENT ( $\text{NaNO}_3 / \text{H}_2\text{O}_4$ ) OF GRAPHENE SHEETS, PRODUCING CARBOXYLIC FUNCTIONALITIES WHICH IN TURN ARE BONDED TO AMINO GROUPS PRESENT IN ANTIBODIES THROUGH EDC/SULFO-NHS CHEMISTRY. AFTER ROTAVIRUS IMMOBILIZATION, A COMPLEMENTARY ANTIBODY BONDED WITH A DNA-AU NP PROBE IS USED TO MARK THE VIRUS TO EFFECTUATE THE DETECTION. REPRINTED FROM REF. [38] J.H JUNG, ET AL., ANGEW. CHEM. IN. ED. ENGL., 49, 2010, 5708.....	103
FIGURE 5-8. OXYGEN PLASMA TREATMENT SCHEME FOR THE CARBOXYLATION GRAPHENE FOAM NANOSTRUCTURES. AFTER THE CREATION OF CARBOXYLIC GROUPS AT THEIR SURFACE, MULTILAYER SHEETS OF GRAPHENE ARE TREATED WITH EDC/NHS CHEMISTRY TO BIND THEM WITH ANTI-ERBB2 ANTIBODIES. ALTERNATIVELY, THE FOAM STRUCTURE CAN BE DOPED WITH TITANIUM DIOXIDE ( $\text{TiO}_2$ ) NANOTUBES, INCREASING THE OVERALL IMPEDANCE OF THE BIOSENSOR COMPLEX. REPRINTED FROM REF. [46] M. A. ALI ET AL., ACS APPL. MATER. INTERFACES, 8, 2016, 20570. ....	105
FIGURE 5-9. PRODUCTION OF 3DG INK BY POLYMER BLENDING OF POLYLACTIDE-CO-GLYCOLIDE (A HIGHLY BIOCOMPATIBLE ELASTOMER) AND GRAPHENE POWDER. AFTER MIXING, THE SOLUTION CAN BE SCALED UP FOR POLYMER PRINTING APPLICATIONS. POTENTIAL APPLICATIONS OF 3DG BUILT ARCHITECTURES INCLUDE ENERGY STORAGE, BIOELECTRONICS, TISSUE AND ORGAN ENGINEERING. REPRINTED FROM REF. [65] A. E. JAKUS ET AL., ACS NANO, 9, 2015, 4636. ....	109
FIGURE 5-10. SEM MICROGRAPHS OF SUSPENDED CNWs WITH A PROTECTIVE LAYER OF POSITIVE PHOTORESIST, USED FOR GOLD COATING SURFACE MODIFICATION. (A) OVERVIEW OF FIVE SAMPLES WITH RECTANGULAR APPERTURES CREATED BY EXPOSING THE ZONES OF THE PHOTORESIST WHERE THE WIRES ARE. (B) ZOOM IN OF THE IMAGE PRESENTED IN (A). (C) FURTHER MAGNIFICATION REVEALS A GRANULAR PATTERN OF THE PHOTORESIST THAT WAS NOT FULLY DEVELOPED.(D) OPTICAL MICROSCOPE IMAGE OF A RESULTING SUSPENDED CNW AFTER REMOVING THE POSITIVE PHOTORESIST SACRIFICIAL LAYER. ....	112
FIGURE 5-11. SCHEME SHOWING THE COVALENT ATTACHMENT OF 4-ABA INTO A GC SURFACE.....	113
FIGURE 5-12. SCHEMATIC OF A G40T20.RE ELECTRODE, WHICH HAS 4 DIGIT ELECTRODE AND A REFERENCE ELECTRODE. THIS STRUCTURE WAS USED TO PERFORM THE ECM EXPERIMENTS.....	114
FIGURE 5-13. SEM MICROGRAPH OF A SUSPENDED CNW WITH A LAYER OF SPUTTERED GOLD. A DIFFERENT SURFACE MORPHOLOGY IS SLIGHTLY VISIBLE IN THE REGION COATED BY GOLD. ....	115
FIGURE 5-14. EDS SPECTRUM OF DIFFERENT SECTIONS OF THE C-MEMS DEVICE. (A) EDS OF A REGION NEARBY THE END OF THE CNW. (B) EDS SPECTRUM TAKING AT THE SURFACE OF THE SUPPORTING SUBSTRATE. (C) SPECTRA OBTAINED AT ONE OF THE SUPPORTING C-MEMS ELECTRODES. (D) EDS AT THE CENTRAL PORTION OF THE CNW. ....	116
FIGURE 5-15. CYCLIC VOLTAMMOGRAMS OF A GC MICROELECTRODE IN $\text{LiClO}_4$ SOLUTION (100MM) WITH 3MM 4-ABA, SHOWING THE PROGRESSIVE CYCLES (REDUCING PEAK INTENSITY). SCAN RATE: 100MV/s.....	117
FIGURE 5-16. (A) [CONTINUOUS LINE] CYCLIC VOLTAMMOGRAM OF THE PROBE SOLUTION $\text{K}_3[\text{Fe}(\text{CN})_6]$ (1MM) AND $\text{K}_4[\text{Fe}(\text{CN})_6]$ (1 MM) AND KCl 0.5 M, OBTAINED AT A SCAN RATE OF 100MV/s, IN THE CATHODIC DIRECTION. ELECTRODES CONSISTED OF GC MICROELECTRODES, IN THE AFOREMENTIONED SOLUTION. [DASHED-LINE] CYCLIC VOLTAMMOGRAM EVALUATED AT THE SAME CONDITIONS, AFTER THE 4-ABA FUNCTIONALIZATION. (B) CYCLIC VOLTAMMOGRAM OF THE SAME SOLUTION IN (A), FOR THE CONTROL GROUP BEFORE AND AFTER 4-ABA FUNCTIONALIZATION. (D) EIS DIAGRAM OF THE ORIGINAL SAMPLE BEFORE AND AFTER ECM. (D) EIS DIAGRAM OF THE CONTROL GROUP, BEFORE AND AFER 4-ABA MODIFICATION.....	118

FIGURE 6-1. (A) FABRICATION SCHEME USED TO PRODUCE CNW ARRAYS, COMBINING EMS AND CARBONIZATION OF THE STRUCTURES BY PYROLYSIS. (B) SEM MICROGRAPH OF THE SIX-WALL STRUCTURE CONTAINING FIVE CNWs (TOP VIEW, NUMBERED 1 THROUGH 5). (C) CLOSE- UP OF AN INDIVIDUAL SUSPENDED CNW BETWEEN TWO CARBON ELECTRODES..	122
FIGURE 6-2. A) I-V CURVES FOR THREE CNWS OF DIFFERENT D AND SAME LENGTH ( $L=44$ MM). $V_{MAX}=3.4$ V, 5.2 V, 3.0 V AND $T_{MAX}=21$ MS, 43 MS AND 380 MS FOR CNWs WITH $D=300$ NM, 481 NM AND 787 NM, RESPECTIVELY. (B) RESISTANCE EVOLUTION IN THE CASE $L=44$ MM AND $D=300$ NM.....	125
FIGURE 6-3. (A) DEPENDENCE OF MAXIMUM CURRENT DENSITY AT POINT OF CNW BREAKAGE WITH LENGTH OF CNWs. (B) RAMAN SPECTRA FOR CNW WITH GEOMETRY $D=467$ NM AND $L=36.7$ MM. (C) SCATTERING PLOT OF THE $I_D/I_G$ RATIO FOR CNWS OF DIFFERENT DIAMETERS; THE ERROR BARS REPRESENT THE STANDARD DEVIATION. ....	126
FIGURE 6-4. NANOGAPS SIZE DEPENDENCE ON THE DOWNSCALING OF CNWs. (A,B) SEM MICROGRAPHS OF SUSPENDED CNWs BEFORE ELECTRICAL BREAKDOWN: (A) $L=39.2$ MM, $D=1180$ NM AND (B) $L=5$ MM, $D=289$ NM.(C,D) NANOGAPS PRODUCED AFTER APPLYING THE JOULE HEATING CURRENT, WITH GAP SIZE OF: (C) 140 NM AND (D) 12 NM. (E) DEPENDENCE OF THE SIZE OF NANOGAPS WITH THE LENGTH OF THE CNW. IN THIS GRAPH, EACH POINT REPRESENTS FIBERS OF SIMILAR LENGTH AND ERROR BARS REPRESENT THE STANDARD DEVIATION OF THE NANOGAP SIZE IN EACH CASE. IN THE CASE OF THE LEFT-MOST POINT, ONLY ONE FIBER WAS TESTED ( $L=5$ MM). ....	128
FIGURE 6-5. (A) SEM MICROGRAPH OF A CNW FABRICATED IN AIR ATMOSPHERE CONDITIONS ( $L=65$ MM AND $D=1.06$ MM). (B) SEM MICROGRAPH OF A CNW PRODUCED IN A HIGH VACUUM ( $L=65$ MM AND $D=1.10$ MM). (C) CHANGE IN RESISTANCE OF THE CNW PRESENTED IN (A) AFTER APPLICATION OF SUCCESSIVE VOLTAGE SWEEPS. (D) RESISTANCE CHANGE AFTER SUCCESSIVE VOLTAGE CYCLES IN VACUUM TO THE CNW PRESENTED IN (B); THE INSET OF (D) SHOWS A CLOSE-UP VIEW EVIDENCING THE RESISTANCE REDUCTION AFTER EACH STRESSING CYCLE. (E) CHANGE IN THE CRITICAL STIMULATION POWER IN ATMOSPHERE AND VACUUM CONDITIONS. ....	129
FIGURE 6-6. FINITE ELEMENT SIMULATIONS OF THE TEMPERATURE DISTRIBUTION IN CNWs HEATED BY ELECTRIC CURRENTS. (A) A COLORMAP GRAPH OF THE TEMPERATURE PROFILE FIR A CNW WITH LENGTH $L=40$ $\mu$ M AND $D=1$ $\mu$ M. (B) CUTLINE PROFILE OF THE TEMPERATURE ALONG THE AXIS OF THE CNW.....	130

## TABLE OF CONTENTS

ABSTRACT .....	vii
LIST OF FIGURES .....	viii
TABLE OF CONTENTS.....	xiii
1 Introduction .....	16
1.1 Objectives.....	19
1.2 Research hypotheses .....	20
1.2.1 Additive manufacturing .....	20
1.2.2 Functionalization of carbon nanowires .....	21
1.3 Research questions .....	21
1.4 Thesis outline .....	23
2 Carbon Micro Electromechanical Systems (C-MEMS) .....	24
2.1 Fabrication of C-MEMS structures .....	26
2.1.1 Photolithography of photoresist structures .....	26
2.1.2 Pyrolysis of patterned photoresist.....	29
2.2 Characterization by Scanning Electron Microscopy and Energy Dispersive X-ray Spectroscopy.....	30
2.3 Summary .....	32
3 Electro-Mechanical Spinning of Suspended Carbon Nanowires .....	33
3.1 Electrospinning of carbon nanofibers .....	33
3.2 Precursor materials used for CNF production .....	36
3.3 Influence of polymer machining methods on the crystallinity of CNWs .....	40
3.4 Thermal analysis of CNFs produced by pyrolysis .....	48
3.5 Experimental methods .....	49
3.5.1 EMS of SU-8 nanofibers by Method 1.....	50
3.5.1.1 Preparation of polymer solution.....	50
3.5.1.2 Deposition .....	50
3.5.2 EMS of SU-8 nanofibers by Method 2.....	50
3.5.2.1 Preparation of polymer solution.....	50
3.5.2.2 Deposition .....	51
3.5.3 Characterization of CNWs by Scanning Electron Microscopy.....	52
3.5.4 Electric characterization of CNWs.....	53
3.6 Results and discussion.....	53

3.6.1	Morphology analysis of samples obtained with “Method 1” vs “Method 2” .....	53
3.6.2	Influence of soft-bake time.....	54
3.6.3	Analysis of pyrolyzed samples .....	56
3.7	Summary .....	59
4	Microfabrication of Suspended Carbon Nanowires by Multiple-Photon Polymerization .....	61
4.1	Background .....	63
4.2	Mechanisms leading to the smallest MPP features.....	65
4.2.1	Two beam strategies.....	65
4.2.1	Diffusion assisted approaches .....	66
4.3	Theoretical Framework of Multiple Photon Polymerization (MPP) .....	66
4.3.1	Theory of 2PA and 3PA absorption rates using Fermi’s Golden Rule.....	67
4.3.2	Dependence of voxel resolution on process parameters .....	70
4.3.3	Linewidth resolution in scanning writing configuration .....	73
4.4	Experimental methods .....	76
4.4.1	Photoresist preparation .....	76
4.4.2	Two Photon Polymerization (TPP) experiments .....	77
4.5	Results and discussion.....	80
4.5.1	SEM analysis of CNWs produced by TPP.....	80
4.6	Summary .....	84
5	Surface Modification of Carbon Nanostructures.....	86
5.1	Characteristics of the bioreceptor surface .....	86
5.1.1	Physical Characteristics .....	87
5.1.1.1	Surface area .....	87
5.1.1.2	Surface topography .....	87
5.1.1.3	Surface wettability.....	88
5.1.2	Chemical characteristics .....	88
5.1.2.1	The presence of functional groups .....	88
5.2	Biomolecular interactions .....	91
5.3	Frequently used functionalization techniques .....	93
5.4	Advantages and disadvantages of current functionalization techniques.....	95
5.5	Functionalization of carbon nanomaterials .....	96
5.5.1	Common functionalization techniques for carbon nanomaterials.....	101
5.5.1.1	Wet chemical treatment.....	101

5.5.1.2	Plasma-assisted treatment .....	104
5.5.1.3	UV treatment .....	105
5.5.1.4	$\pi$ - $\pi$ stacking .....	106
5.5.2	Alternative functionalization techniques.....	107
5.6	Experimental methods .....	111
5.6.1	Gold coating of CNWs .....	111
5.6.2	Electrochemical Modification of Carbon Electrodes and Carbon Nanowires .....	112
5.7	Results and discussion.....	114
5.7.1	Sputtering of CNW samples .....	114
5.7.2	Electrochemical modification of GC microelectrodes .....	116
5.8	Summary .....	118
6	Nanogap Fabrication by Joule Heating of Carbon Nanowires.....	120
6.1	Background and motivation.....	120
6.2	Experimental methods .....	121
6.2.1	CNW arrays .....	121
6.2.2	Nanogap fabrication .....	122
6.2.3	Simulation of Joule Heating effects in CNWs.....	123
6.3	Results and discussion.....	123
6.3.1	Electrical testing of CNWs and nanogap fabrication .....	123
6.3.2	Reduction Nanogap size with CNW length .....	127
6.3.3	Atmosphere effects on nanogaps .....	128
6.3.4	Finite Element simulation of CNW Joule heating .....	130
6.4	Summary .....	132
7	Concluding Remarks .....	134
7.1	Future work.....	135
7.1.1	EMS of CNWs .....	136
7.1.2	MPP of CNWs .....	136
7.1.3	CNWs as biosensing structures.....	138
7.1.4	Nanogaps in CNWs.....	138
References.....		140
Appendix A .....		153
MatLab routine for CNW diameter measurement .....		153

# 1 Introduction

Nanotechnology has attracted considerable attention in science due to the fundamentally different properties that nanostructures have over bulk materials. Progress in this field is driven by the demand for manufacturing ever-smaller functional devices that can merge these properties with a specific application. For instance, Silicon-based Micro-Electromechanical Systems (MEMS/Si-MEMS) are microscopic devices with characteristic lengths in the micron range<sup>\*</sup> which typically comprise sensing, actuating, optical, fluidic, biological and/or processing functions.<sup>1</sup> However, over the last two decades, Carbon-based micro/nano-electromechanical systems (C-MEMS, C-NEMS) have emerged as a promising extension to conventional Si-MEMS, offering numerous advantages such as scalability in manufacturing, availability of inexpensive precursor materials, tunable surface properties and biocompatibility.<sup>2</sup> Carbon is a material of significant importance, both in nature and fundamental research, due to its widely different structures of its various allotropes.<sup>3,4</sup> In C-MEMS, three-dimensional (3D) glassy carbon (GC) electrodes of desired geometry are derived by patterning of a polymer precursor through photolithography and its subsequent conversion into carbon using pyrolysis in an inert environment or vacuum.<sup>5</sup> Although C-MEMS are composed mostly of glassy carbon material, the goal behind this technology is that it could eventually incorporate all of the carbon allotropes depending on the fabrication process.<sup>2,6</sup>

Among the carbon allotropes,<sup>†</sup> carbon nanostructures have found important application in the manufacturing of next-generation biosensor and biomedical devices, owing to their unique physical and chemical properties,<sup>7</sup> some of them available by virtue of their nanoscale dimensions.<sup>8–10</sup> Well-known examples include Single<sup>11–13</sup> and Multi-walled<sup>14–17</sup> Carbon Nanotubes (SWCNT, MWCNT) and Graphene.<sup>18–20</sup> The integration of these materials into analytical systems has found applications in medical diagnostics,<sup>19</sup> multi-modal drug delivery,<sup>21</sup> bioimaging,<sup>22</sup> environmental monitoring<sup>23</sup> and biocatalytic sensing.<sup>7</sup> For

---

<sup>\*</sup> Or even below 1μm for Nano-electromechanical Systems (NEMS).

<sup>†</sup> Some carbon allotropes include diamond, graphite, lonsdaleite, fullerenes, (C<sub>60</sub>, C<sub>540</sub>, C<sub>70</sub>), amorphous carbon, glassy carbon, graphene, single and multi-walled carbon nanotubes.

cylindrical structures like SWCNTs and MWCNTs, their unique geometry allows them to work in a nanowire or nanochannel configuration.<sup>24–27</sup> Detectors based on this principle can be described as Field Effect Transistors (FET), in which a change in the conductivity of the nanostructure is associated with a change in the potential at its surface, which is usually caused by a sensitive interaction with the environment.<sup>28</sup> In the case of an analytical biosensor platform, the underlying detection mechanism comprises at least two fundamental components: (i) a biological receptive element that selectively interacts with the target analyte; and (ii) a transducer element that converts the biological response into a recognition signal (see Figure 1-1). Even though carbon nanostructures have superior properties that would make them ideal transducing elements, they lack the most important surface characteristic, which is heterogenic reactivity towards biomolecules, thus complicating their straightforward application. Therefore, a central requirement for a successful protein detection on the surface of a carbon nanostructure is a systematic functionalization methodology that converts it from a naturally inert material<sup>29–31</sup> to an active surface that can readily react with the biomolecules of interest.

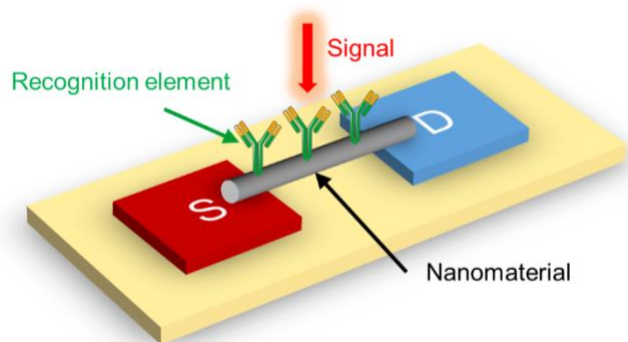


**Figure 1-1.** Impedance Nanowire Biosensor structure acting as a highly sensitive device. The nanomaterial provides the interface at which a recognition component (such as an antibody) is linked. Subsequently, the presence of an analyte will trigger a signal that changes the overall conductance of the channel, revealing its presence.

The manufacturing of biosensor platforms based on the Carbon Nanowire (CNW)<sup>‡</sup> FET principle has other important challenges that have limited their widespread application. For CNWs and CNTs in particular, it is desirable that their position and orientation be controlled within an electric circuit. In addition, they should be connected to metallic electrodes with reproducible ohmic contacts.<sup>32</sup> The available fabrication schemes for CNTs, such as chemical vapor deposition (CVD) fail to achieve this goal, as nanowires must be first synthesized, isolated and placed on a flat substrate, followed by deposition of metallic electrodes with expensive and low-throughput techniques.<sup>33–35</sup> Even though intensive research efforts have been placed in the precise positioning and patterning of nanotubes (for example, through dielectrophoresis), this path continues to be a difficult avenue, with serious throughput limitations.<sup>36,37</sup>

The C-MEMS technology has also been extended by exploring different polymer patterning techniques to integrate allotropes such as CNWs into its toolbox.<sup>3,38,39</sup> One of such methods is Far Field Electrospinning (FFES), a technique in which electrified jets of polymer are used to produce nanofibers which are subsequently carbonized by high temperature treatment in an inert environment (pyrolysis).<sup>40</sup> Electrospinning being a relatively new but prolific research field, has evolved into different sub-techniques and versatile manufacturing methods. One of them is Near Field Electromechanical Spinning (EMS), which is promising for controlling and patterning the deposited polymeric nanofibers. However, as of now, EMS remains largely unexplored, with relatively few compatible materials for fabrication.<sup>41–44</sup> In view of this, some research teams have explored the possibility of using pyrolysis-compatible precursors, such as the carbon-rich photoresist SU-8, which is a negative tone epoxy.<sup>45</sup> While the patterning possibilities offered by this technique are promising,<sup>45</sup> the achieved linewidth resolutions appear to lack the precision required for manufacturing of nanobiosensor platforms.<sup>44,46</sup>

---

<sup>‡</sup> The term Carbon Nanowire (CNW) will be preferred over Carbon Nanofiber (CNF) to emphasize the fact the nanostructure is functioning as the electrical connection between two terminals in a device. Currently, there is no consensus in the literature as to which term should be used to refer to these nanoscale structures, which have similar size and crystallinity. The term CNF is often found in the context of fabrication techniques like Electrospinning, which inherently produce large amounts of randomly oriented thread-like structures (see Ref. 40). On the other hand, CNW has appeared in the context of C-MEMS, where the structures are usually patterned and positioned within a functional device (see Refs. 3,38, for instance).

Multiple Photon Polymerization (MPP) is another Advanced Additive Manufacturing (AdAM) method that has been used for the fabrication and low-cost prototyping of polymer microstructures with feature sizes in the micron and sub-micron scale.<sup>47–49</sup> In particular, MPP has been integrated with pyrolysis techniques to produce GC nanolattices<sup>50</sup> and nanostructures.<sup>51,52</sup> Furthermore, MPP is inherently capable of writing, single-voxel thick lines (known as *linewidth* resolution) that can have dimensions in the ~200 nm before pyrolysis processing, and potentially shrink up to 90% after thermal decomposition and transition into conductive carbon with reliable ohmic contacts.<sup>3,44</sup> In theory, this technique can create complex CNW geometries with arbitrary positioning while at the same time offering an alternative more amenable to manufacturing than current methods available for suspended nanowire positioning, which usually involve CNW synthesis, isolation, nanopositioning prior to electrical interfacing.<sup>3</sup>

Therefore, the current work introduces, for the first time, a thorough study of the use of two AdAM techniques, EMS and MPP, for the precise patterning of CNWs. Moreover, the dissertation inquires the possibility of chemically engineering the surface of their constituent material, GC, with the aim of pursuing biosensing applications. This analysis is mainly performed through electrochemical characterization of functionalized C-MEMS structures. In the case of EMS, the geometry obtained for the C-MEMS/CNW hybrid allowed the study of morphology, chemical composition and electrical IV characteristics of CNWs. For both EMS and MPP techniques, the reader will find that special emphasis is placed on investigating of how the process variables affect the reproducibility of CNW production.

### 1.1 *Objectives*

In view of the manufacturing and surface chemistry challenges posed by CNW biosensor fabrication, the following dissertation is divided in two central objectives:

- 1) To explore the feasibility of using advanced additive manufacturing techniques to improve the reproducibility of CNW production in the nanoscale range.

In particular, EMS and Direct Femtosecond Laser Writing (DLW) techniques will be studied and tested in terms of their fabrication parameters. Furthermore, morphological and electrical characterization of the obtained samples will be key in the discussion and assessment of this objective.

2) To study the surface chemistry of CNWs as a material for biomolecule immobilization.

The goal will be to explore a functionalization technique that will allow the surface modification of GC to achieve the immobilization of a biomolecule. GC will be studied in particular since it is the predominant material obtained from advanced manufacturing techniques like EMS<sup>46</sup> and TPP.<sup>50</sup>

## 1.2 *Research hypotheses*

The research hypotheses of the following dissertation are divided into two sections. The first section is related to additive manufacturing techniques used to produce the CNWs; the second one includes the proposed hypotheses with regards to functionalization those structures.

### 1.2.1 *Additive manufacturing*

**Hypothesis 1 (H1):** The geometry (diameter and length) of CNWs produced by Electro-Mechanical Spinning (EMS) can be controlled by having consistent fabrication parameters (stage velocity, voltage, dispense rate, polymer formulation). A given set of parameters should, therefore, result in a repeatable nanowire structure with defined geometry. We expect this repeatability will be evident in the statistical deviation from a mean value of the measured diameter and length.

**Hypothesis 2 (H2):** MPP lithography can be used to produce sub-micrometric CNWs by pyrolysis of a highly cross-linked photoresin, such as SU-8. The dimensions of the produced CNWs are expected to depend on the process variables. By controlling the energy dosage

impinged on the photoresin, the localized polymerized volume will vary in size. Therefore, it is expected that dosage will be directly correlated to the diameter of the polymerized polymeric microstructure precursor (and consequently, the diameter of its carbonized version, the CNWs).

### *1.2.2 Functionalization of carbon nanowires*

**Hypothesis 3 (H3):** Through a suitable surface chemistry modification, CNWs can provide a platform that can serve for biomolecule immobilization.

**Hypothesis 4 (H4):** Localized surface modification of CNWs can be achieved by chemically protecting the rest of the device and addressing only the wire area.

- Glassy carbon is chemically inert material. We expect this material will be inefficient for biomolecule immobilization.
- By locally depositing a material with stronger affinity to biomolecules, we can study the performance of Suspended CNW as biosensors. In this study, the molecule 4-aminobenzoic acid (4-ABA) will be explored as the interfacing molecule between the surface wire area (composed of GC) and a protein probe.

### *1.3 Research questions*

The following research questions were formulated as a function of hypotheses 1-4:

1. **H1:** What are the parameters (stage velocity, voltage, dispense rate, polymer formulation) for EMS that allow the fabrication of CNWs?

Why have those parameters failed to produce reproducible CNWs in the past?

Are there research efforts that suggest the use of an automated deposition of polymeric nanofibers with EMS, which can be pyrolyzed into CNWs?

2. **H2:** In the literature, is there any evidence of the process parameters that should be employed to fabricate SU-8 polymeric structures with MPP?

How does the minimum characteristic features that can be obtained through MPP (i.e. *voxels*) scale with two and three photon absorption (TPA, 3PA) processes?

What are the specific role played by variables such as the intensity of the laser, frequency of operation, writing speed (or stage velocity) in the efficiency of the 2PA/3PA process?

3. **H3:** What are the most important surface characteristics that allow protein immobilization in an interface?

Is there any evidence in the literature that GC can serve as a platform for biomolecule detection?

What are the most common functionalization techniques that have been used in carbon nanostructures? What are the most recent techniques and, are they promising?

4. **H4:** What methods can be employed to achieve local surface modification of CNWs?  
Are there any reported methods in the literature?

Is there a manufacturing method that can allow the selective addressing of the CNW micro/nano-surface, while protecting the rest of the C-MEMS device?

Are Electrochemical Modification (ECM) techniques suitable for local modification of GC materials?

#### *1.4 Thesis outline*

After introducing the area of study and research topic to the reader in Chapter 1, Chapter 2 covers the general aspects of Carbon Micro Electro-Mechanical Systems (C-MEMS) technology. In Chapter 3 and 4, emphasis is made on how sub-micrometric features can be added to the C-MEMS toolbox via AdAM techniques, such as Near-Field Electro-Mechanical Spinning (EMS) and Multiple Photon Polymerization (MPP). These methods allow the fabrication of highly oriented, freely-standing Carbon Nanowires (CNWs), which are nanostructures that hold potential for biosensor applications in analytic devices. Next, Chapter 5 explores some of the fundamental requirements that CNWs should fulfill to be used as bio-sensing elements and gives a general background on the functionalization strategies that are available in the literature to chemically modify Carbon nano-structures. Furthermore, in Chapter 6, the reader will find an application of the CNWs investigated in this dissertation: Nano-gap fabrication in CNWs via Joule-Heating. Finally, the conclusions drawn from of the experimental results and remarks for future work are summarized in Chapter 7.

## 2 Carbon Micro Electromechanical Systems (C-MEMS)

Carbon Micro Electromechanical Systems (C-MEMS) constitutes a class of miniaturized functional devices in the sensor industry. The term C-MEMS also encompasses the set of fabrication methods used to produce glass-like carbon (or Glassy Carbon, GC) micro/nano-structures that result from the pyrolysis of pre-patterned, organic polymer precursors (as schematically presented in Figure 2-1).<sup>53</sup> This method was presented for the first time by Schueller and colleagues in 1997.<sup>54</sup> In their pioneering work, the fabricated carbon micro-components were derived from polymers and were proposed for microreactor applications in view of their appealing chemical, mechanical and electrical properties (GC now being a conductor, as opposed to an insulator, like the polymer precursor).

Because GC is formed by thermal decomposition of the polymer precursor at high temperatures (~900°C or more), C-MEMS devices are shrunk into smaller structures with high aspect ratio. This volumetric loss occurs due to the release of gases such as oxygen and hydrogen,<sup>55</sup>s leading to shrinkage of the heated structures, which can be as high as 90% and thereby resulting in sub-lithography resolution features.<sup>38</sup> GC also exhibits a wide electrochemical stability window, biocompatibility, superior chemical resistance and semiconductor-like electrical properties.<sup>2,5,38,56</sup> It is in view of these properties that C-MEMS has found applications such as Li-ion batteries,<sup>57</sup> dielectrophoretic immobilization devices<sup>58</sup> and electrochemical sensing platforms.<sup>59,60</sup> Furthermore, a wide variety of GC microstructures can be found in the literature,<sup>61</sup> which range from the ubiquitous post arrays<sup>62</sup> (see Figure 2-1B) to nanopillars,<sup>63</sup> interdigitated electrodes,<sup>64</sup> nanowires (or microbridges),<sup>3,38,46</sup> nanogaps,<sup>46</sup> TEM grids<sup>65</sup> and AFM tips.<sup>52</sup>

## Carbon Microelectromechanical Systems (C-MEMS)

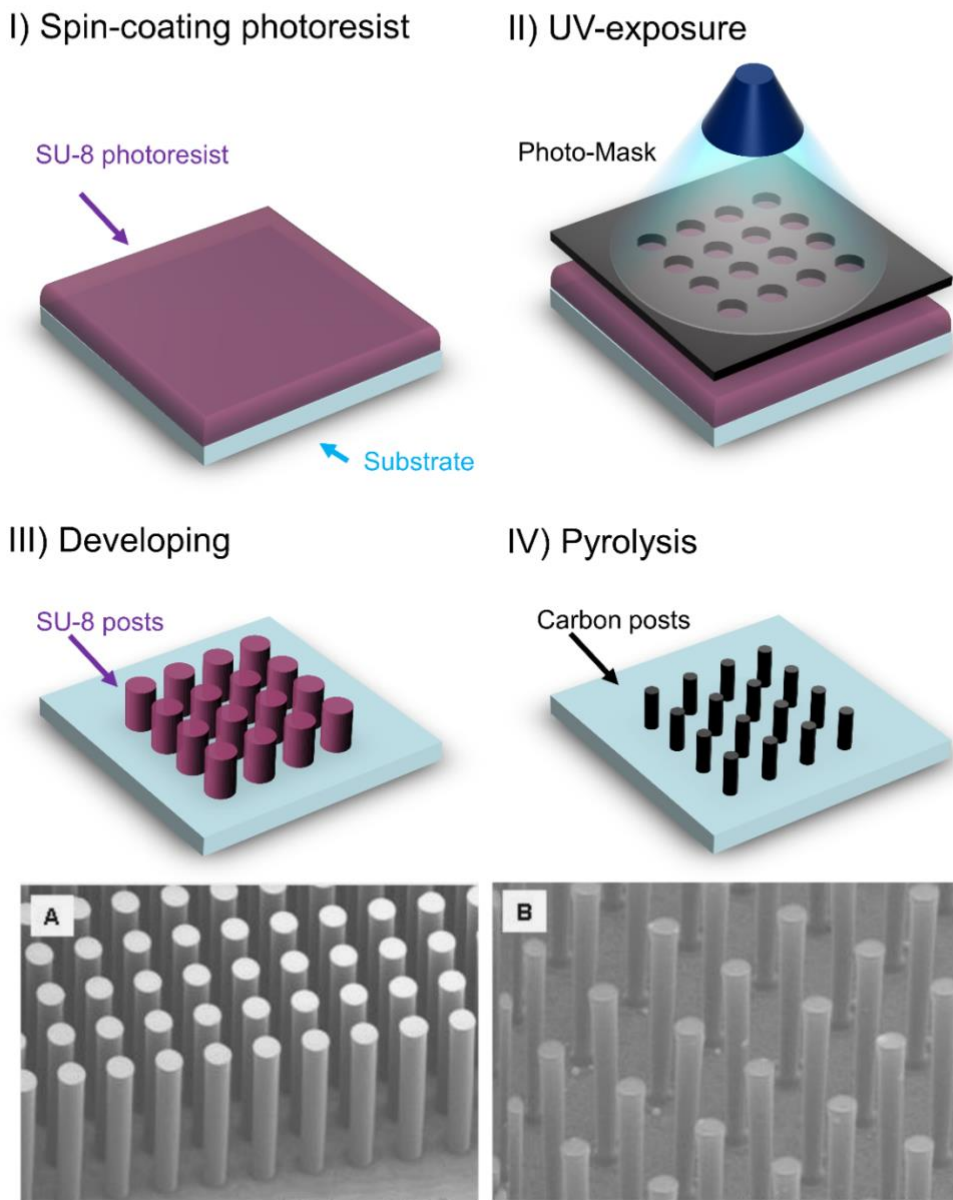


**Figure 2-1.** The C-MEMS Technology manufacturing process begins with (i) coating of a polymer unto a substrate, followed by (ii) patterning with UV-exposure photolithography. (iii) Afterwards, features are developed with a solvent; (iv) subsequently, they are carbonized in a pyrolysis furnace at high temperatures (900°C) and an inert environment. (Bottom, A) Patterned SU-8 photoresist (polymer) structures before carbonization. (B) The same structures, after the carbonization step, featuring conformal shrinkage in post height and diameter. Images adapted from ref. [62] R. Srikanth, et al., *J. Electrochem. Soc.*, **147.1**, 2000, 277-282.

## *2.1 Fabrication of C-MEMS structures*

As stated previously in the introduction of this dissertation, one of the research objectives is to make suspended carbon nanowire structures with sub-micrometric dimensions. The fabrication of these kind of structures has been previously reported for methodologies, such as Electrospinning (ES) and photoresist patterning by photolithography. The first method can be regarded as an extension step to the latter, by which polymeric nanofibers can be produced, since photolithography is inherently restricted by the diffraction limit. A description of the influence of the selected microfabrication method on the final carbon nanowire (CNW) properties is presented in Chapter 3. The current section then focuses on presenting the fabrication protocol followed in this work to create the supporting electrode structures where the CNW sensor element rests on. These electrodes serve three main purposes: 1) they provide electrical interfacing with ohmic contacts to the CNW sensor element; 2) electrodes elevate the wire from the substrate, allowing it to be suspended from the surface and 3) they serve as a transition from the mesoscale (i.e. the millimeter-sized contact pads) to the CNW scale, allowing instrumentation and interfacing.

### *2.1.1 Photolithography of photoresist structures*

Table 2-1 summarizes the steps taken to fabricate the C-MEMS electrodes. In Figure 2-2(a-d), the photomasks used for fabrication are shown. Two main designs were employed: “Mask 1”, as seen in Figure 2-2(a-b) having 6 available electrodes for fiber deposition and “Mask 2”, with 4 electrodes and one reference electrode for electrochemical sensing experiments. In practice, “Mask1” was used to optimize fabrication parameters for CNW manufacturing and “Mask 2” was meant for fabrication of the final device (thus, the reference electrode for electrochemical experiments).

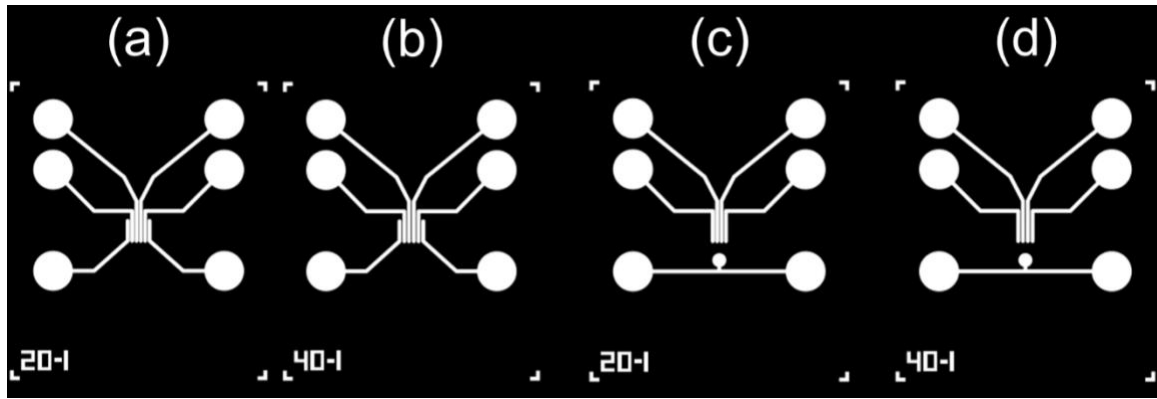


**Figure 2-2.** (a-b) “Mask 1”: Six-electrode mask design for photolithography used in the fabrication of the C-MEMS structures. The lower left corner shows a code that indicates the separation between the electrodes (20 and 40 $\mu\text{m}$ , respectively). (c-d) “Mask 2”: Four-electrode mask design, where two of the electrodes have been replaced by a single reference electrode. Separations of (c) 20 and (d) 40 $\mu\text{m}$ .

The targeted height for the polymeric structures was  $h_{\text{SU8}} = 20 \mu\text{m}$ , so that after the carbonization step, the volumetric shrinkage would yield a reduction down to  $h_{\text{CE}} \approx 10 \mu\text{m}$  (here, the sub-indexes SU8 and CE refer to the photoresist precursor and the carbon electrode, respectively). It was found that the height  $h_{\text{CE}} \approx 10 \mu\text{m}$  was tall enough to elevate CNWs from the substrate, yet short enough to prevent it from coming in contact with the roof of a PDMS microfluidic channel of 30  $\mu\text{m}$  in height that would be incorporated in latter steps of the fabrication. The most important steps (spin coating, UV-exposure and Developing) are schematically represented in Figure 2-1 (I-III). The height of structures was found to be of  $h_{\text{SU8}} = 20 \pm 1 \mu\text{m}$ , where 1 $\mu\text{m}$  is the uncertainty measurement of the Vernier tool used. After following all the steps on Table 2-1, the result is a silicon wafer containing the negative design from the mask, as seen in Figure 2-3, which is expected outcome for a negative tone photoresist.

**Table 2-1.** Protocol for SU-8 2015 photolithography (target height of  $h_{\text{SU8}} = 20 \mu\text{m}$ )

Step	Description	Comments
1	<b>Substrate cleaning:</b> Substrate was a new crystalline 4 inch Si/SiO <sub>2</sub> wafer, 525 $\mu\text{m}$ thick (no doping). Cleaning was performed using acetone and isopropanol afterwards.	Thorough cleaning with isopropanol after acetone will prevent stains on the surface of wafer.
2	<b>Substrate dehydration</b> for 30 min @ 120°C.	Measure the temperature @ the surface of hotplate with a surface thermometer to make sure all temperatures are correct.

2	<b>Spin coating:</b> For SU-8 2015 and a target thickness of 20 $\mu\text{m}$ : <ul style="list-style-type: none"> <li>• Step 1: 10sec @500rpm, acceleration:100rpm/sec</li> <li>• Step 2: 30sec @2000rpm, acceleration:300rpm/sec</li> </ul> Let wafer <b>Rest</b> for 1hr.	Choose the target thickness (in this case, $h_{\text{SU8}} = 20 \mu\text{m}$ ) and get parameters from manufacturer's processing guidelines (in our case, MicroChem®).  Keep wafer away from dust in the Rest step.
3	<b>Soft-bake:</b> Heat structure to 95°C for 3 min.	Hotplate setpoint was 97°C so that the measured temperature was ~95°C.
4	<b>UV-exposure:</b> Structures were exposed to UV light for 50 sec.(300W, i-line)	Important distinction:  Using a generic lamp (Blak-Ray B-100AP, 100W, distance from lamp of 20cm), the time 50sec was used first and results were evaluated. If structures were underexposed, time would be increased by 1 or 2 seconds until the correct result was achieved. Exposures would be performed individually in 4 sections of the wafer to maximize light homogeneity.  Using lamp (Dymax Model 2000 Flood, 400W, distance from lamp of ~30cm), time would be set to 6 sec. If samples came out overexposed, time would be reduced to 4 sec (as a minimum).
5	<b>Post-Exposure Bake (PEB):</b> Structures were heated to 95°C for 4 min.	Same as step 3.
6	<b>Developing:</b> Submerge wafer into SU-8 Developer (MicroChem®) solution for 3 minutes, followed by 10 sec rinsing with fresh developer solution and another 10 sec rinsing with Isopropanol.	For structures that have a height less than 10 $\mu\text{m}$ avoid Isopropanol rinsing. It was found that performing this rinsing after developing resulted in detachment of the SU-8 structures from the substrates.
7	<b>Hard bake:</b> Heat structures to 200°C for 1 hr	Hotplate setpoint was 202°C so that the measured temperature was ~200°C. The processing guidelines for SU-8 mention that this step is optional, however, it has been found that for C-MEMS fabrication, this step is highly recommended (if not mandatory).

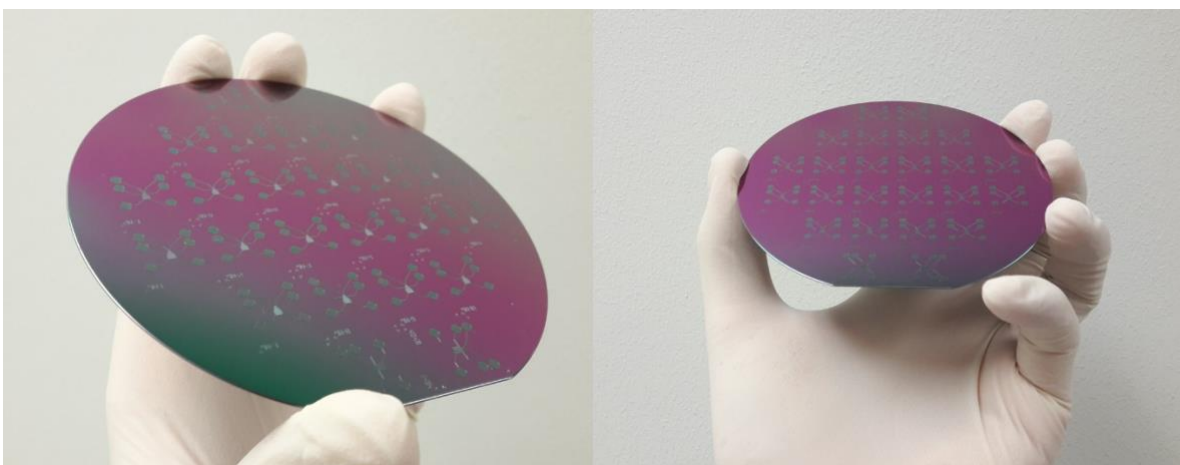


**Figure 2-3.** Two views of the resulting patterned photoresist using “Mask 1” from Figure 2-2(a-b). As seen in the image, SU-8 photolithography allows wafer scale production of microelectrodes.

### *2.1.2 Pyrolysis of patterned photoresist*

After photopatterning the SU-8 2015 precursor, samples were subjected to a high temperature treatment of up to 900°C in an ultra-pure grade nitrogen environment using a furnace (PEO 601, ATV Technologie GmbH, Germany) to produce the C-MEMS electrodes (schematically shown in Figure 2-1 IV). Several process variables involved in the pyrolysis are known to affect the microstructure of the resulting carbon:<sup>55,66</sup> target temperature, ramp rate, dwell time (the duration of the time that the high temperature is maintained), the chemical nature of the inert gas, flow rate, and the configuration/orientation of samples within the furnace. Because the focus of the current work was not to optimize such parameters, the pyrolysis protocol variables were kept unchanged from a standard close to that reported on the literature.<sup>55</sup> The only variable that was modified was that of flow rate, which was found to heavily affect the yield rate of CNWs, but not that of C-MEMS electrodes. However, once a working flow rate was found (5.5 L/min), the same value was used for the rest of the experiments here reported, unless otherwise stated.

The parameters used for pyrolysis are best illustrated in Figure 2-4, where the set temperature is plotted against time. In the initial phase, 99 min of the routine are devoted to evacuating all gases within the tube furnace by flushing in ultra-high purity N<sub>2</sub> at a rate of 5.5L/min. For this pyrolysis routine, the corresponding ramp rate is 5°C/min, when going from room temperature (~25°C) to 300°C and from 300°C to 900°C. Both of these temperatures where kept at dwell times of 1hr. Finally, the total duration of the routine is estimated to be around 526 min, although this lapse could get extended if the natural cooldown process has not finished yet.

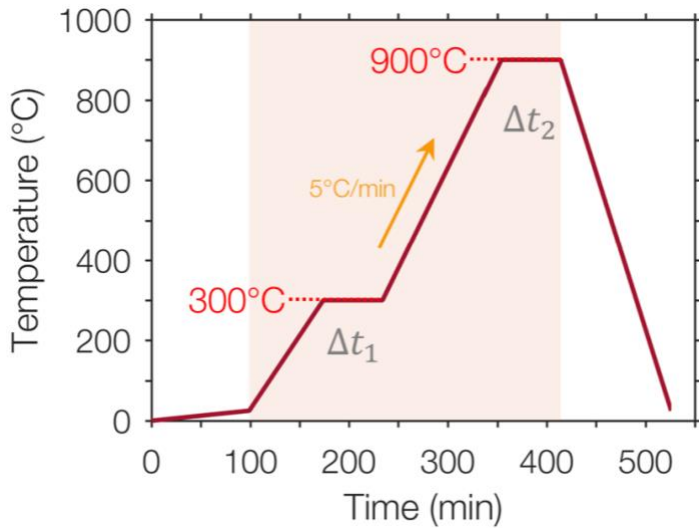


**Figure 2-4** Plotting of the pyrolysis set temperature against time in minutes (dwell times:  $\Delta t_1 = \Delta t_2 = 60\text{ min}$ ). The filled portion of the plot indicates the parts of the process in which heat control was applied by the automated furnace. Note that the final ramp going down is just an indication of what the temperature of the furnace should be. Nonetheless, the furnace is cooled down naturally, and thus, cooldown could take slightly longer time in practice.

## 2.2 Characterization by Scanning Electron Microscopy and Energy Dispersive X-ray Spectroscopy

After pyrolysis, samples were taken to a Scanning Electron Microscope (SEM; EVO MA25, Zeiss, Germany) for morphology characterization and Energy Dispersive X-ray Spectroscopy (EDS; XFlash 6, Bruker Corporation, Billerica, MA, USA) for elemental identification. Figure 2-5a shows an SEM micrograph of an electrode fabricated with the photomask from design “Mask 1”, with the original gap of  $40\text{ }\mu\text{m}$  gap (G40). For each classification of gaps, 10 samples were taken randomly to measure the resulting gap length after pyrolysis. It was found that for G20 samples, the resulting gap after pyrolysis widened to  $41.0 \pm 1.4\text{ }\mu\text{m}$ , with fairly low variation between devices, while samples from G40 had a gap of  $60.5 \pm 4.3\text{ }\mu\text{m}$ , showing a greater spread in the measurements. This variation is likely to have happened from before the pyrolysis step, and is attributed to the reproducibility of the UV-exposure step. The main limitation of the set up used was the control over the shutting speed (which was manually switched), which directly affected exposure time. In general, a

lower yield rate would be obtained for G20 samples and thus, these samples were more selectively chosen, whereas for G40 samples, almost all of the time we were able to process the complete amount of the devices (hence, the larger variability). Furthermore, it is expected that any variation before pyrolysis will be amplified, as the gap widens further with the volumetric loss and shrinkage. Nonetheless, variations were within 2-10% for all samples.

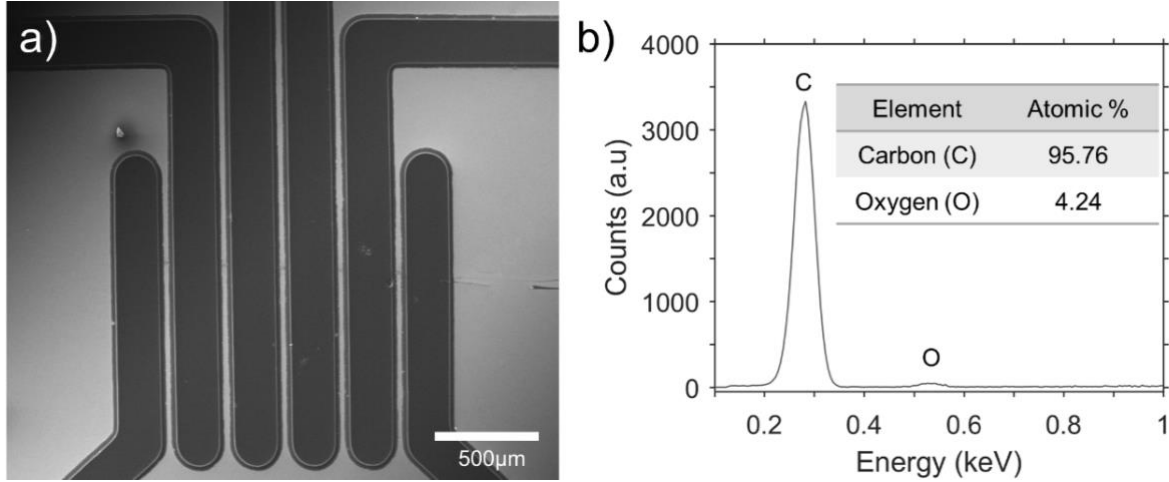


**Figure 2-5.** (a) Carbon micro-electrodes obtained from pyrolysis at 900°C of design “Mask 1”. (b) EDS spectrum analysis of electrode number 3 in (a). Spectrum is presented in the range of 0.1 to 1 keV, showing peaks corresponding to carbon and oxygen. The inset table shows the atomic percentage measured from the spectrum in (b).

Figure 2-5b shows the EDS spectrum of a typical carbon microelectrode (in this case, electrode 3 from left to right). To assess the validity of the obtained data in terms of the analytical area, Castaing’s formula was used to estimate the minimum depth of sample needed to detect carbon and oxygen (the main components of the sample):<sup>67</sup>

$$z_m = 0.033(E_0^{1.7} - E_c^{1.7}) \frac{A}{\rho Z} \quad (2.1)$$

where  $z_m$  is the X-ray generation depth (μm),  $E_0$  is the accelerating voltage (kV),  $E_c$  is the minimum emission voltage (keV),  $A$  is the atomic mass,  $\rho$  is the density of the target (g/cm<sup>3</sup>) and  $Z$  is the atomic number. In our experiment,  $E_0 = 20$ kV, and we estimate to be in the order of  $E_c = 5$ keV.<sup>67</sup> Moreover,  $\rho_{\text{Glassy Carbon}} = 1.7$  g/cm<sup>3</sup>,  $A_{\text{Carbon}} = 12.01$ u and

$Z_{\text{Carbon}} = 6$ , and for oxygen  $A_{\text{Oxygen}} = 16.0\text{u}$ ,  $Z_{\text{Oxygen}} = 8$ . For these parameters, Equation 2.1 resulted in X-ray depths of  $z_m = 5.7\mu\text{m}$  for both materials, which is smaller than the thickness of the tested sample.

As seen in Figure 2-5b, the X-ray peak of carbon is located at 0.282 keV, which is very close to the characteristic value of 0.277 keV. In the case of the peak for oxygen, it is centered at 0.527 keV, near the characteristic value of 0.525 keV for this element. The inset of Figure 2-5b shows the atomic percentages obtained from the EDS analysis. As expected, there is a predominant amount of carbon after pyrolysis (>95%), which is indicative of a successful carbonization of the sample.

### 2.3 *Summary*

This chapter presented a brief background of C-MEMS and how it is used as a methodology to produce micrometric structures for device fabrication. A standard microfabrication protocol was followed to obtain microstructures from SU-8, a versatile negative tone photoresist widely used in photolithography. The manufactured structures were produced with two mask designs based on the electrode configuration and separation (G20 for a gap of 20  $\mu\text{m}$  and G40 for 40 $\mu\text{m}$ ). Although not presented here, the derived pyrolysis method was found to be successful not only for SU-8 microstructure carbonization, but also for CNW production. Therefore, the reader will find in the following sections how the presented C-MEMS can be integrated with an SU-8 nanofiber production method (Electromechanical Spinning, EMS) in complete manufacturing process.

## 3 Electro-Mechanical Spinning of Suspended Carbon Nanowires

### 3.1 *Electrospinning of carbon nanofibers*

The C-MEMS methodology has been extended by exploring different polymer patterning techniques to integrate allotropes such as carbon nanowires (CNWs) as part of the basic building blocks of sensor devices.<sup>3,38,44</sup> A typical method used to produce precursor polymeric nanofibers is Electrospinning (ES). ES was invented in 1934, and it consists on application of an electrostatic force to a polymer solution to spin micro/nanofibrous filaments with diameters in the 10 nm to 10  $\mu\text{m}$ .<sup>68</sup> In general, ES depends on the following parameters: applied electric field, solution conductivity, jet length, solution viscosity, surrounding gas, flow rate and geometry of the collector assembly.<sup>68</sup> Depending on the distance between the collector and the dispensing needle, the electrospun jet will experience a whipping motion which can be controlled near the tip. This operation region is called Near-Field Electrospinning (NFES).<sup>69</sup> On the other hand, if the collector is farther from the dispensing tip, the whipping motion of the jet will dominate. This configuration is called Far-Field ES (FFES).<sup>3</sup> The two configurations are displayed on Figure 3-1.

Carbon nanofibers (CNFs) can be defined as long, thin strands of material with diameters in the 10-1000 nm range, composed mostly of carbon atoms bonded together in microscopic crystals and aligned parallel to the long axis of the fiber.<sup>68</sup> It is important to notice that CNFs differ from single walled carbon nanotubes (SWCNTs), which can be visualized as a single graphene sheet that is seamlessly wrapped into a cylindrical tube with diameter in the range of 0.4 to 2.5 nm<sup>70</sup> (see Figure 3-2a,d). CNFs are also different from multi-walled carbon nanotubes (MWCNTs), as the latter have outer diameters that are typically in the 10-50 nm range and present overall higher crystallinity, graphitic content and weak length-dependent resistance (see Figure 3-2e for a representation of MWCNTs).<sup>17</sup> A comparison of the three structures can be found in Figure 3-2, which compares the overall difference in order of magnitude of diameters and crystallinity. Furthermore, the term CNF is usually used in the context of FFES where these

nanostructures are randomly deposited in mats.<sup>40,71</sup> On the other hand, when these structures are patterned within C-MEMS devices, they are referred as CNWs (although there is no consensus as to which term should be used<sup>3,44,46,72</sup>).

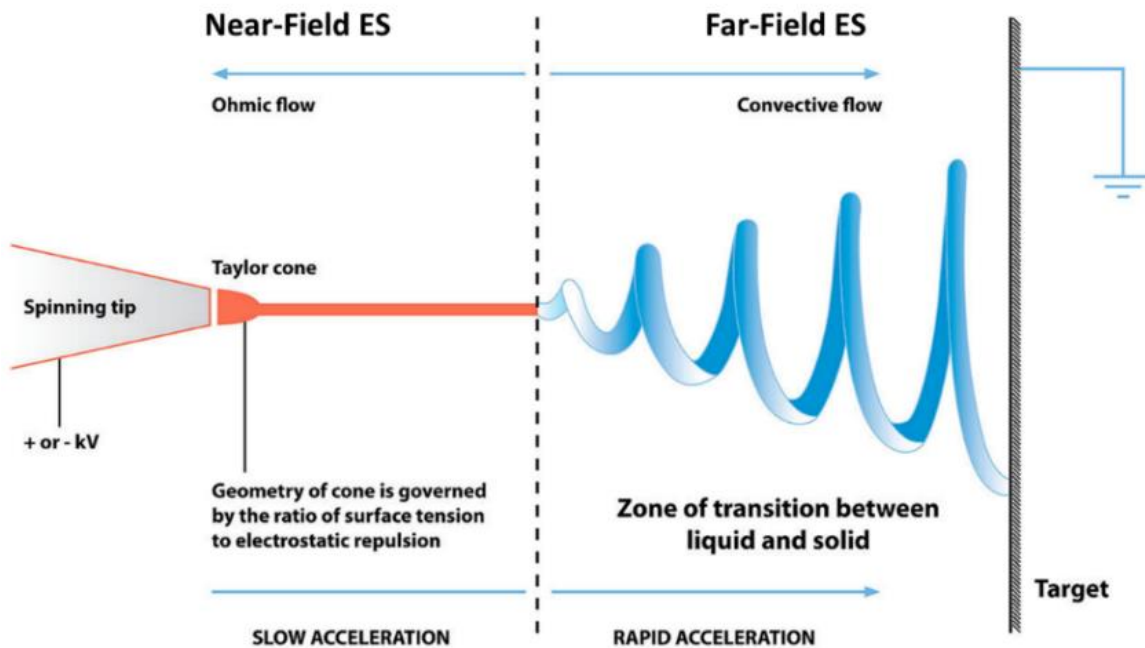


**Figure 3-1.** Comparison of the two regimes under which electrospinning occurs, showing the basic components: dispensing needle, polymer solution and collector or target. Close to the electrospun jet, the flow is ohmic and is slowly accelerated, resulting in no bending instabilities (Near Field Electro-Spinning, NFES). On the contrary, far from the needle the flow is convective and is dominated by rapid acceleration which leads to Earnshaw instabilities (Far-Field ES, FFES).

It has been reported that in the C-MEMS fabrication process and particularly in the pyrolysis step, polymer precursors preserve morphology and chain configuration: an entangled polymer precursor thereby converts into more vitreous carbon materials even after thermal decomposition at high temperatures.<sup>3,73</sup> Hence, it follows that polymer precursors with minimized chain entanglements will result in the increased graphitization of the carbon product, since carbonized chains cannot convert into graphitic domains.<sup>74,75</sup> It follows that the polymer machining method employed to shape the carbon precursor will be of utmost importance to the morphology and crystallinity of the final CNF structure.

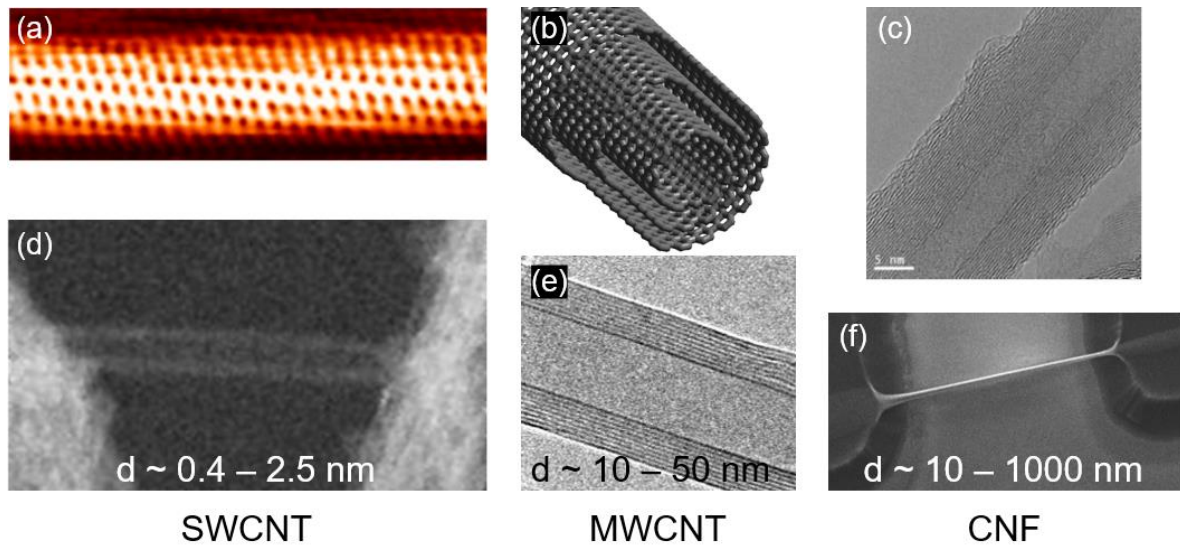


**Figure 3-2.** The different kinds of carbon nanowires. (a,d) Single walled carbon nanotubes (SWCNTs), showing the seamlessly rolled graphene sheet in a cylindrical configuration; in (a) a Scanning Tunneling Microscopy (STM) micrograph of an individual SWCNT is shown, while (d) shows the Scanning Electron Microscopy (SEM) image of the nanotube. (b) Three-dimensional representation of the multiple graphene sheets existing in multi-walled carbon nanotubes (MWCNTs), along with a High-Resolution Transmission Electron Microscopy (HR-TEM) imaging of the nanotube. (c,f) HR-TEM and SEM images of a suspended Carbon Nanofiber. The term Carbon Nanowire (CNW) has also been used in the literature. Reprinted from ref [76]. , W. Odom et al., *J. Phys. Condens. Matter.*, **14**, 2002, R145-R167.

According to Sharma *et al.*<sup>3</sup>, the following are parameters that play an important role in increasing the graphitic content of CNFs produced by ES of polymeric precursors: (1) the chemical composition and viscoelasticity of the precursor; (2) the thickness in the produced polymeric wires; (3) the heat treatment temperature; (4) the molecular alignment of the polymer by shaping in the nozzle tip; (5) mechanical pulling on the polymeric jet during electrospinning; (6) alignment of polymer chains induced by the presence of the electric field; (7) catalysts and solvents in the precursor and finally, (8) templating.

In the present chapter, the different polymer machining techniques and materials that have been employed to produce CNFs/CNWs will be reviewed. Parameters (1), (2), (5), (6) will be evaluated for a variety fabrication techniques; the focus of the investigation will be on the impact that such methods have on desirable characteristics for building highly sensitive sensor devices, including electric conductivity and controllable patterning onto MEMS systems.

### **3.2 Precursor materials used for CNF production**

Early attempts of C-MEMS devices included the use of materials such as diazo resins, phenolformaldehyde and furfuryl alcohol-based resins as precursors for in the carbonization process.<sup>77</sup> The basic requirement to produce CNFs is that the precursor material should be a carbon rich compound and it should be compatible with the pyrolysis step, which involves heating up to temperatures in the range of 900°C, in an inert environment (Argon, Nitrogen or vacuum conditions). Because of this, the most widely used scheme of CNF production involves the pyrolysis of poly(acrylonitrile) (PAN) and copolymers of PAN, which exhibit very high carbon yields after carbonization (up to 56%).<sup>68</sup> However, the most challenging task when working with acrylonitrile (AN) involved its proper dissolving for solution handling in spinning techniques; proper solvents include dimethylformamide (DMF), dimethyl sulfoxide (DMSO), dimethyl sulfone, tetramethylsulfide, aqueous solutions of ethylene carbonate and some mineral salts.<sup>68</sup>

The incorporation of structures such as nanowires into MEMS devices has been performed predominantly with photolithographic techniques, involving the fabrication of Silicon (Si) wire devices.<sup>78</sup> With the advent of the C-MEMS technology, it became clear that scientists had the available photosensitive materials provided by Si-MEMS, and thus began exploring their use in combination with other machining methods, such as ES. One of the first studies that employed photoresins (SU-8 2100) as precursors in FFES was the one by Jeremy K. Steach and coworkers.<sup>79</sup> In their work, researchers explored the optimization of the FFES parameters, such as the distance between the collector and the dispensing needle, the applied voltage, SU-8 concentration in the solution and flow rate.<sup>79</sup> After deposition, the electrospun nanofibers were pyrolyzed under a forming gas atmosphere (95% N<sub>2</sub> and 5% H<sub>2</sub>). This procedure yielded CNFs with diameters in the range of 320±140 nm. It is important to mention that in this experiment, the electrospun nanofibers were not collected in a moving platform. Furthermore, the crystallinity of the CNFs was characterized by means of Raman spectroscopy.<sup>79</sup> Two sets of electrospun fibers were characterized: fibers with 75% (v/v) of SU-8 2100 in the solution and 70% ones. These sets of fibers are shown in Figure 3-3a. Authors evaluated the crystallinity of the samples by measuring the area under the disordered peak ( $I_D$ ) and the ordered peaks ( $I_G$ )

utilizing a Gaussian-Lorentz fit. They concluded that the ratio  $I_D/I_G$  was close for both trials ( $1.20 \pm 0.10$  for the 70% sample, and  $1.14 \pm 0.14$  for the 75% sample), suggesting similar molecular  $sp^2$  content in the samples after pyrolysis.<sup>79</sup> Finally, using the Tuinstra-Koenig relationship, they calculated an average crystallite size  $L_a$  of 7.1 nm, suggesting an overall glassy carbon composition in the CNFs.<sup>79</sup>

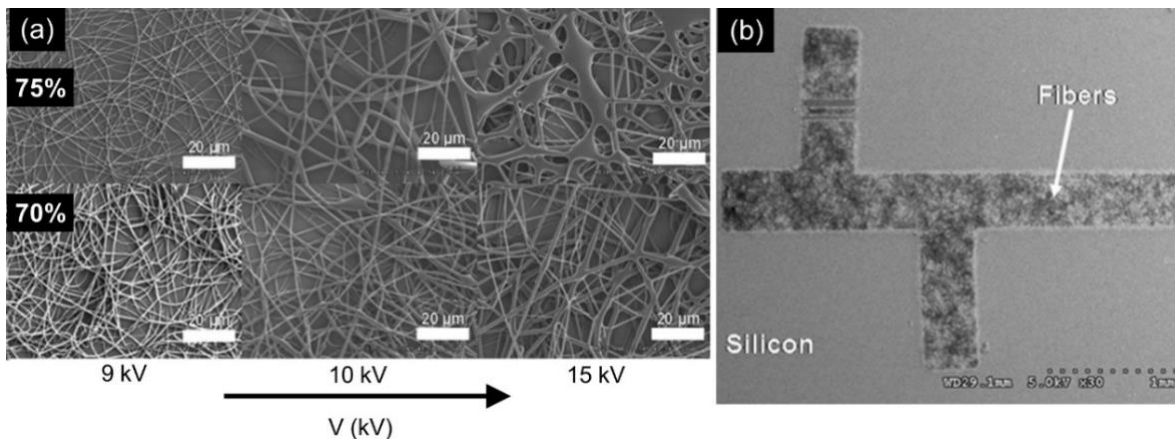


**Figure 3-3.** (a) Electrospun photoresist (SU-8 2100) on a flat collector plate with two different solution concentrations (in cyclopentanone) and three different spinning voltages (9kV, 10kV and 15 kV). (b) Patterning of a randomly deposited nanofiber mat by exposing sample to UV light and subsequent developing. Reprinted from ref. <sup>79</sup>, Steach, J. K. *et al.*, *J. Appl. Polym. Sci.*, **118**, 2010, 405-412.

In the study by Steach and coworkers,<sup>79</sup> the collector plate was used in a static configuration. This arrangement led to randomly oriented nanofibers, which were latter on patterned by masking in conventional UV-lithography (see Figure 3-3b). In short, using a photosensitive material allowed scientists to patterned the randomly oriented fibers into a hierarchically microscopic scale; such structures could have potential in the fabrication of high specific surface area carbon electrodes for electrochemical device applications.<sup>79</sup>

A thorough investigation of the precursor materials that have been employed for CNF deposition in ES is represented in Table 3-1. Furthermore, it discusses the additives used, as well as the polymer machining method that was employed to obtain a configuration of the CNFs (diameter and orientation). It is emphasized that ES is the most widely used technique to pattern CNFs to date. Moreover, PAN is by far the precursor material of choice in both industry and

research.<sup>40</sup> Because extensive review papers have been written on the matter, PAN is omitted in Table 3-1.<sup>40</sup>

**Table 3-1** Polymeric precursors and polymer machining methods used for the production of CNFs and CNWs structures.

Precursor material	Additives	Polymer machining method	Carbon nanowire dimensions	Orientation	Perspective applications	References	
Photoresists	SU-8 (negative tone)	-	Photolithography	sub-micron diameter (~800 nm)	Aligned	Carbon microelectromechanical systems	2,80
	AZ512e (positive tone)	-	Photolithography	thickness: 550 nm	Aligned	Nanomechanical resonators	81
	SU-8 2000	-	Two-Step Photolithography	diameter: 0.21 $\mu$ m, length: 89.4 $\mu$ m	Aligned	Electrochemical and hydrogen gas sensor	38
	SU-8 2000	-	Far field electrospinning	diameter: 190+-40 nm	Random	Electrochemistry electrodes	82
	SU-8 2002	PEO and Tetrafluoroborate tetrabutylammonium salts	Electro-mechanical Spinning	diameter: ~200 nm (min)	Aligned	Carbon microelectromechanical systems	41,44,45
	SU-8-2010	-	Far field electrospinning (rotating drum collector)	diameter: 42.2 nm to 113.0 nm	Aligned	Carbon microelectromechanical systems	383
	SU-8 2015	-	Far field electrospinning	diameter: 198+-11nm	Semi-aligned	Carbon microelectromechanical systems	84
	SU-8 2100	-	Far field electrospinning	diameter: 300 nm - 1 um	Random	-	79
	KMPR	Titanium tetraisopropoxide	Far field electrospinning (rotating drum collector)	diameter: 100-150 nm	Aligned	pH and UV sensor	85
Synthetic polymers	Phenolic Resin	Poly (vinyl butyral)	Far field electrospinning	diameter:~810 nm	Random	Capacitive deionization	86
	Poly(styrene)	poly(carbomethylsilane)	Far field electrospinning	diameter: ~20 nm	Random	-	87
	Poly(styrene)	Polycarbosilane	Far field electrospinning	diameter: ~1 to 2 nm	Random	-	88
	poly(vinyl alcohol)	Multi-element oxide materials (for nanotube formation)	Far field electrospinning	diameter: ~50 to 200 nm	Random	Lithium-ion batteries, sodium-ion batteries, supercapacitors	89
	Poly(vinyl pyrrolidone)	Lithium acetylacetone (LAA) and titanium isopropoxide (TTIP)	Far field electrospinning	diameter: ~200nm	Random	Electrochemical energy storage	90
	Poly-L-lactic acid	Poly(acronitrile), Si nanoparticles	Far field electrospinning	diameter:~200 to 300 nm	Random	Rechargeable lithium-ion batteries	91
	Poly(vinyl alcohol)	Silicon nanoparticles	Far field electrospinning	diameter: 80-200 nm	Random	Lithium-ion batteries	92
	Poly(methyl methacrylate)	Nickel acetate/poly(acronitrile)	Far field electrospinning (rotating drum collector)	diameter: ~200nm	Random	Lithium-ion batteries	93
	Poly(ethylene oxide)	Mg-modified, LiMnPO4	Far field electrospinning	diameter: ~100nm	Random	Lithium-ion batteries	94
	Poly(vinyl chloride)	-	Far Field electrospinning	diameter: ~100nm	Random	High performance Na-ion battery material	95
	Poly (vinyl pyrrolidone)	CdS/TiO2 Nanoparticles	Far Field electrospinning	diameter: ~200 nm	Random	Development of efficient, low cost photocatalysts	96
	Resorcinol-formaldehyde	PMMA	Far Field electrospinning	diameter: ~200 nm	Random	Nerve regeneration	97
	Poly(furfuryl alcohol)	-	Furfuryl alcohol polymerization	diameter: 150-250 nm , length: 10-20 $\mu$ m	Random	Semiconductor nanowire electronics	56,98

### *3.3 Influence of polymer machining methods on the crystallinity of CNWs*

There are numerous methods used to produce nanofibers, which include vapor growth, discharge, laser ablation and chemical vapor deposition. However, these techniques are inherently hindered by their low throughput and expensive equipment required. In contrast, electrospinning (ES) of polymer solutions is a promising technique for the simple and inexpensive fabrication of CNWs, which can be combined with a moving collector to induce further thinning of fibers.<sup>44</sup> For instance, ES has been reported to yield fibers in the 10 nm to 10  $\mu\text{m}$  range.<sup>68</sup> By exploiting both the mechanical stretching of the polymer fiber inherent to ES and the volumetric shrinkage induced by pyrolysis, sub-50 nm CNWs have been produced.<sup>3</sup>

The production of C-MEMS involves two main stages: (i) polymer patterning by such techniques as photolithography, ES, ES combined with lithography, Computer Numerical Control (CNC), molding, hot embossing, and recently, Multiple Photon Polymerization (MPP);<sup>49</sup> (ii) carbonization, resulting in the isometric shrinking of the patterned polymer and its conversion into carbon. In some cases, an additional oxidative stabilization step is used [for instance in polyacrylonitrile (PAN) nanofibers produced by ES] to induce the crosslinking of the polymer chain molecules and prevent melting during subsequent carbonization.<sup>68</sup>

Numerous previous studies show how the heat treatment temperature of the polymer precursor during the pyrolysis step greatly affects the overall crystalline composition of the resulting GC structures.<sup>74</sup> Early GC investigations divided it into two groups, graphitizing and non-graphitizing carbon, depending on the crystalline nature of the produced carbon and its ease of conversion into a more graphitic configuration.<sup>74</sup> For graphitizing carbons, high temperature treatment can result in its complete transformation into graphitic material, while non-graphitizing carbon remains glassy even for high temperature treatments.<sup>74,75,99</sup> Recently, however, non-graphitizing carbon has also been classified into two additional subcategories: Type-I GC, which is composed of randomly distributed and curved graphene planes and; Type-II GC which contains self-organizing nanometer fullerene-like spheroids and three-dimensional graphene flakes.

As mentioned in Section 3.2, randomly electrospun nanofibers that are carbonized typically yield GC Type I structures, as seen by the  $I_D/I_G$  ratio. Several studies by Sharma and coworkers have sought to explore the effects of polymer machining techniques on the composition of the final CNFs structures.<sup>3,82–84</sup> The first attempts by this group replicated the strategy utilized by Steach et al.,<sup>79</sup> and tried to study the effects of the patterning and nanofiber morphology on the overall contact angle measurements.<sup>82</sup> In latter works, Sharma et al. explored the use of PAN and SU-8 photoresist to deposit nanofiber directly on C-MEMS substrates as collector geometries.<sup>84</sup> This addition from previous attempts changed the way in which polymer nanofibers were deposited in the C-MEMS structures. In Figure 3-4a-h, it is shown how nanofibers have a preferential orientation towards the SU-8 walls and are hanged in between posts during deposition,<sup>84</sup> subsequent pyrolysis yields suspended CNF architectures. In their study, Sharma and colleagues showed the fabrication of CNFs from two different precursors; SU-8 2015 and PAN.<sup>84</sup> For the two precursors, they studied the diameter distribution, electrical conductivity, as well as the graphitic composition of the samples via Raman spectroscopy (as seen in Figure 3-4i,j). For the SU-8 derived samples, they obtained an electrical conductivity of  $1.84 \times 10^3$  S/m and  $1.30 \times 10^4$  S/m for PAN samples.<sup>84</sup> In addition, the average diameter of the CNFs ranged in the 198 nm for SU-8 and 217 nm for PAN samples. Furthermore, the ratio ( $I_D/I_G$ ) was characterized for batches of samples, indicating a value of 0.98 and 0.74, for the SU-8 and PAN-derived CNFs, respectively.<sup>84</sup> It can be concluded from their study that PAN-derived CNFs yielded carbon of a higher  $sp^2$  content than for SU-8 samples. Structural characterization was in agreement with the electric conductivity measurements for PAN that show values an order of magnitude higher than those of SU-8. Nonetheless, it is important to mention that while higher graphitic content was achieved by exploring the precursor material, the obtained CNFs still had a Type I-GC composition.

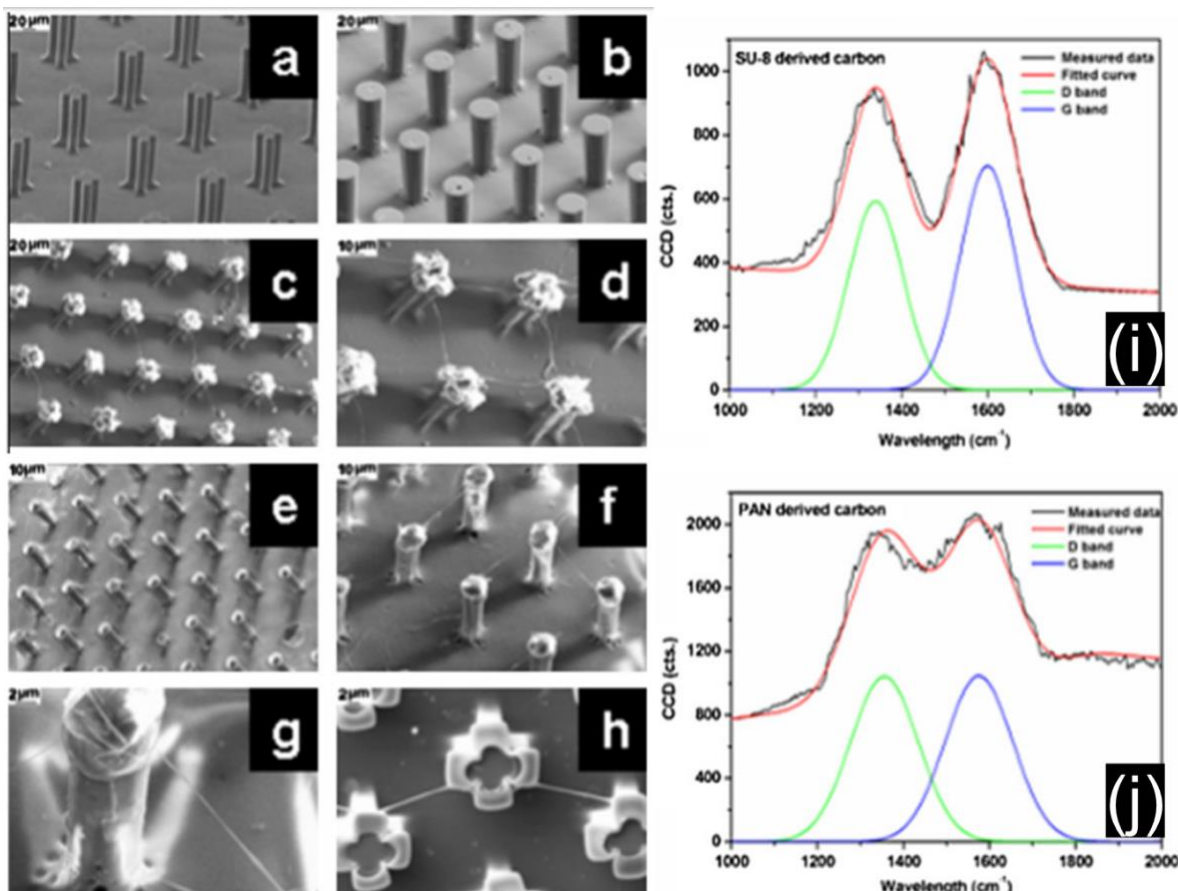


**Figure 3-4.** (a-h) Suspended CNFs produced by pyrolysis of SU-8 polymeric nanofibers produced by FFES directly on C-MEMS electrodes. Raman spectra of (i) SU-8 derived CNFs and (j) PAN derived CNFs. Reprinted and adapted from ref. <sup>84</sup>, Sharma, C. S. *et al.*, *Carbon N. Y.*, **49**, 2011, 1727-32.

The GC-Type I structural conformation of CNFs has been verified in other investigations. For instance, Wang et al. showed that CNFs produced by pyrolysis at different temperatures and times of poly(furfuryl) (PFA) nanofibers resulted in amorphous structures.<sup>100</sup> Interestingly, researchers found in the Raman spectra of the CNFs that the crystallite size of PFA carbonized at 600°C decreased with increasing pyrolysis time.<sup>100</sup> They corroborated this behavior with electrical conductivity measurements of the samples. Further, for CNFs produced at temperatures of 850°C, the CNFs behaved with a semiconductor-like electrical conductivity, which was highly dependent on the temperature in the wire.<sup>100</sup> Crystallite sizes came about 2 nm,<sup>100</sup> which are smaller than those obtained for ES of randomly oriented fibers.<sup>79</sup> Other works on PFA derived CNFs have demonstrated similar trends, with highly amorphous carbon structures.<sup>56</sup> In Figure 3-5a, the suspended CNF is shown, contacting two metallic electrodes. In

addition, Figure 3-5b-d show the structural conformation of the CNF obtained by synthesis in a porous alumina template. In the work by B.A. Samuel et al., it is confirmed that template-based fabrication of CNFs yields structures with semiconductor properties.<sup>56</sup> Conductivity of these CNFs can decrease up to 700% as shown in temperature-dependent measurements.<sup>56</sup>

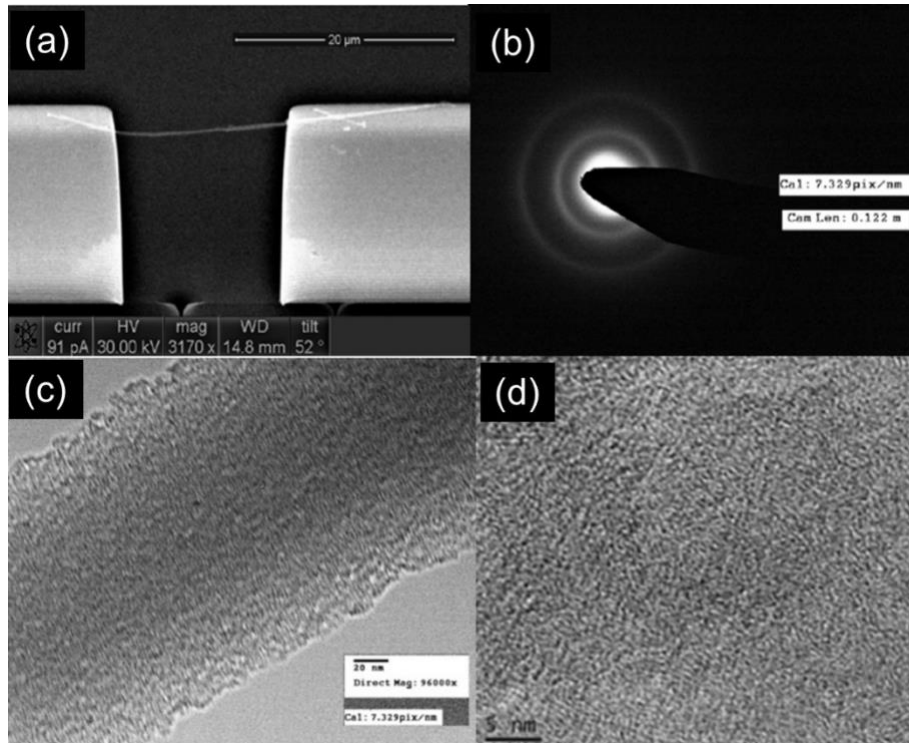


**Figure 3-5.** Suspended CNFs derived from pyrolysis of PFA produced porous alumnia, template techniques. (a) CNF suspended between metallic contacts. (b) Diffraction pattern of the CNF. (c,d) TEM micrograph showing the dimensions and crystallite size present in highly amorphous CNFs. Reprinted and adapted from ref [56]., B. A. Samuel. *et al.*, *Nanotechnology*, **19**, 2008, 275702.

Patterning of suspended CNFs has motivated other works, particularly in the use of ES and lithography as fabrication techniques. One commonly used strategy to achieve straight and parallel CNF arrangements has been with the use of a rotating drum as collector, as seen in Figure 3-6.<sup>3,85</sup> This rotation of the collector introduces two main changes in the patterning mechanism from a basic ES experiment: (i) the rotating drum will help orient the fibers during deposition, since the deposited material will be constantly wrapping around the collector; (ii) a rotating drum at high rpm values will induce a mechanical pulling force along the axis of the polymeric wires.<sup>3</sup> This mechanical pulling force can induce the molecular orientation in the

precursor polymer chains, which in turn will result in an increased graphitization of the CNFs after pyrolysis. Such hypothesis was tested by Swati Sharma et al,<sup>3</sup> in which a rotating drum spinning at 2000 rpm was used to place fibers in short 3-5 s deposition shots.<sup>3</sup> In their work, fibers deposited by this method were proven to have a higher graphitic content. This was verified by electrical conductivity measurements, HR-TEM characterization, Raman spectroscopy and X-Ray diffraction (XRD) analysis.<sup>3</sup> The measured electric conductivity indicated values of up to  $6.96 \times 10^4$  S/m, which is a two-fold increase from the bulk value of GC.<sup>2</sup> Moreover, the CNFs were automatically contacted by carbon walls due to the pyrolysis step, and were shown to have stable ohmic contact at the ends of the wires.<sup>3</sup> The minimum diameters obtained by this method were in the order of 42.2 nm, which are among the lowest observed for CNFs in C-MEMS applications.<sup>3</sup> The structural composition of the CNFs is summarized in Figure 3-7, where the micrographs in (a-d) show the graphitic shell/GC core structure of the samples. The  $I_D/I_G$  was calculated via Raman spectroscopy (Figure 3-7e), indicating a value of 0.61, which was comparatively higher than those obtained in previous studies.<sup>84</sup> Furthermore, XRD analysis (represented Figure 3-7f, where the x-axis is equivalent to  $2\theta$ ) showed the characteristic spike of graphite, along with a significant GC content. Authors report that using a rotating drum conclusively results in CNFs with an increased graphitic content, attributing it to the disentanglement of polymer chains in the precursor prior to carbonization.<sup>3,56</sup>

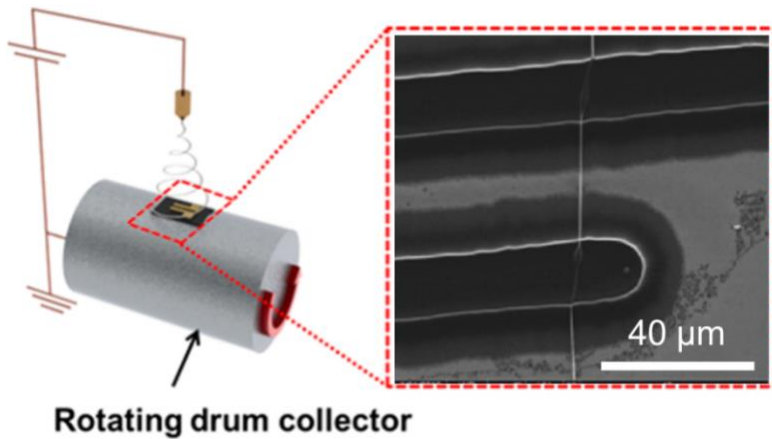


**Figure 3-6.** FFES on a rotating drum collector, which can be used to simultaneously align and stretch polymer nanofibers. Rotating drum schematic adapted from ref. [39] W. S. Lee *et al.*, *ACS Appl. Mater. Interfaces*, 2014, **6**, 12189–12195. The SEM micrograph of CNW was obtained from ref. [3] S. Sharma, *et al.*, *ACS Appl. Mater. Interfaces*, 2012, **4**, 34–39.

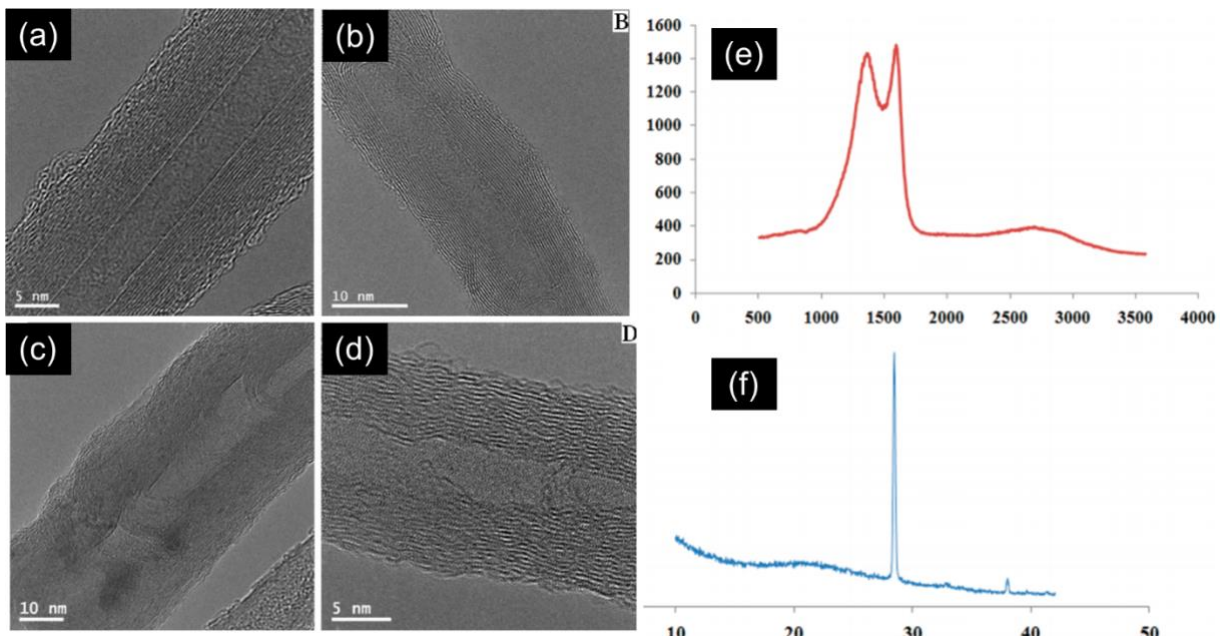


**Figure 3-7.** (a-d) HR-TEM images of CNFs fabricated by using a rotating drum collector, showing an increased graphitic content. In figure (e), the Raman spectra of such CNFs is shown, as well as their X-ray Diffraction pattern in (f). Reprinted and adapted from ref.[<sup>3</sup>], Sharma, S. *et al.*, *ACS Appl. Mater. Interfaces.*, **4**, 2012, 34-39.

One disadvantage of the rotating drum configuration is that the amount of polymeric wires deposited on the substrate cannot be controlled.<sup>3</sup> Often, multiple wires are deposited in a configuration connecting the underlying electrodes, and thus, they must be cut with expensive techniques such as focused ion beam (FIB).<sup>3</sup> It has been widely reported that the bending instabilities of the liquid jet in FFES make it difficult to position of single electrospun fibers in a pattern.<sup>69</sup> On the other hand, in NFES, the reduction of the distance between the needle and the substrate helps alleviate this by working in the stable distance jet.<sup>42</sup> Nonetheless, the reduction of voltage in NFES hinders the stretching of the spun fibers to the nanometric range. To tackle this problem, Bisht *et al.* reported the use of a new electrospinning method referred to as Electro-Mechanical Spinning (EMS), which reduced both the applied voltage and the needle-substrate distance to achieve better deposition control and stretching in the near field range, thus obtaining thinner polymer fibers. However, the results from that research group were achieved by utilizing a high oxygen containing poly(ethylene) oxide PEO as a polymer solution. To produce polymer nanowires using the EMS technique, Canton et al. formulated a SU-8 solution

compatible with pyrolysis at 900°C, which included PEO and tetrabutylammonium tetrafluoroborate (TB-TFB) as additives. This formulation was effectively carbonized due to the high carbon content in the precursor material (SU-8) and the viscoelasticity provided by the PEO (due to its high molecular weight), providing continuous writing of the wires during patterned deposition. Because the resulting structure was deposited onto photolithographically patterned SU-8, the similarity in glass-transition temperature and composition of both the wire and the posts resulting in the monolithic merging of the two structures (see Figure 3-8b). This process resulted in good ohmic contacts between the electrodes and the suspended fiber. EMS-produced carbon fibers had diameters ranging from the micron range, down to 300 nm.<sup>101</sup>

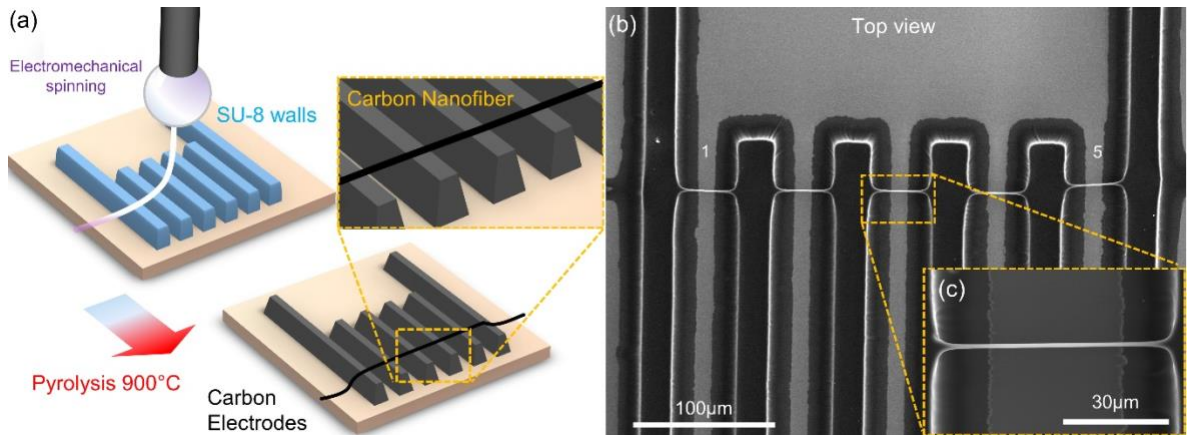


**Figure 3-8.** Polymer machining of SU-8 wires through EMS to produce CNF arrays. (a) Deposition and patterning of SU-8. (b) SEM imaging of the obtained CNWs after carbonization at 900°C.

Photolithography has been extensively used to produce micrometer-scale structures employed in C-MEMS. Special configurations of photolithography, such as two-step lithography can be used to produce nanowire architectures. For instance, Lim et al. produced single suspended carbon nanowires by pyrolysis of SU-8 structures patterned in two steps.<sup>38</sup> In the first step, the supporting walls structures were fabricated. Afterwards, a second coating of the sample through spin coating of SU-8 2000 was followed by UV exposure and subsequent developing. The result was a structure like the one shown in Figure 3-9 (Top, a).<sup>38</sup> Once the structures were fabricated by two-step lithography, the complete nanowire-wall hybrid was pyrolyzed at 900°C to produce suspended carbon nanowires, as seen in Figure 3-9 (Top, b). From this SEM micrograph, the top

part of the supporting walls is shrunk during pyrolysis, but the bottom part, which is firmly anchored to the silicon substrate, is not [Figure 3-9 (Top, b)]. This is because the latter part is not exposed as much as the top part, which is completely open for thermal decomposition during the carbonization step.<sup>38</sup> The method proposed by Lim et al. is highly effective to produce patterned nanowires, which can have the intricate architecture that the masking system allows, as shown in Figure 3-9 (Top, c). It is important to mention that nanofibers produced by this technique have an essentially Type I-GC nature as portraited in the TEM image of Figure 3-9 (bottom, a,b,c).<sup>38</sup> This is likely due to the non-organized nature in which cross-linking occurs in the polymer precursor phase, before carbonization.

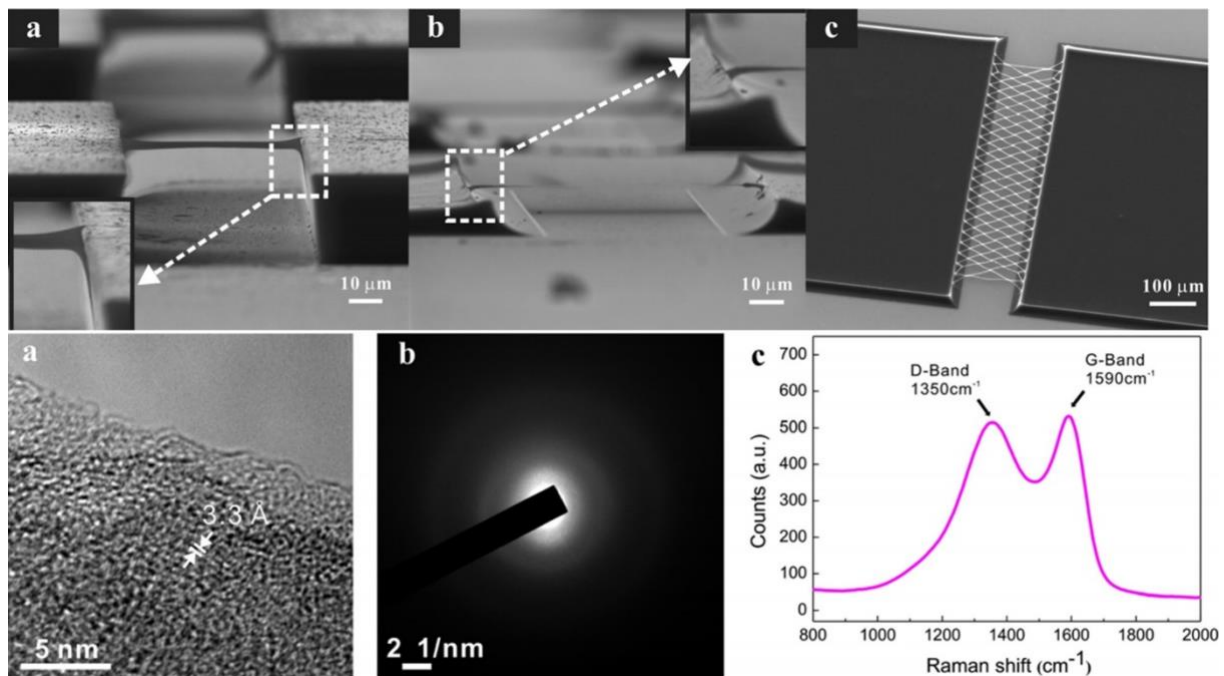


**Figure 3-9.** (Top, a) Single suspended SU-8 2000 nanowire structure before pyrolysis; (inset) anchoring point of the nanowire to the supporting wall. (Top, b) Single suspended CNW, after pyrolysis; (inset) bending of the anchoring point to the supporting wall due to isometric shrinkage during pyrolysis. (Top, c) Example of electrode structures with two-step lithography photo-patterned nanowire network. (Bottom, a) TEM of a carbon nanowire and (Bottom, b) corresponding diffraction pattern. (Bottom, c) Raman spectrum from a carbon post, showing its glassy carbon composition. Reprinted from ref. <sup>38</sup>, Lim, Y. et al., *Nanoscale Res. Lett.*, **8**, 2013, 1-9.

### *3.4 Thermal analysis of CNFs produced by pyrolysis*

An effective way of analyzing the final graphitic content in CNFs produced by pyrolysis of polymeric precursors is by studying how such substances will behave under thermal degradation at given temperatures. To this end, thermogravimetric analysis (TGA) provides an versatile method that can give useful information in regards to the physical and chemical properties of materials, such as phase transition (vaporization, sublimation, absorption, adsorption and desorption).<sup>102</sup> In addition, it can be used to determine the characteristics of materials that suffer thermal decomposition during oxidation or loss of volatile components.<sup>102</sup> If the TGA of polymer precursors (including their additives) are studied, one can draw significant conclusions with regards to the final crystalline content that CNFs will have.

In this regard, TGA has been used to characterize the thermal decomposition of photoresins used in C-MEMS. In their research, Singh and coworkers used TGA along with differential thermal analysis (DTA) (Perkin-Elmer and DTA7) to characterize the pyrolysis process of SU-8 and polyimide (PI) for C-MEMS applications.<sup>103</sup> From the thermal analysis (Figure 3-10a) authors concluded that SU-8 does not start thermal degradation until about 350°C, continuing all the way up to 1100°C. In contrast, polyimide showed a higher weight loss rate than SU-8, starting soon after the 100°C line was passed. Furthermore, as seen from the HR-TEM micrographs in Figure 3-10b,c, the derived carbon is pore free at the nanolevel, indicating thorough annealing of the material.<sup>103</sup> This trait is characteristic of photoresist derived carbons, and is explained by the fact that negative photoresists have long aliphatic carbon chains, which are then cross-linked by a cross-linker molecule.<sup>103</sup> Such aliphatic configuration complicates the ring rearrangement that is needed to form the hexagons present in graphite.<sup>103</sup> In order to exhibit such crystallinities, therefore, higher temperatures are needed for negative photoresist precursors, as shown by Takechi in 2700°C pyrolysis experiments with polyimide.<sup>104</sup>

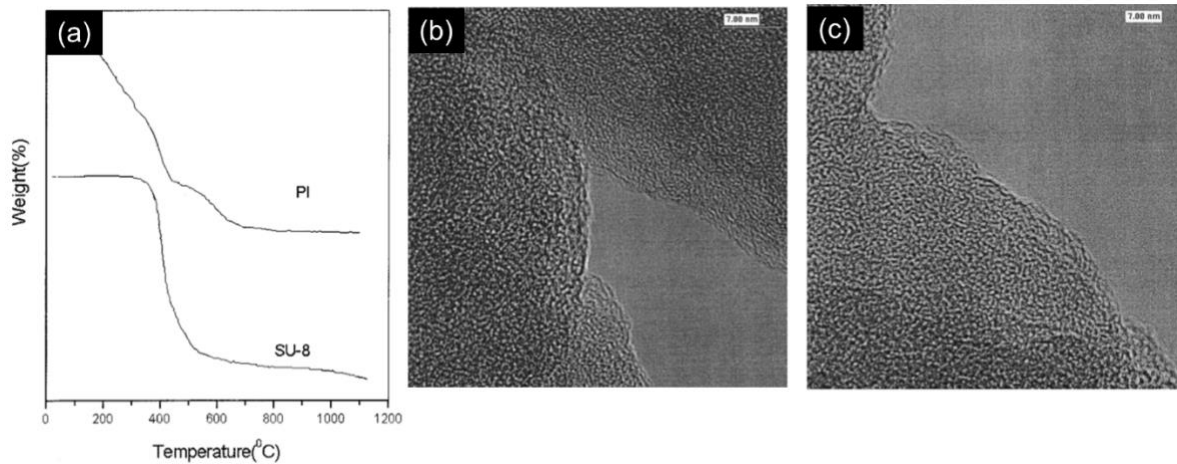


**Figure 3-10.** (a) TGA analysis of SU-8 and polymide C-MEMS precursors. HR-TEM micrograph of (b) SU-8-derived and (c) polymide-derived C-MEMS structures. Reprinted and adapted from ref. <sup>103</sup>, Singh A. *et al.*, *J. Electrochem. Soc.*, **149**, 2002, E78-E83.

It is important to mention that the velocity at which decomposition occurs can be a significant factor in the crystallite sizes of the resulting pyrolyzed CNF. For example, a PEO carrier will counteract the molecular alignment of SU-8 chains due to their structural difference, and hence, the velocity at which it volatizes could impact the crystallization process during thermal ramping in the oven. Moreover, it is expected that the pyrolysis heating rate could influence the way in which the liquid precursor will volatize.

### 3.5 Experimental methods

Polymeric SU-8 nanofibers were produced by two methods which are described in the following sections. For each method, we used different polymer solutions formulations, which would be used to deposit nanofibers on top of the trench formed by the photopatterned SU-8 2015 electrodes described in Section 2.1, thus forming a suspended SU-8 nanofiber. In “Method 1”, fibers were deposited by EMS using a solution that has been previously reported.<sup>44,45</sup> Furthermore, in “Method 2”, a new SU-8 formulation is presented, which was used to deposit 3 mm polymer lines on top of the aforementioned structures. The following sections describe the methodology used to prepare each polymer solution and the deposition protocol.

### *3.5.1 EMS of SU-8 nanofibers by Method 1*

#### *3.5.1.1 Preparation of polymer solution*

The EMS polymer solution consisted of 2ml of SU-8 2002 mixed with 0.5 wt% of Poly(ethylene oxide) (PEO, 4,000,000 MW; SigmaAldrich Inc., Cat. N. 189464) and 0.5 wt% tetrabutylammonium tetrafluoroborate salts (TBATFB; SigmaAldrich Inc., Cat. N. 217964) to increase its conductivity and allow smooth polymer flow during electrospinning.<sup>44</sup> All reagents were used as received. Magnetic stirring of these components was performed for 1hr at 75°C and low rpm (100-150 rpm).

#### *3.5.1.2 Deposition*

A voltage in the range of 100V was applied between a dispensing needle (gauge 32, I.D 132 $\mu$ m) and the collector stage. The needle to collector distance was set to 100 $\mu$ m. Furthermore, the collector was coupled to a mechanically motorized stage, which was used to pattern SU-8 nanofibers into the SU-8 microstructures. Three different stage velocities were tested (20,40 and 60 mm/s) to see the influence on wire geometry; these values were taken from previous works on EMS.<sup>45</sup> Acceleration of the stage was set to 500 mm/s<sup>2</sup>, although this parameter did not perceptibly influenced the deposition velocity. After deposition, samples were exposed to UV light (i-line, 365nm) for 45 min to ensure complete cross-linking.

### *3.5.2 EMS of SU-8 nanofibers by Method 2*

#### *3.5.2.1 Preparation of polymer solution*

A freshly prepared solution consisting of 4ml of SU-8 2025 (MicroChem Corp., MA, USA), 4 mg of TBATFB and 80uL of SU-8 thinner (MicroChem Inc., MA, USA) was stirred for

1.5hr @ 100 rpm at 75°C. All reagents were used as received. Further, the amounts were selected based on previous work from our group.<sup>44,45</sup>

### 3.5.2.2 *Deposition*

To write the fiber exactly on top of the SU-8 electrodes, a routine was set to move the needle relative to the collector. A schematic representation of this is presented in Figure 3-11(a-c). The polymer solution was dispensed at a rate of 8.847 nL/min using a programmable syringe pump (Pump 11 Elite Nanomite) with a gauge 32 (I.D 132 $\mu$ m) needle with a chamfered tip (a characteristic critical for mechanical stability). Afterwards, a voltage of 200V was applied between the collector plate and the needle tip, and the polymer solution was allowed to flow continuously until it was stable (~15 to 30 min). This higher voltage had to be used in contrast to “Method 1” due to the higher viscosity of the SU-8 2025 solution. Once steady flow was achieved, the collector was moved relative to the needle tip using the described motorized stage following the path described by Figure 3-11a. The mechanical parameters used during this deposition step were: a velocity of 5000 $\mu$ m/s, an acceleration of 2500  $\mu$ m/s<sup>2</sup>. Furthermore, the deposition was initiated by approaching the needle to touch the substrate (referred to as contact points in Figure 3-11a), followed by retrieving the needle 1 mm up and subsequently moving it to write the 3mm fiber (see Supplementary video1). After deposition, the sample was exposed to UV light for 45 min to ensure complete crosslinking of the deposited SU-8 nanofiber. Subsequently, the hybrid structure (SU-8 Microstructure + SU-8 nanofiber, Figure 3-11b) was taken into a pyrolysis furnace and were processed according to the protocol indicated in Section 2.1 to obtain the CNW (Figure 3-11c). Finally, the morphology and atomic composition of the obtained samples were characterized using the SEM and EDS equipment described in Section 2.2

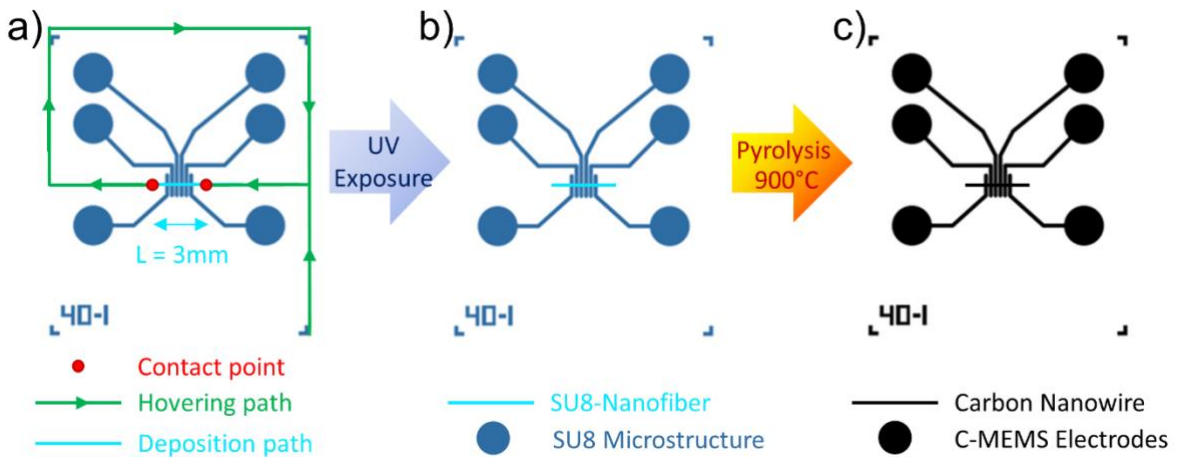


**Figure 3-11.** Schematic representation of the deposition process in EMS. (a) Path taken by the deposition needle relative to the sample, portraying a hovering section (no deposition), contacting points (where the needle comes in contact with the sample) and a deposition segment (where the nanofiber is deposited). (b) Resulting SU-8 Nanofiber from (a). (c) Carbonized sample after pyrolysis, showing the position of the CNW with respect to the device.

### 3.5.3 Characterization of CNWs by Scanning Electron Microscopy

The geometry and morphology of the samples was characterized using the SEM equipment described in Section 2.2. In order to measure the length and diameter of SU-8 polymeric nanofibers, samples were coated with a 5 nm thick layer of gold using a conventional sputter coater (Q150R ES Quorum, Quorum Technologies Ltd, UK). Once pyrolyzed, SU-8 nanofibers are carbonized into CNWs, becoming conductive and therefore, is possible to image them without this additional treatment.

To analyze the SEM micrographs, a MatLab® program was developed which automatically identifies and measures the diameter of nanofiber samples. Briefly, the program uses a pixel counting routine specifically at the region of interest (where the nanofiber is located) and converts the computed amount into a micron scale. In addition, the program can also effectively measure the uniformity of the diameter for each sample.

### *3.5.4 Electric characterization of CNWs*

A Keithley 2636B source meter (Tektronix Inc., OR, USA) was used to run voltage sweeps of CNW and record the electric current. For this purpose, a two-probe approach was used, since contact resistance can be neglected for CNW/C-MEMS hybrid structures.<sup>3,38,44,46</sup> Two kinds of experiments were performed: i) In the first one, voltage was varied from -1V to 1V for I-V curve characterization, for a total of 5 times per sample; ii) The second test consisted in voltage sweeps from different minima ( $-V_m$ ) and maxima ( $V_m$ ), where  $V_m$  varied in magnitude from 1V to 10V. The latter test allowed the determination of the non-linearity of the CNWs from the resulting I-V curves.

## *3.6 Results and discussion*

### *3.6.1 Morphology analysis of samples obtained with “Method 1” vs “Method 2”*

“Method 1” and “Method 2” solutions required different processing parameters due to their difference in viscosity, with solution from “Method 1” being fairly more liquid. This viscosity variance was evident from SEM micrographs. Typical samples from “Method 1” and “Method 2” are shown in Figure 3-12a and Figure 3-12b, respectively. Both samples were deposited on top of SU-8 microelectrodes using mask design “Mask 1” (G40, gap = 40 $\mu\text{m}$ ). Size and morphological differences are evident from these micrographs. While samples from “Method 1” showed microfibers smoothly fused with the supporting electrodes, samples from “Method 2” revealed superimposed fibers sitting on top the electrode structures. Moreover, in Figure 3-12c,d, the diameter profile for each kind of microfiber is presented by taking a 20 $\mu\text{m}$  line profile along their central axis. Evidently, microfibers produced by “Method 1” have a deformation near the anchoring points that widens their geometry and diameter. Indeed, such deformation leads to a standard deviation of the diameter, which is equal to  $\sigma_{M1} = 75\text{nm}$ . On the other hand, microfibers from “Method 2” show very high diameter uniformity, evinced by the absence of deformation towards the anchoring points in the electrodes and a lower standard deviation of  $\sigma_{M2} = 25\text{nm}$ . These observations suggest that microfibers produced from “Method 1” have a different material composition with

higher solvent content than fibers from “Method 2”, even after EMS and UV-exposure. One reason for this could be the solvent content that comes from the polymer solution, with SU-8 2002 having a concentration of solids of 29.00% compared to SU-8 2025, with 68.55%.<sup>105,106</sup>

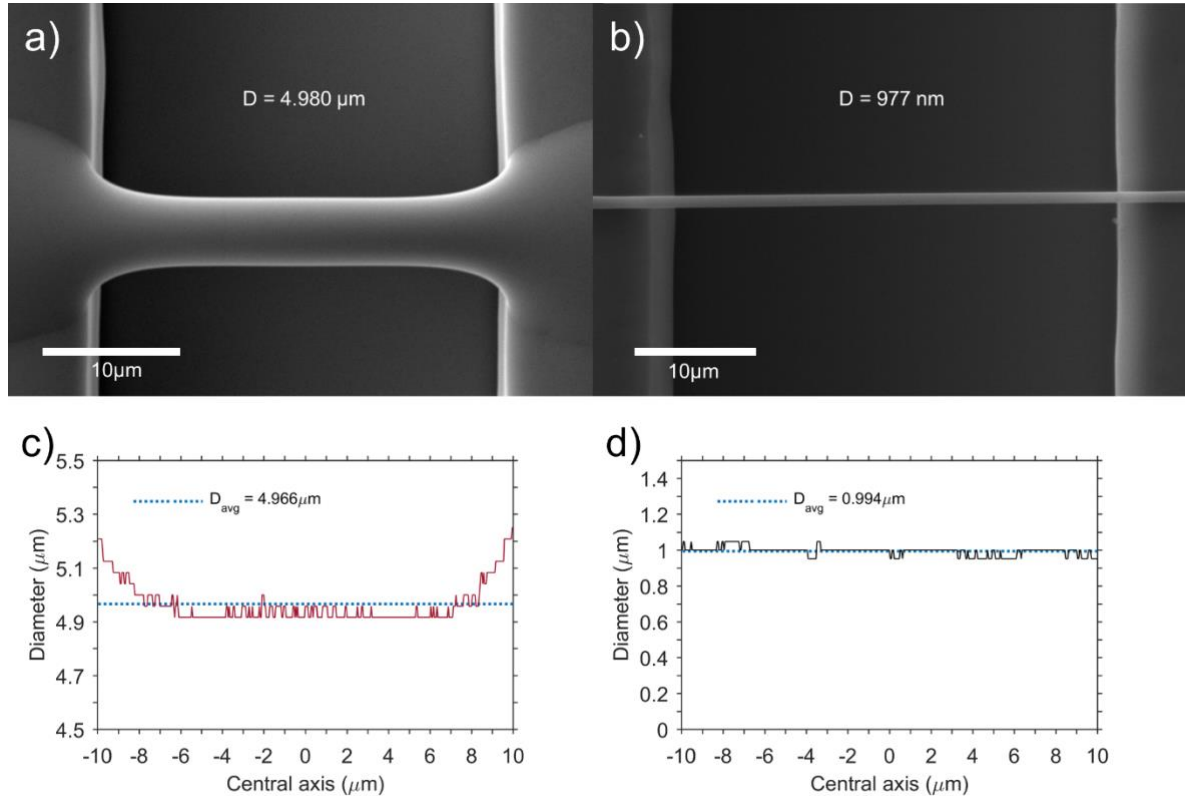


**Figure 3-12.** Top view SEM micrographs of SU-8 fibers deposited on top of SU-8 microstructures. (a) SU-8 microfiber deposited using “Method 1”. (b) SU-8 nanofiber deposited using “Method 2”. (c) Diameter profile for SU-8 microfiber produced by “Method 1”. (d) Diameter profile for SU-8 microfiber produced by “Method 2”.

### 3.6.2 Influence of soft-bake time

To test the hypothesis of a higher solvent content in samples produced by “Method 1”, samples were subjected to a soft-bake step, heating them at 70°C for a minimum time of 60 sec. We found that samples from “Method 2” had little to no change in their morphology after the treatment (and thus, these results are not presented). On the other hand, samples from “Method 1” had a significant change in their morphology and diameter. In Figure 3-13,

the bar plot portraits the diameter variation of fibers as a function of soft-bake time for five samples. Furthermore, in Figure 3-13(i-v) we present a time sequence for one sample subject to a soft-bake temperature of 70°C.

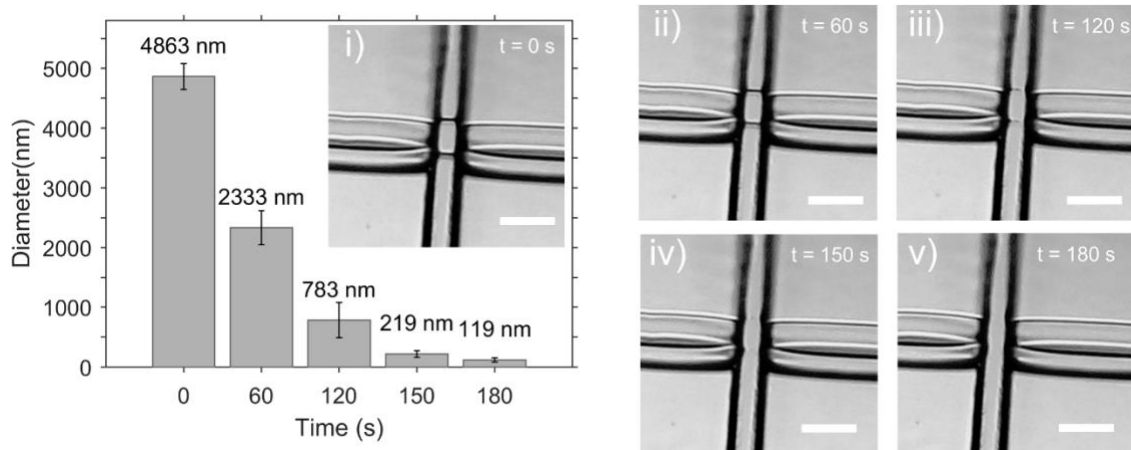


**Figure 3-13.** Bar plot: diameter reduction of SU-8 nanofibers produced by “Method 1”, as a function of soft-bake time (at 70°C). (i) As-deposited fiber at soft-bake time of 0 s; the image was recorded with an optical microscope at a magnification of 200X. (ii-v) Time sequence of the same nanofiber, showing the evolution of fiber diameter. Although it may seem that there are two fibers suspended, the “second fiber” is a reflection on the reflective silicon substrate. All scale bars are equal to 40μm.

Figure 3-14a,b presents two SEM micrographs of nanofiber samples after heat treatment at 70°C, obtained with soft-bake times of  $t = 150\text{s}$  and  $t = 180\text{s}$ , respectively. Thermal processing led to changes in the morphology of the samples, which had a significant diameter reduction in the middle part of their length, compared to their end points. While samples subjected to prolonged heating (Figure 3-14b,  $t = 180\text{s}$ ) suffered the highest volumetric reductions, they often collapsed or broke at the anchoring points. Furthermore, uneven evaporation of the solvent left polymer beads in the fibers (Figure 3-14c,  $t = 180\text{s}$ ), resulting in poor surface uniformity. Lastly, mechanical stability was an issue for sub 200nm diameters, as samples often collapsed after exposure to the electron beam for a couple of minutes (~5kV for Figure 3-14d). From these results, it can be concluded that a heat induced change is evident and that the morphology change can be related to different solvent content in the samples. This typical behavior is also observed in thin film SU-8 materials that shrink after solvent (cyclopentanone) evaporation.<sup>105,106</sup> Even though soft baked samples presented

the smallest diameters obtained so far for SU-8 nanofibers, they were not compatible with the harsh pyrolysis conditions and thus, no CNWs were obtained by this method.

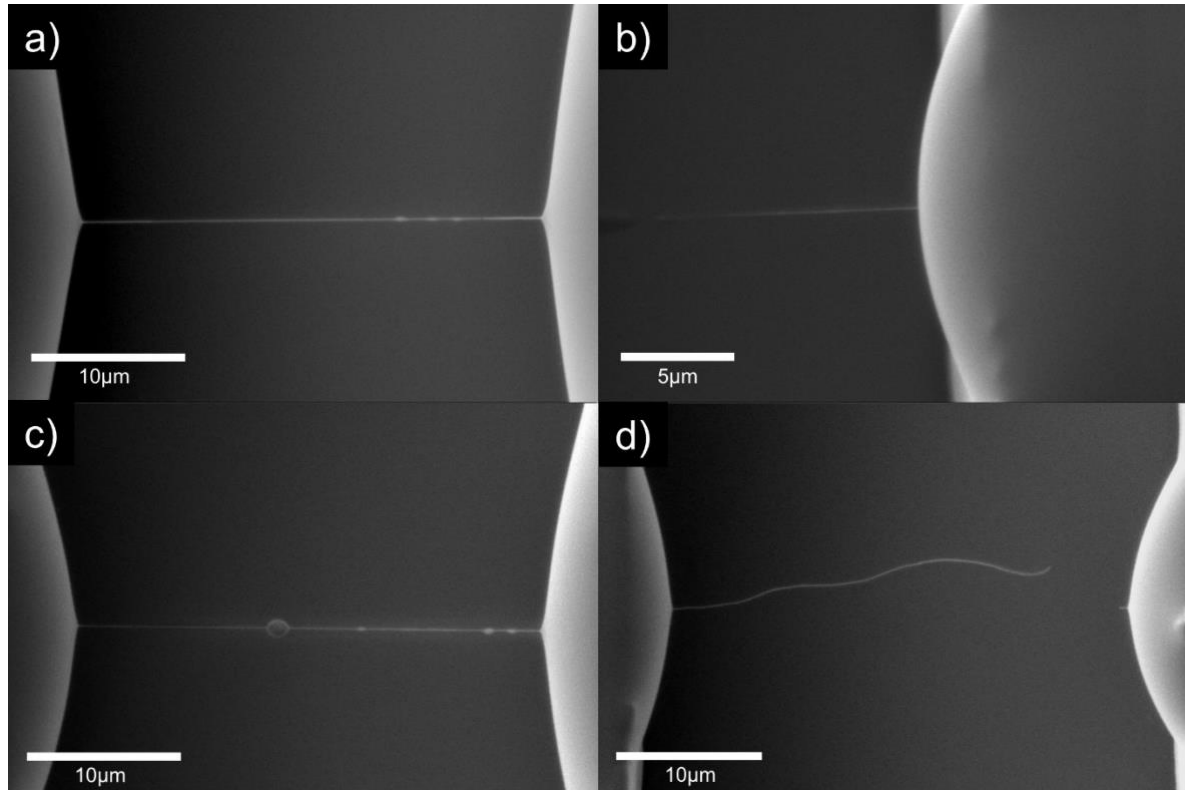


**Figure 3-14.** SEM micrographs of SU-8 nanofibers after soft-bake treatment at 70°C. (a) Micrograph of a fiber sample that is suspended in between two SU-8 electrode structures ( $D = 224\text{ nm}$ , soft-bake time: 150s). (b) Zoomed portion of a nanofiber, showing a collapsed end ( $D = 105\text{ nm}$ , soft-bake time: 180s). (c) Fiber sample showing beads that remained even after soft-bake ( $D = 270\text{ nm}$ , soft-bake time: 150s). (d) A sample fiber that collapsed after prolonged exposure to electron beam (5kV).

### 3.6.3 Analysis of pyrolyzed samples

To explore the possibility of using the SU-8 nanofibers in C-MEMS applications, samples were pyrolyzed in an inert environment to convert them into glassy CNWs.<sup>3,44,46</sup> In the experiments performed for the current dissertation, samples prepared by “Method 1” failed to result in pyrolyzed CNW. This failure is attributed to the fact that SU-8 microwires deposited in this way were mostly liquid before carbonization. Therefore, it is likely that they evaporated during the beginning of the heating process (200~500°C), where plastics lose a

significant amount of volume due to degassing.<sup>55</sup> On the other hand, fibers produced by “Method 1” had a yield rate of 81% (percentage of obtained CNWs from the total amount of pyrolyzed SU-8 microfibers). Figure 3-15a portraits the top view of a pyrolyzed CNW ( $D = 200 \text{ nm}$ ,  $L = 64.2\mu\text{m}$ ), which features a high aspect ratio of 321. In order to have a statistically significant distribution of the diameters after pyrolysis, a total of  $N = 30$  samples were analyzed and measured using SEM micrographs. Size distribution can be appreciated in Figure 3-15c, which shows a normal distribution fit that is in agreement with the obtained data. Therefore, we indicate the mean value of  $204\pm41\text{nm}$  as the benchmark for nanofabrication linewidth resolution offered by the proposed manufacturing methodology. In addition, the resistances of the CNWs were obtained from the I-V curves of the samples, as presented in Figure 3-15b. In this case, the plots for four diameter cases are presented. The tendency for all samples was that of high resistance ( $\sim 8\text{M}\Omega$  range) for thin samples ( $\sim 150\text{-}200 \text{ nm}$ ). This dependence resulted in resistances spanning wide ranges ( $0.1\text{M}\Omega$  to  $\sim 8\text{M}\Omega$ ). A distribution of CNW resistance for 64 samples is presented in a bar plot (Figure 3-15d). This behavior is expected if we consider CNW resistance ( $R = Y$ ) is a function of the normally distributed diameter,  $D = X \sim \mathcal{N}(\mu_X, \sigma_X^2)$ . Assuming this kind of distribution and assuming a linear and ohmic resistance, the expression

$$Y = \frac{4L}{\pi\sigma X^2} \quad (3.1)$$

holds for resistance of a sample. In the previous expression,  $\sigma$  is the conductivity of the CNWs and  $L$  their length. Using Eq.(3.1), it is possible to calculate the probability density function for  $Y$ :

$$f(\omega) = \frac{\Delta}{\sqrt{2\sigma_X^2}} \exp\left(-\frac{(\omega - \mu_X)^2}{2\sigma_X^2}\right) \quad (3.2)$$

where  $\omega = 2\left(\frac{L}{y\pi\sigma}\right)^{1/2}$  and  $\Delta = \frac{\omega}{2y}$ . We performed functional fitting of the randomly distributed data to the presented expression for  $R$ . Experimental distribution data is in good agreement with the functional fit, as seen in Figure 3-15d, where we present the distribution

of the measured  $R$  values, along with a line plot. For this distribution, the expected value lies in  $1.244 \text{ M}\Omega$  and the standard deviation was calculated to be  $1.268 \text{ M}\Omega$ . To perform the fit, the values  $\mu_X$ ,  $\sigma_X$ ,  $L$  and  $\sigma$  were allowed to vary. The obtained values are found to be in the order of the experimental data, confirming the validity of the distribution. The experimental data were  $\mu_X = 204 \text{ nm}$ ,  $\sigma_X = 41 \text{ nm}$ ,  $L = 60.5 \pm 4.3 \text{ }\mu\text{m}$  and  $\sigma = 1488.1 \pm 448.9 \text{ S/m}$ , while the model fitting data corresponded to  $\mu_X = 218 \text{ nm}$ ,  $\sigma_X = 108 \text{ nm}$ ,  $L = 65.197 \text{ }\mu\text{m}$  and  $\sigma = 1630.0 \text{ S/m}$ .

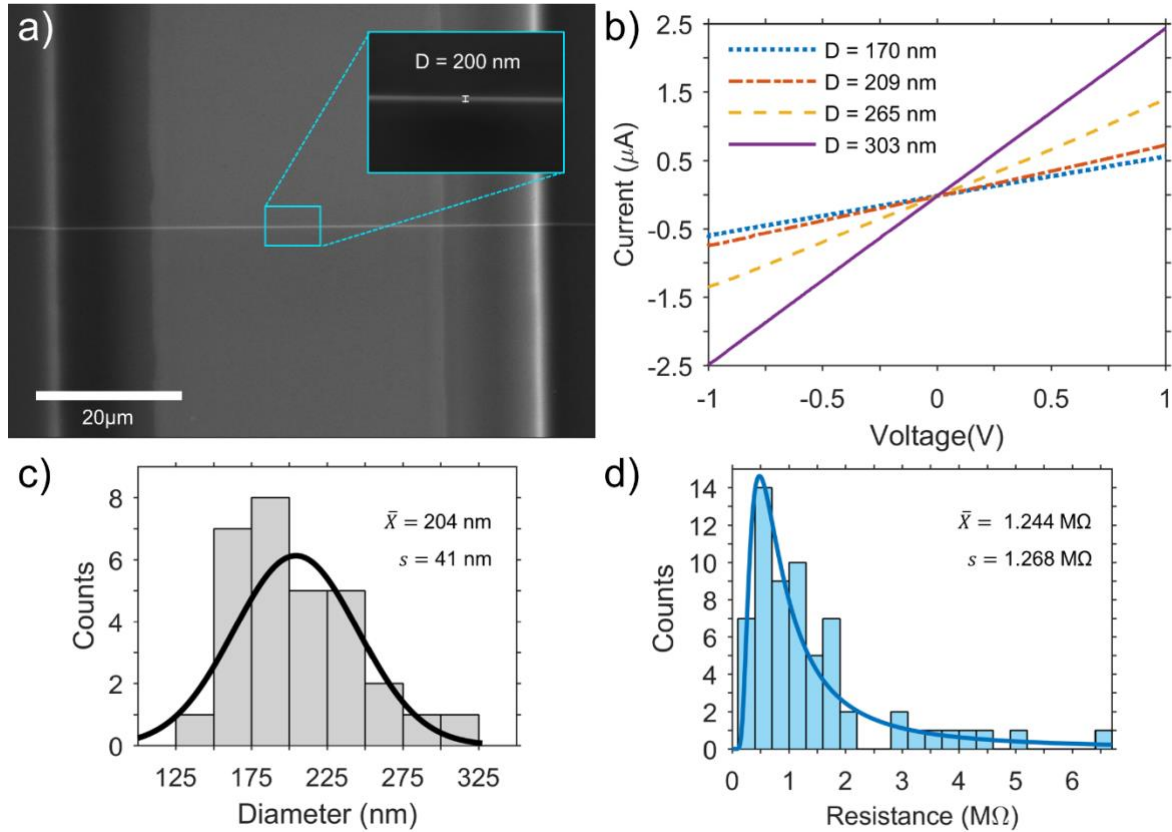


**Figure 3-15.** (a) SEM micrograph (top view) of a pyrolyzed CNW; inset: zoomed portion of the CNW, with a mark indicating the diameter of the sample. (b) I-V curve of four CNW samples of different diameters; the corresponding resistances are  $1.727 \text{ M}\Omega$ ,  $1.371 \text{ M}\Omega$ ,  $0.731 \text{ M}\Omega$  and  $0.407 \text{ M}\Omega$ , for  $D = 170 \text{ nm}$ ,  $209 \text{ nm}$ ,  $265 \text{ nm}$  and  $303 \text{ nm}$ , respectively. (c) Diameter distribution of 30 CNW samples, with mean  $204 \text{ nm}$  and standard deviation of  $41 \text{ nm}$ . (d) Resistance distribution of 64 samples, with mean  $1.244 \text{ M}\Omega$  and standard deviation of  $1.268 \text{ M}\Omega$ .

A statement about the experimental information available in the literature regarding EMS produced CNWs is necessary at this point. Previous experiments on CNWs fabricated with EMS lack specific information about the operating conditions (stage velocity, voltage, dispense rate, needle-to-collector distance, etc.) that lead to specific diameters.<sup>44</sup> Moreover, even when these conditions are specified, they often lead to very wide ranges of linewidth resolution (200 nm to 2.5 $\mu$ m).<sup>44,46</sup> This variability is attributed to the difficulty in producing continuous polymeric fibers from the SU-8 2002 formulation, likely due to its viscoelasticity. On the other hand, the current method offers a systematic way of producing single CNWs, but compromises the ability to make several samples within a device, due to the way in which the polymer jet is initiated (substrate contact). Thus, geometry has to be carefully examined before starting a deposition experiment.

### 3.7 *Summary*

The geometry of CNWs is an important characteristic that will determine the C-MEMS device resistance, ampacity, mechanical and thermal characteristics and crystallinity. This chapter presented some of the techniques and precursor materials that have been used to produce CNWs, as well as the influence that fabrication parameters have on the final geometry of the nanowires. The relative ease of implementation of ES has made it the de facto method for CNW production. EMS, being a relatively new subset of ES, improves on this technique and is a promising AdAM alternative for making highly ordered and individually addressed CNWs. The novelty of EMS, however, brings many unexplored challenges, such as the reproducibility of CNW production. The current fabrication methodology represents an attempt to approach this challenge.

The experiments here presented contrast the available EMS fabrication method with a new alternative of automatically initiated deposition of single CNWs. This new method involved a new polymer solution formulation, in addition to a systematic approach to EMS deposition. It was found that the proposed manufacturing method yielded normally distributed diameters with a mean value of  $\bar{X} = 204$  nm and standard deviation of  $s = 41$  nm, which significantly narrowed the uncertainty in the EMS fabrication standard. The presented method was

evaluated in terms of the obtained morphology and electric characteristics of CNWs. Furthermore, a statistical analysis of the obtained resistance is presented. The presented method of performing a functional fitting to the resistance histogram (for a statistically significant number of samples) allows one to estimate likely values of length, conductivity, diameter and standard deviation of diameters. This is a useful technique, as it can save a significant amount of characterization time (i.e. micrograph measuring) when an estimation of the geometry of the CNWs is needed.

## 4 Microfabrication of Suspended Carbon Nanowires by Multiple-Photon Polymerization

In the last twenty years, Multiple Photon Polymerization<sup>§</sup> (MPP) fabrication has grown into a mature research field of science and technology. Being a subset of advanced additive manufacturing (AdAM), MPP operates at the micro/nano-scale, offering great design flexibility at the cost of fabrication speed.<sup>107</sup> The field of MPP has proven to be an effective method for the fabrication of sub-100 nm nanostructures, where important minimum linewidths and writing resolutions of 9 and 52 nm, respectively, have been achieved.<sup>48</sup> In essence, MPP offers the possibility of producing computer-designed, fully 3D structures with resolutions beyond the diffraction limit, which is an achievement that no other competing technology has attained.<sup>108</sup>

In MPP, pulses from an ultrafast laser are tightly focused into a photosensitive polymer material so that the intensity reached in the focal volume (called *voxel*) is high enough to initiate a polymerization reaction via two-or multi-photon absorption (2PA, MPA), even though the material is completely transparent to the wavelength of the laser.<sup>107</sup> Because of this working principle, almost arbitrarily complex structures can be fabricated by scanning the sample relative to the focus. The variety of 3D photonic crystal structures that have been produced include: woodpile,<sup>109–111</sup> slanted-pore,<sup>112</sup> square,<sup>113</sup> and round spiral photonic crystals,<sup>114</sup> – with and without functional defects, chiral photonic crystals,<sup>115,116</sup> and photonic quasicrystals<sup>117</sup> (see Figure 4-1). Although it could be assumed that almost arbitrarily small features could be generated via MPP, two limiting factors appear in real applications: 1) the instability of the laser source, which makes it difficult to operate at multi-photon resonance; 2) photoresists do not exhibit a sharp threshold of polymerization and in fact, do not allow for a resolution greater than the average size of their building blocks.<sup>107</sup>

---

<sup>§</sup> The Multi-Photon Polymerization (MPP) technique is also known as Direct femtosecond Laser Writing (DLW), Two-Photon Polymerization (TPP), Nonlinear Lithography (NLL) and Multi-Photon Lithography (MPL)

The present chapter aims to describe how the inherent resolution of two photon polymerization (2PP) and three-photon polymerization (3PP) arises from a theoretical perspective. Two of the most common operation modes will be covered: single voxel and scanning voxel line fabrication. By presenting a simplified theory of multi-photon absorption (MPA) phenomena in polymers, we demonstrate how the most important experimental fabrication parameters (such as average power, laser wavelength, repetition rate, pulse duration and tuning of the process) modulate the voxel size. Furthermore, this theory is linked to experimental results in which both common operation modes were tested. The scanning configuration was used to fabricate suspended, 3D polymeric structures that were subsequently carbonized via the C-MEMS methodology to obtain CNWs.



**Figure 4-1.** Types of photonic crystals that have been fabricated by MPP. From top-most image and in clockwise order: slanted pore, square spiral, chiral, quasicrystal, round spiral and woodpile crystal structures. All SEM images were adapted from several sources referenced within the text [109–117].

#### 4.1 Background

The dimension of a structure fabricated by MPP lithography is defined by the combination of three components of the overall system: the laser and the required optics, the photoresist and the photoinitiator<sup>108,118–121</sup> (see Figure 4-2). In the first case, the election of the wavelength of operation will impact the tuning of the MPA process; the type of laser (if it is a continuous wave or pulsed laser) will also play a significant role, and the chosen optics will define the focal length, numerical aperture (NA) and the transmitted power.<sup>122</sup> The photoresist will define the polymerization mechanism (cationic or radical), the ease of cross-linking and the propagation and termination mechanics.<sup>123</sup> Lastly, the photoinitiator will indicate the efficiency of the absorption process as well as the diffusion mechanism from the active species generated at the focal volume.<sup>124</sup>

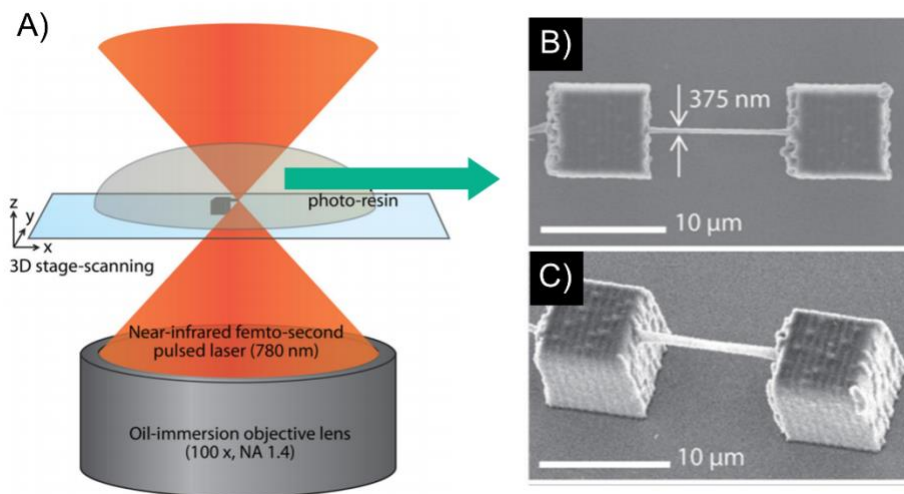


**Figure 4-2.** Overall MPP fabrication scheme. (a) A tightly focused laser beam (near infrared light) is illuminated into a photosensitive resin and the focus spot is moved relative to the scanning stage to fabricate a fully 3D suspended structure. (b,c) An example structure, which illustrates the 3D writing capabilities of MPP. Adapted from ref. [125] S. Ushiba *et al.*, *Adv. Mater.*, 2014, **26**, 5653–5657.

The two most important parameters that indicate the spatial resolution of a photolithographic system are the linewidth and the writing resolution.<sup>48</sup> Linewidth (also named feature size) refers to the size of an isolated fabricated feature, such as a dot or a line (or in the case of 3D fabrication, a voxel). The writing resolution can be axial or lateral, and it is the minimum distance at which two fabricated features can be resolved (with no overlapping between them).<sup>48</sup> The current work will focus on the determination of the

linewidth or feature size, as the writing resolution involves the combination of polymerization reaction mechanisms and mechanical movement of the stage, which are out of the scope of this investigation.

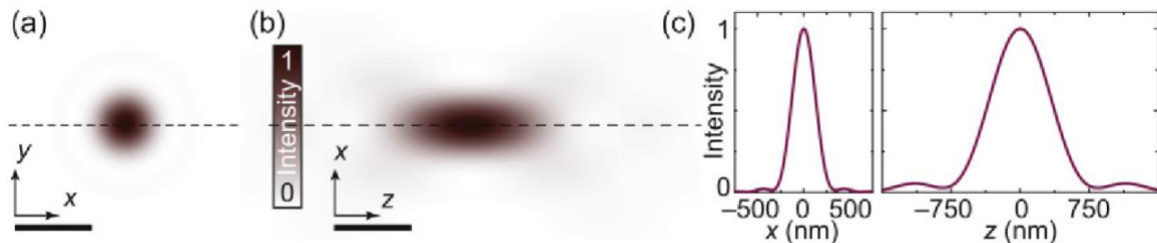


**Figure 4-3.** Light intensity distribution (normalized) showing the Airy pattern in the (a)  $x - y$  plane and (b)  $x - z$  plane. (c) The intensity profile of (a) for a fixed  $y = 0$ . (d) Profile shown in (b) for  $z = 0$ , where clearly the waist is bigger (3 times more) than that of case (b). Plots in (c) were obtained with  $\lambda = 780\text{nm}$  and NA = 1.4. Reprinted from ref [48], T. Baldacchini, *Three-Dimensional Microfabrication Using Two-Photon Polymerization*, 2015, vol. 1542.

The linewidth of a laser-irradiated photoresist will be closely related to the diffraction pattern that comes out of the objective lens. Figure 4-3 shows the diffraction pattern that is produced by the objective lenses when illuminated by a Gaussian profile beam. This distribution is called an Airy pattern and in general it is the diffraction created by a circular aperture. Notice that the central lobe can be approximated to a Gaussian profile in a simplistic approximation (Figure 4-3c). As seen from Figure 4-3a-c, it is evident that the feature size of a voxel is smaller in the lateral direction than in the axial one (usually there is a 3:1 ratio). Taking the case of 1PP (linear absorption), the exposure dose will define the concentration profile of active species in the photoresin after irradiation. Thus, one could expect that the region within the photoresin surpassing the polymerization energy (given by the dose) will experience the nonreversible transformation (for example, a transition from liquid to solid like in photoresin ORMOCER®). We can see this profile in Figure 4-4 (left). On the other hand, if we consider the case of 2PP (Figure 4-4, right), which corresponds to modification to the photoresin material that depends on 2PA events, the modification will modulate as the square of the light intensity, giving a thinner region that surpasses the threshold of polymerization, and therefore a smaller linewidth.

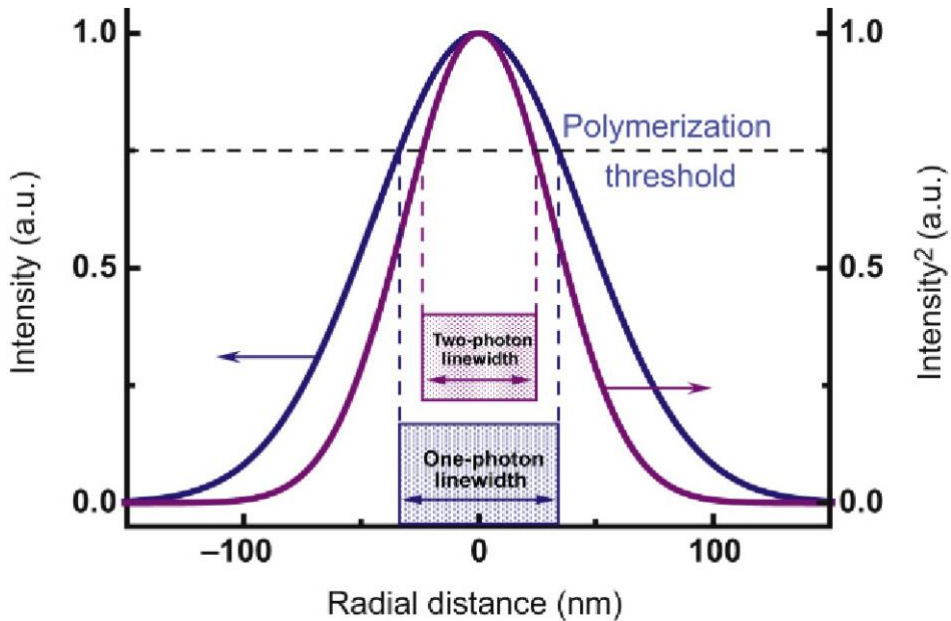


**Figure 4-4.** Exposure region experienced by the photoresist for the case of one-photon polymerization (1PP) at the left axis and 2PP at the right axis. Notice that the 2PP polymerization threshold has a lower linewidth than the 1PP case. Reprinted from ref [48], T. Baldacchini, *Three-Dimensional Microfabrication Using Two-Photon Polymerization*, 2015, vol. 1542.

## 4.2 Mechanisms leading to the smallest MPP features

### 4.2.1 Two beam strategies

In this mechanism, an inhibition/depletion beam is overlapped with the default excitation light beam with the objective of tightly localizing the polymerization volume. The inhibition beam can alternate the state of the molecules between “on” and “off”. This beam then controls the state of the periphery molecules (around the target voxel) to switch them “off”.<sup>126</sup> The suppression of the polymerization in MPP can be achieved through the depletion of the excited state of the photoinitiator via a laser-induced stimulated emission mechanism (stimulated emission depletion, STED).<sup>48,127</sup> Other depletion mechanisms involving two-beam strategies that lead to sub-100nm features include triplet absorption (TA),<sup>128</sup> resolution augmentation through photoinduced deactivation (RAPID)<sup>129</sup> and the two-color photoinhibited super-resolution (PInSR) lithography.<sup>130</sup>

#### 4.2.1 Diffusion assisted approaches

In this technique, only the excitation beam is used, and it consists of the addition of a quencher molecule to the photoresin mixture, which modifies both the polymerization threshold and modifies the surrounding areas due to the diffusion of the quenchers.<sup>131</sup> One of the main features of this technique is that it reduces the “memory effect” (overpolymerization due to overlapping writing patterns), which improves the spatial resolution. This reduction is due to the diffusion of the quenching molecules between the writing steps of two adjacent lines (or features). Table 4-1 summarizes the best linewidth dimensions (or voxel diameter) and writing resolutions achieved up to date.

**Table 4-1.** State of art of the smallest features and writing resolutions achieved by MPP techniques, retrieved from ref. [48]. T. Baldacchini, *Three-Dimensional Microfabrication Using Two-Photon Polymerization*, 2015, vol. 1542.

MPP Mechanism	Experimental conditions		Linewidth (nm)	Writing resolution (nm)	References
	$\lambda$ (nm)	NA			
Two beam approach (STED)	780	1.46	55	120	<sup>127</sup>
Two beam approach (TA)	760	1.4	90	-	<sup>128</sup>
Two beam approach (RAPID)	800	1.45	40 (axial)	-	<sup>129</sup>
Two beam approach (PInSR)	800	1.4	9	52	<sup>130</sup>
Diffusion assisted approach	800	1.4	80-100	400	<sup>132</sup>

#### 4.3 Theoretical Framework of Multiple Photon Polymerization (MPP)

The objective of this section is to present the absorption rates of 2PA and 3PA processes from the quantum mechanical treatment of MPA phenomena. These rates will be related to the absorption cross sections for the cases  $\bar{\sigma}_{ng}^{(2)}$  (for 2PA) and  $\bar{\sigma}_{og}^{(3)}$  (for 3PA) and will be derived following the procedures from Robert Boyd.<sup>133</sup> Subsection 4.3.1 will give the reader an insight of the orders of magnitude of these nonlinear absorption rates and cross sections, and the impact this has in MPP lithography. Following this introduction, subsection 4.3.2 will present a simple theoretical derivation of the spatial limits of MPP in terms of the voxel dimensions, that is, the length of a prolate spheroid of polymerized material ( $l_{voxel}$ ) and its

diameter ( $d_{voxel}$ ). Finally, in subsection 4.3.3 a theoretical derivation of linewidth resolution will be presented and discussed. This type of feature is of keen interest because of its analogy with  $d_{voxel}$ ; while the latter is mainly modulated by exposure time and average laser power ( $P_t$ ), linewidth resolution ( $d_{line}$ ) is modeled via the stage scanning speed  $v_{scan}$  and  $P_t$ .

#### 4.3.1 Theory of 2PA and 3PA absorption rates using Fermi's Golden Rule

We begin by considering an atom in ground state  $g$  and its interaction with an applied monochromatic wave of the form

$$\tilde{E}(t) = E e^{-i\omega t} + \text{c. c.} \quad (4.1)$$

which is applied suddenly at  $t = 0$ . Such atom can be described with its atomic wave-function  $\psi(\mathbf{r}, t)$ , which obeys the time-dependent Schrödinger equation. The Hamiltonian of this system can be represented as  $\hat{H} = \hat{H}_0 + \hat{V}(t)$ , where  $\hat{H}_0$  denotes the Hamiltonian for the free atom and

$$\hat{V}(t) = -\hat{\mu}\tilde{E}(t) \quad (4.2)$$

indicates the interaction energy with the applied optic field, where  $\hat{\mu} = -e\hat{\mathbf{r}}$ .<sup>133</sup> It can be shown (see derivation within Ref. <sup>133</sup>) that  $\psi(\mathbf{r}, t)$  will have the form of a linear combination of eigenstates:

$$\psi(\mathbf{r}, t) = \sum_l a_l(t) u_l(\mathbf{r}) e^{-i\omega_l t} \quad (4.3)$$

with  $\omega_l = E_l/\hbar$  as the frequency associated with the eigenstate  $\psi_l(\mathbf{r}, t) = u_l(\mathbf{r}) e^{-i\omega_l t}$  of the free atom. The term  $a_l(t)$  is a coefficient that can be related to the time-varying probability amplitude that the atom is in the state  $l$ . This coefficient can be readily determined using perturbation theory by introducing the expansion parameter  $\lambda$ ,  $\lambda \in [0, 1]$

$$a_m(t) = a_m^{(0)}(t) + \lambda a_m^{(1)}(t) + \lambda^2 a_m^{(2)}(t) + \dots \quad (4.4)$$

where  $a_m^{(N)}$  for  $N = 1, 2, 3 \dots$  satisfies the set of equations

$$\frac{da_m^{(N)}}{dt} = (i\hbar)^{-1} \sum_l a_l^{(N-1)} V_{ml} e^{-i\omega_{lm} t} \quad (4.5)$$

The relations defined by Eq. (4.5) contain the matrix elements of the interaction Hamiltonian,  $V_{ml} = \int u_m^*(\mathbf{r}) \hat{V} u_l(\mathbf{r}) d^3r$  and the frequency term  $\omega_{lm} = \omega_l - \omega_m$ . By properly defining the boundary conditions, the amplitude  $a_m^{(N)}$  can be determined for any  $N = 1, 2, 3, \dots$ . Furthermore, it can be shown that  $a_m^{(1)}(t)$  becomes resonant when the optic field frequency is  $\omega = \omega_{mg}$ , where the subscript  $m$  denotes an energy state above  $g$ <sup>133</sup>. The case  $N = 1$  describes linear absorption, and is related to transition probability to occupy state  $m$  at time  $t$  (for large  $t$ )

$$p_m^{(1)}(t) = |a_m^{(1)}(t)|^2 = \frac{2\pi|\mu_{mg}E|^2 t}{\hbar^2} \rho_f(\omega_{mg} = \omega) \quad (4.6)$$

where  $\rho_f$  represents density of final states, which is normalized  $\int_0^\infty \rho_f(\omega_{mg}) d\omega_{mg} = 1$ . In Eq. (4.6), the function  $\rho_f$  is to be evaluated at  $\omega_{mg} = \omega$ . Moreover, using Fermi's Golden Rule, Eq. (4.6) can be rewritten as the transition rate

$$R_{mg}^{(1)}(t) = \frac{p_m^{(1)}(t)}{t} = \frac{2\pi|\mu_{mg}E|^2}{\hbar^2} \rho_f(\omega_{mg} = \omega) \quad (4.7)$$

It is convenient to rephrase the transition rate as a function of the experimental intensity of the incident light beam. Conventionally, the intensity of the beam is expressed in photons  $\text{cm}^{-2}\text{sec}^{-1}$ . Introducing  $\bar{I} = \frac{2n\epsilon_0 c}{\hbar\omega} |E|^2$  into Eq. (4.7), the rate is found to be proportional to  $\bar{I}$

$$R_{mg}^{(1)} = \bar{\sigma}_{mg}^{(1)}(\omega) \bar{I} \quad (4.8)$$

where  $\bar{\sigma}_{mg}^{(1)}(\omega)$  is known as the one-photon cross section. Using Eq. (4.5) with the appropriate boundary conditions for other values of  $N$  will give the different cases of MPA. For instance,  $N = 2$  will correspond to the 2PA, which can be expressed as a transition rate in an analogous matter to Eq. (4.8)

$$R_{ng}^{(2)} = \bar{\sigma}_{ng}^{(2)}(\omega) \bar{I}^2 \quad (4.9)$$

where  $n$  represents an energy state above  $m$ .

Continuing the derivation presented by Boyd <sup>133</sup>, we proceed to present  $a_o^{(3)}$  for energy level  $o$  (above  $m$ ) as calculated from Eq. (4.5) for the case of three-photon absorption ( $N = 3$ )

$$a_o^{(3)} = \frac{1}{\hbar^3} \sum_{mn} \frac{\mu_{on}\mu_{nm}\mu_{mg}E^3}{(\omega_{og} - 3\omega)(\omega_{ng} - 2\omega)(\omega_{mg} - \omega)} [e^{i(\omega_{og} - 3\omega)t} - 1] \quad (4.10)$$

which evidently becomes resonant for  $\omega = \omega_{og}/3$ . Starting from Eq. (4.10), the probability of occupying the energy level  $o$  at time  $t$  (for large  $t$ ) will be given by

$$\begin{aligned} p_o^{(3)}(t) &= |a_o^{(3)}(t)|^2 \\ &= \left| \frac{1}{\hbar^3} \sum_{mn} \frac{\mu_{on}\mu_{nm}\mu_{mg}E^3}{(\omega_{ng} - 2\omega)(\omega_{mg} - \omega)} \right|^2 t 2\pi\rho_f(\omega_{og} = 3\omega) \end{aligned} \quad (4.11)$$

which translates to a transition rate

$$R_{og}^{(3)} = \bar{\sigma}_{og}^{(3)}(\omega) \bar{I}^3 \quad (4.12)$$

where  $\bar{\sigma}_{og}^{(3)}(\omega)$  is expressed as

$$\bar{\sigma}_{og}^{(3)}(\omega) = \frac{\omega^3 \pi}{4n^3 \epsilon_0^3 c^3 \hbar^3} \left| \sum_{mn} \frac{\mu_{on}\mu_{nm}\mu_{mg}}{(\omega_{ng} - 2\omega)(\omega_{mg} - \omega)} \right|^2 \rho_f(\omega_{og} = 3\omega) \quad (4.13)$$

Often, a simplified estimation of the  $N$ -photon absorption cross section is provided by  $\bar{\sigma}^{(N)} = (\bar{\sigma}^{(1)})^N \tau^{N-1} [\text{cm}^{2N} \text{sec}^{N-1}]$ , where  $\tau$  is the virtual state lifetime ( $\tau \approx 10^{-16} \text{sec}$ , based on the uncertainty principle) and  $\bar{\sigma}^{(1)}$  is approximated to the geometrical cross section of the absorbing molecule (typically  $\Delta S \approx 10^{-16} \text{cm}^2$ ) <sup>108,134</sup>. On that ground, the three-photon absorption cross section is of the order of  $\bar{\sigma}^{(3)} \approx 10^{-80} \text{cm}^6 \text{sec}^2$ . Furthermore, this relationship can be used to claim that the probability ratio between 2PA and 3PA is

approximately  $\bar{\sigma}^{(1)}\tau \approx 10^{-32} \text{ cm}^2\text{sec}$ <sup>108</sup>. Boyd uses the derivation for  $\bar{\sigma}_{ng}^{(2)}(\omega)$  to provide an estimate of  $\bar{\sigma}_{ng}^{(2)} \approx 2.5 \times 10^{-58} \text{ m}^4\text{sec}$ ,<sup>133</sup> which compares to the above calculation ( $\bar{\sigma}^{(2)} = (\bar{\sigma}^{(1)})^2\tau^1 = 10^{-54} \text{ m}^4\text{sec}$ ) and to other reports which place the TPA as high as  $1.1 \times 10^{-54} \text{ m}^4\text{sec}$  for dendrimer molecules (see Drobizhev *et al.*<sup>135</sup>).

The orders of magnitude calculated above imply that 3PA becomes an important phenomenon at peak intensities of about  $100 \text{ GW/cm}^2$ <sup>108</sup>. Higher order absorption processes for  $N = 4, 5, \dots$  are less probable and might be physically unrealizable because of the required intensities being over  $10 \text{ TW/cm}^2$ , which surpass the optical breakdown of dielectric materials.<sup>134,136</sup>

#### 4.3.2 Dependence of voxel resolution on process parameters

In MPA and MPP, a pulsed, focused laser beam is employed. If the intensity distribution of the laser beam at the focal plane is assumed to be Gaussian, it can be written as

$$I(r, z = 0, t) = I_0(t)e^{-2r^2/w_0^2} \quad (4.14)$$

where  $r$ ,  $I_0$  and  $w_0$  are the radial coordinate, the beam intensity at the central axis in the focal plane and the radius of the focused beam spot, respectively.<sup>137</sup> Further, the geometry of the beam shape along the optical axis ( $z$ ) can be expressed by

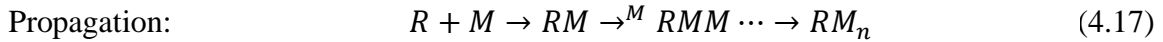
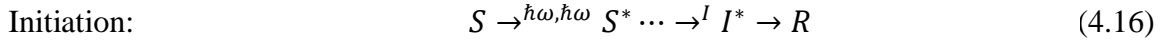
$$I(r, z) = \frac{2P_t}{\pi w(z)^2} \exp\left[-\frac{2r^2}{w(z)^2}\right] \quad (4.15)$$

where

$$w(z) = \frac{\lambda}{\pi \tan[\sin^{-1}(NA/n)]} \left[1 + \left(\frac{\lambda z}{\pi w_0^2}\right)\right]^{1/2}$$

Here, we have introduced the radius of the focused beam along the optical axis  $w(z)$ , the wavelength of the light beam  $\lambda$ , the index of refraction of the immersion oil  $n$  and the value of the numerical aperture, NA.

The laser described by Eqs. (4.14) and (4.15) is used to stimulate a liquid (or solid) resin that is effectively transparent to near-infrared radiation.<sup>137</sup> This allows the laser to affect only a localized spot within the resin volume, which polymerized and is denominated *voxel* (volume pixel). Photon dose and intensity are usually relevant parameters in the modification induced by the absorbed optical beam at the focus spot. This modification by an  $N$ -photon process scales as  $\propto I^N$ ,<sup>108</sup> as demonstrated by Eqs. (4.8), (4.9) and (4.12). Within the polymer material, there will usually be photo sensitizers and photoinitiators which exhibit a reactivity dependent on this  $\propto I^N$  process. In the case of two-photon polymerization (2PP) mechanism can be described as follows:



Equations (4.16) to (4.18) describe the interactions of the photosensitizer ( $S$ ) and its excited state after photon absorption ( $S^*$ ), the photoinitiator ( $I, I^*$ ), the radical or cation ( $R$ ) and the monomer ( $M$ ). The rate of change of the density of radicals  $\rho(r, z, t)$  that is produced by the femtosecond pulses (for 2PA) is assumed to be proportional to the transition rate given in Eq. (4.9), so that

$$\frac{\partial \rho}{\partial t} = (\rho_0 - \rho)\sigma_2 \bar{I}^2 \quad (4.19)$$

where  $\rho_0$  is the initial density of radicals and  $\sigma_2 = \bar{\sigma}_{ng}^{(2)}\eta$  is the effective two-photon cross section for the generation of radicals, which is defined by the product of the TPA cross section and the efficiency of the initiation process,  $\eta < 1$ .<sup>138</sup> Polymerization is defined to occur at any point within the resin volume where a minimum concentration threshold of radicals is achieved, so that  $\rho(r, z) \geq \rho_{th}$ . Moreover, the photon flux is taken as constant for the duration of the pulse,  $\bar{I}(t) = \bar{I}_0$ . By neglecting the loss of radicals in between pulses, the

voxel diameter and length ( $d_{\text{voxel}}$  and  $l_{\text{voxel}}$ , respectively) can be estimated for the total effective exposure time  $t_{\text{eff}}$ , which we define as

$$t_{\text{eff}} = n\tau_L \quad (4.20)$$

where  $n = \nu t_{\text{exp}}$  is the number of pulses,  $\nu$  corresponds to the pulse repetition rate and  $t_{\text{exp}}$  is the total exposure time (see Figure 4-5).<sup>111</sup> To derive  $d_{\text{voxel}}$  and  $l_{\text{voxel}}$ , notice that the solution to Eq. (4.19) can be written as

$$\int_{\rho_0}^{\rho_{\text{th}}} \frac{d\rho}{\rho_0 - \rho} = \sigma_2 \bar{I}^2 \int_0^{t_{\text{eff}}} dt \rightarrow \ln\left(\frac{\rho_0}{\rho_0 - \rho_{\text{th}}}\right) = \sigma_2 \bar{I}^2 t_{\text{eff}}$$

Plugging the form for  $\bar{I}^2 = \bar{I}_0^2 \exp(-4r^2/w_0^2)$  and noting that the threshold condition requires that  $\rho(d_{\text{voxel}}/2, z) = \rho_{\text{th}}$  (implying  $-4r^2 = d_{\text{voxel}}^2$ ), we find that

$$d_{\text{voxel}}(\bar{I}_0, t_{\text{exp}}) = w_0 \left[ \ln\left(\frac{\nu t_{\text{exp}} \tau_L \sigma_2 \bar{I}_0^2}{C}\right) \right]^{1/2} \quad (4.21)$$

$$C = \ln\left(\frac{\rho_0}{\rho_0 - \rho_{\text{th}}}\right)$$

It is convenient to rewrite  $\bar{I}_0$  as a function of experimental parameters

$$\bar{I}_0 = \frac{2}{\pi w_0^2 \tau_L} \cdot \frac{P_t \mathcal{T}}{\nu \hbar \omega_L} \quad (4.22)$$

where  $P_t$  is the average power,  $\mathcal{T}$  is the fraction of transmitted light through the objective and  $\omega_L = 2\pi/\tau_L$ . Because the axial light distribution differs from the radial one, we must consider this in the calculation of  $l_{\text{voxel}}$ . It is sufficient to perform the same calculation only changing the axial light distribution to  $\bar{I}(z) = \bar{I}_0/(1 + z^2/z_R^2)$  at  $r = 0$ , which yields

$$l_{\text{voxel}}(\bar{I}_0, t_{\text{exp}}) = 2z_R \left[ \left( \frac{\nu t_{\text{exp}} \tau_L \sigma_2 \bar{I}_0^2}{C} \right)^{1/2} - 1 \right]^{1/2} \quad (4.23)$$

here we have introduced the Rayleigh length, defined as  $z_R = \pi w_0^2 / \lambda$ .

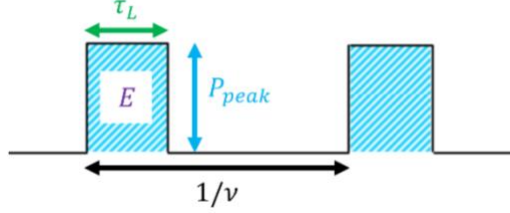


**Figure 4-5.** Simplified scheme for a pulse train, illustrating the pulse duration  $\tau_L$ , repetition rate  $v$ , peak power  $P_{peak}$  and energy per pulse  $E$ .

Because the 3PA version of Eq. (4.19) can be simply stated as

$$\frac{\partial \rho}{\partial t} = (\rho_0 - \rho) \sigma_3 \bar{I}^3 \quad (4.24)$$

its solution follows the exact same procedure as above, concluding that

$$d_{voxel}^{(3)}(\bar{I}_0, t_{exp}) = w_0 \left[ \frac{2}{3} \ln \left( \frac{\nu t_{exp} \tau_L \sigma_3 \bar{I}_0^3}{C} \right) \right]^{1/2} \quad (4.25)$$

And in fact

$$d_{voxel}^{(N)}(\bar{I}_0, t_{exp}) = w_0 \left[ \frac{2}{N} \ln \left( \frac{\nu t_{exp} \tau_L \sigma_N \bar{I}_0^N}{C} \right) \right]^{1/2} \quad (4.26)$$

Similarly, the length of the voxel for  $N$  will be given by

$$l_{voxel}^{(N)}(\bar{I}_0, t_{exp}) = 2z_R \left[ \left( \frac{\nu t_{exp} \tau_L \sigma_N \bar{I}_0^N}{C} \right)^{1/N} - 1 \right]^{1/2} \quad (4.27)$$

It is normally expected that going up from  $d_{voxel}^{(2)}$  to  $d_{voxel}^{(3)}$  the reduction factor will be of about 38%.<sup>139</sup>

#### 4.3.3 Linewidth resolution in scanning writing configuration

We proceed to calculate the diameter of a polymer nanostructure that can be created by scanning a Gaussian profile along a straight-line path. This problem is different from the one

presented in subsection 4.3.2 in that there is no direct time of irradiation, but rather the known velocity of the traveling Gaussian beam acts as a changing intensity profile that imparts an effective exposure dosage to the material volume. The derivation that follows is completely based on the work of Carsten Eschenbaum, which was a part of his Ph. D. dissertation.

We begin by writing the photon flux profile of a traveling Gaussian beam, which can be represented as

$$\bar{I}(x, y, z = 0, t) = \bar{I}_0 \exp(-2((x_c - x)^2 + (y_c - y)^2)/w_0^2) \quad (4.28)$$

where again a constant photon flux  $\bar{I}_0$  has been assumed, and  $(x_c, y_c)$  corresponds to the moving center of the profile. We will assume a scanning movement only in the  $y$  direction so that  $y_c$  can be written as  $y_c = v_y t'$  (see Figure 4-6). Taking again Eq. (4.19) as the starting point, we notice that the problem reduces to a matter of calculating  $C$  for the new moving Gaussian case

$$\int_{\rho_0}^{\rho_{\text{th}}} \frac{d\rho}{\rho_0 - \rho} = C = \sigma_2 \int_{-\infty}^{\infty} \bar{I}^2 dt'$$

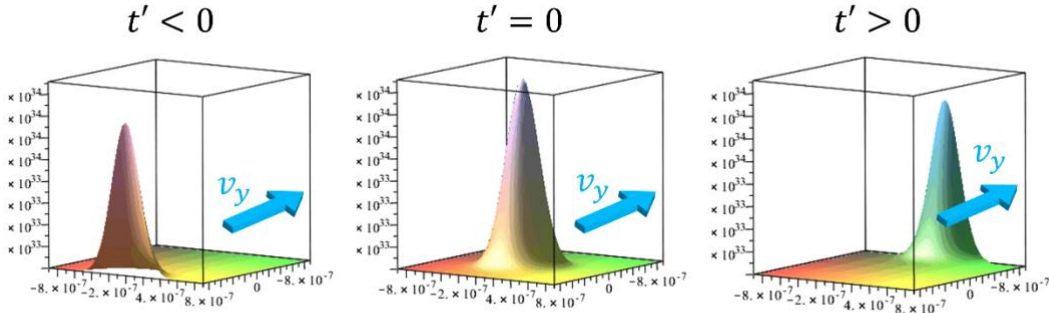


**Figure 4-6.** Traveling Gaussian profile representing the magnitude of the photon flux, with movement in the  $y$ -axis for three different times of exposure. The point of observation corresponds to  $x = 0, y = 0$ . Axis are not to scale. Adapted from thesis dissertation in ref. [140] C. Eschenbaum, 2016.

only now  $\bar{I}(x, y, 0, t')^2$  has a direct dependence on  $t'$ . Notice that the limits of the integral are taken from  $(-\infty, \infty)$  because, as seen from Figure 4-6, the exposure at a single observation point depends on the integrated photon flux before and after the profile crosses that point. Plugging in Eq. (4.28) into the above expression yields

$$C = \sigma_2 \int_{-\infty}^{\infty} \bar{I}_0^2 \exp\left(-4(x^2 + (v_y t')^2)/w_0^2\right) dt' \quad (4.29)$$

where we have introduced  $y_c = v_y t'$  and we set  $x_c = 0$  because we will only observe the change in the voxel linewidth at the origin. Next, we make the following approximations: 1) The photon flux is considered to be constant for the duration of the pulse. However, the integral in Eq. (4.29) assumes that the photon flux present for the duration of the whole irradiation time (not only at the combined time of the pulses durations). To fix this inconsistency, we multiply the integral term by the effective fraction of the time that the sample is being illuminated, which is given by  $v\tau_L$ . 2) We neglect the drop of radicals between laser pulses. Then the solution to Eq. (4.29) can be written as

$$C = \sigma_2 \bar{I}_0^2 \exp\left(-\frac{d_{line}^2}{w_0^2}\right) \left(\frac{\sqrt{\pi} w_0}{2v_y}\right) (v\tau_L) \quad (4.30)$$

Here, we have used the fact that  $d_{line}^2 = 4x^2$ , because we have set the threshold to be  $\rho = \rho_{th}$  at  $2x = d_{line}$ . Solving for  $d_{line}$  we obtain the following expression

$$d_{line} = w_0 \left[ \ln\left(\frac{v\tau_L \sqrt{\pi} w_0 \sigma_2 \bar{I}_0^2}{2v_y C}\right) \right]^{1/2} \quad (4.31)$$

Figure 4-7 shows the resolution (or diameter) dependence on fabrication parameters for the two different configurations (voxel exposure and scanning) described in this work. In Figure 4-7a, the diameter of a voxel dependence on exposure time presented on Eq. (4.21) is plotted for three different values of  $P_t$ . Analogously, Figure 4-7b presents the dependence of voxel linewidth with scanning velocity  $v_y = v_{scan}$ , given by Eq. (4.31).

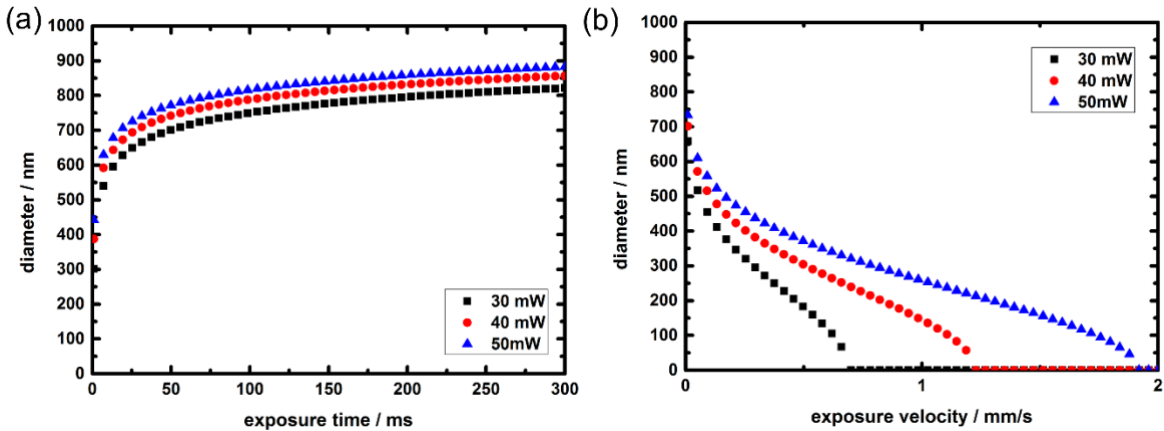


**Figure 4-7.** Theoretical voxel diameter for different values of  $P_t$  for the material SU-8 2050. (a) Diameter of voxel in the case of direct exposure; Dosage is given by  $D_{voxel} = v\tau_L t_{exp} P_t^2$ . (b) Diameter of voxel in the case of scanning configuration; Dose is given by  $D_{line} = v\tau_L \frac{\sqrt{\pi}w_0}{2v_y} P_t^2$ . Adapted from thesis dissertation in ref. [140]

C. Eschenbaum, 2016.

#### 4.4 Experimental methods

##### 4.4.1 Photoresist preparation

Silicon squared substrates (Si, 2 cm x 2cm, thickness 525  $\mu\text{m}$ ) were cleaned using a 5-min acetone ultrasonic bath, followed by 5-min rinsing with isopropyl alcohol under the same conditions. Substrates were then taken to an oxygen plasma treatment for further cleaning (2 min). Afterwards, SU-8 2050 was spin coated for 10s at 5000 rpm (accel: 100 rpm/s) followed by 30s at 3000 rpm (accel: 300 rpm/s) to evenly spread a photoresist thin film. Using these specifications, the thickness of the obtained film was 43  $\mu\text{m}$  thick, which was measured using a Bruker Dektak XT profilometer. Soft-bake was carried out at 95°C for 8 min. Samples were then taken to the TPP setup for exposure. Following this step, post-exposure bake of the samples was performed at 95°C for an additional 8 min to complete the cross-linking process. Finally, samples were taken to developing using SU-8 developer (mr-Dev 600, Micro Resist Technology GmbH, Germany) for 8 min in sonication.

#### *4.4.2 Two Photon Polymerization (TPP) experiments*

SU-8 2050 microfibers were prepared for exposure with a TPP set-up. The complete description of this arrangement can be found in previous publications.<sup>47,141</sup> Briefly, polymerization was induced by a femtosecond pulsed laser (Coherent Mira 900D titanium:sapphire laser) with central wavelength of 800 nm and pulse period of 150 fs, at a repetition rate of 76 MHz. Pumping was used for this purpose, using a Neodymium-doped yttrium orthovanadate (Nd:YVO<sub>4</sub>) laser. The femtosecond laser was coupled to a conventional upright optical microscope (Zeiss Axioplan) using free space optics. Focusing was performed using an Apochromat 100x oil immersion objective (NA 1.4). Before entering the optical microscope, the laser beam was expanded 7x using a Linos beam expander in order to minimize the focal spot. Furthermore, a three-axis nanometer positioning stage (PI P-563.3CD) was used to scan the focal spot into the photoresist sample. Additionally, an automatic shutter (Thorlabs SC10), motorized gradient neutral density (ND) filter and photodiode (Thorlabs DET 110) were used to control exposure time and transmitted power of the laser. To ensure stability of the femtosecond laser setup, room temperature was controlled and regularly monitored (21°C).

In order to produce suspended SU-8 2050 microfibers on a non-transparent substrate (Si) that was robust enough to withstand pyrolysis conditions (900°C), a vertical exposure configuration was used (see Figure 4-8i). A schematic representation of the exposure procedure used to produce the SU-8 wires is presented in Figure 4-9a. A total of 15 pairs of posts were fabricated per silicon substrate using a laser power of 0.2 mW to 3 mW. Posts were 5µm tall, 5µm wide and 80 µm long. Additionally, the separation between posts was fixed to 10 µm. The number of wires for each pair of posts was set to 19, varying scanning velocity from 0.2mm/s to 2 mm/s (although depending on the effective dosage, not all of the structures were completely cross-linked). After exposure, samples were developed using the conditions mentioned in the previous section (Figure 4-8ii). It is important to mention that in order for samples to be fixed to the substrate (as presented in Figure 4-8ii), the vertical region where SU-8 lies must be manually located by monitoring the intensity of fluorescence with

a CCD camera while varying the focal distance to the sample. Furthermore, this fluorescence must be induced with a low laser power (0.8 mW in our case) to prevent polymerization prior to fabrication start up. When the focal spot was within the immersion oil, no characteristic fluorescence response was recorded (Figure 4-10a,b). Once the focal spot reached the SU-8 interface, the fluorescence readout was evident (Figure 4-10c,d), followed by a fully measurable fluorescence peak (Figure 4-10e,f) when 1-2  $\mu\text{m}$  into the sample. Further movement of the focal spot eventually disappeared the fluorescence signal, indicating that the silicon/photoresist interface was found. This procedure was repeated two times at relative coordinates to define a plane ( $300\mu\text{m}^2$ ) which described the orientation of the sample.

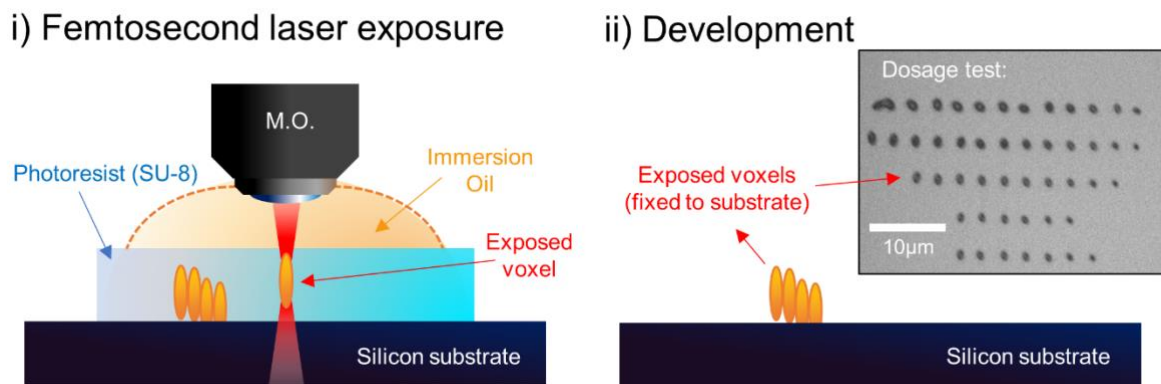


**Figure 4-8.** TPP Vertical exposure setup. (i) Microscope Objective (M.O.) was directly coupled to the SU-8 2050 film using an immersion oil (NA = 1.4). In order to fix structures to the substrate, exposure was started at the SU-8/Si interface. (ii) After development, the unexposed photoresist is removed and only voxels remain. (Inset) An optical microscope image of a dosage test performed on a silicon substrate, featuring lines of individual voxels produced with different exposure times.

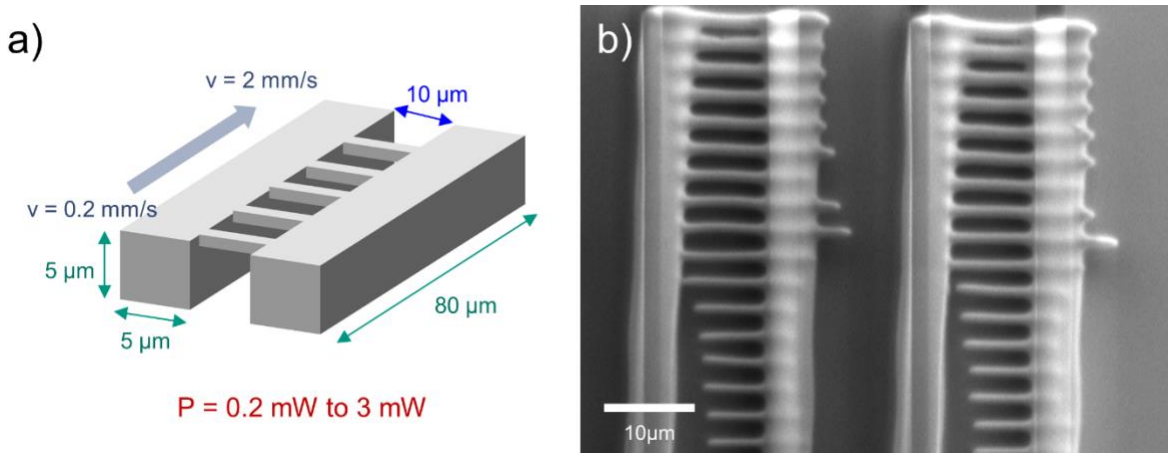


**Figure 4-9.** a) Schematic representation of the experimental process variables used to produce TPP suspended wire structures. The average power used to fabricate the structures varied from 0.2 mW to 3mW and scanning velocity spanned the range 0.2 to 2 mm/s. b) SEM micrograph (top view) of two pairs of posts, featuring the suspended wires.

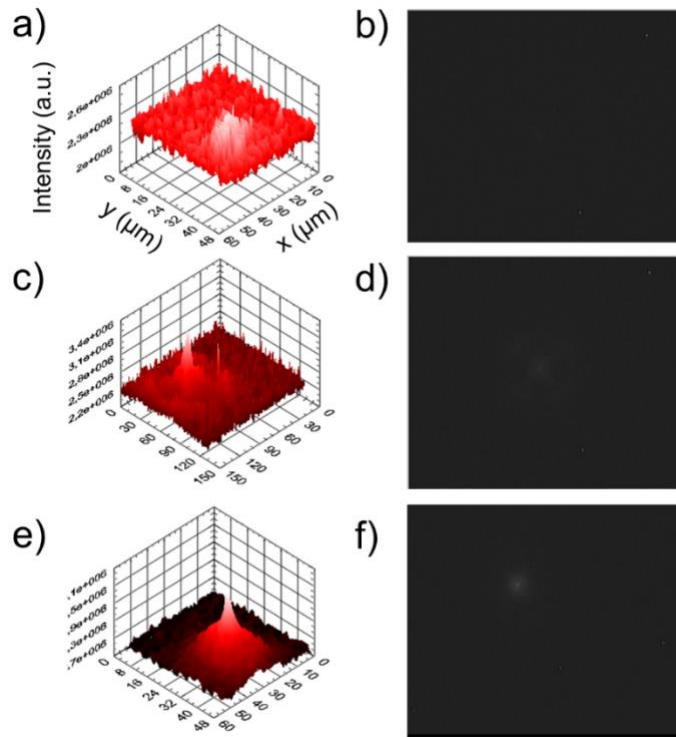


**Figure 4-10.** Interface searching procedure. (a,b) Autofluorescence intensity profile and camera image at the immersion oil phase, before descending the focus into the photoresist material. Laser power was set to 0.8mW in order to achieve autofluorescence. (c,d) An autofluorescence peak is detected, but it is still not completely resolvable from background noise. (e,f) A well-defined fluorescent intensity peak emerges when the focus spot is within the photoresist film (~1 to 2μm within the material). Adapted from ref. [142]. T. Woggon, 2011.

## 4.5 Results and discussion

### 4.5.1 SEM analysis of CNWs produced by TPP

In Figure 4-9b an SEM picture of a non-pyrolyzed TPP photoresist sample is presented. This microstructure represents a test field in which scan velocity and laser power were varied. As discussed in Section 4.3.3, linewidth resolution will be a function of these parameters. We observed that the TPP threshold for polymerization and successful patterning of the wires was  $1.13 \pm 0.12$  mW, at a scan velocity of 0.2 mm/s. Figure 4-11 shows a typical example of how the minimum dosage was determined. Furthermore, Figure 4-11 i and ii) present a zoomed image of the suspended SU-8 wire structure for  $P_t = 3.0$  mW before and after carbonization, respectively. It should be noted that at higher exposure doses, we noticed an overexposure effect towards the ends of the wires. This was a consequence of the way in which the structures were fabricated. Because the supporting structures are exposed first and then the wires, the regions near the ends were essentially exposed to twice the normal dose. This effect was accentuated for higher average powers, as seen in Figure 4-11i, with the bottom wire in the image having the maximum dose used in the experiments ( $P_t = 3.0$  mW,  $v = 0.2$  mm/s). The geometrical configuration used in this experiment prevented the collapsing of the majority of the suspended structures after pyrolysis. This problem arises particularly in the case when different photoresist are used (such as IP-Dip from the commercial set-ups) which severely limits the design freedom to few geometries.<sup>52</sup> The presented fabrication scheme allowed us to create freely suspended CNWs without any reported problem, likely due to the mechanical robustness offered by highly crosslinked SU-8 2050. Nonetheless, this precursor is known to give substantially bigger feature sizes than SU-8 2000, even for the same processing parameters.<sup>140,142</sup>

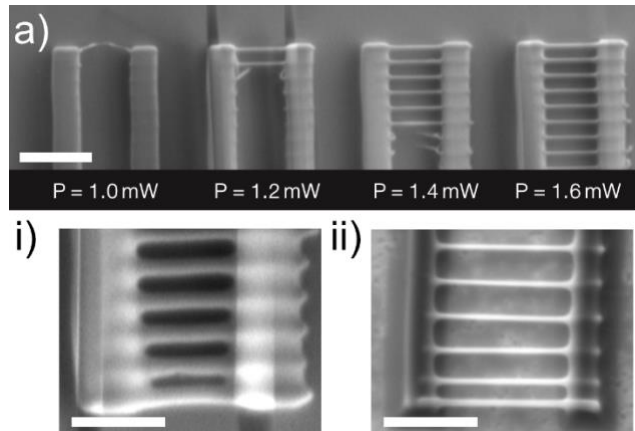


**Figure 4-11.** (a) SEM micrograph of a TPP test field, showing the dosage threshold required for fabrication of stable (non-collapsed) suspended SU-8 wires (blurred lines are due to insufficient conductivity during imaging in SEM). (i) Typical micrograph of photoresist wires before pyrolysis (fabricated with  $P = 3.0\text{mW}$ ). (ii) The photoresist wires after pyrolysis, featuring volumetric shrinkage and straightening of wires into CNWs. Scale bars are a)  $10\mu\text{m}$ , i)  $5\mu\text{m}$  and ii)  $5\mu\text{m}$ .

To continue our analysis of the geometry of the produced TPP structures, we note that the expression for TPP linewidth resolution (Eq. 4.31) can be rewritten in terms of the exposure dosage according to:

$$d_{line} = \alpha w_0 \left[ \ln \left( \frac{\sigma_2 N_0^{*2} D_{2PA,line}}{C} \right) \right]^{1/2} \quad (4.32)$$

where  $D_{2PA,line} = \frac{\nu \tau_L \sqrt{\pi} w_0}{2\nu_y} P_t^2$ ,  $N_0^* = \frac{2}{\pi w_0^2 \tau_L \nu \hbar \omega_L}$  and  $\alpha$  is a constant reflecting characteristic

of the exposure scheme, which describes the fact that diffraction limit is not the sole factor that determines voxel size.<sup>143</sup> We proceeded to plot this expression for the obtained experimental data of diameters in Figure 4-12a, using  $\sigma_2/C$  and  $\alpha$  as fitting parameters. In this plot, we present the dependence of the diameter of SU-8 wires with the TPP dose. We remark that the dosage dependence is retained even after the thermoplastic deformation induced by high temperature pyrolysis. Photoresist nanostructures subject to carbonization are known to suffer semi-isotropic shrinkage, characterized by “gum-like” distortions in one or several directions, depending on the topography of the substrate they are fixed to.<sup>49,144</sup> We theorize that the SU-8 line structures here presented suffer a marginal deformation of this

kind, as the height of the structures prior to pyrolysis is  $5\mu\text{m}$ , and this effect is known to become significant for tall structures ( $20\text{-}80\ \mu\text{m}$ , or more).<sup>44</sup> Under these assumptions, we can use the fitted curves from Figure 4-12a to estimate the diameter shrinkage percentage. In Figure 4-12b the experimentally obtained diameter shrinkage is plotted for all pyrolyzed samples ( $D_{sh}(\%) = 1 - D_f/D_i$  where  $D_i$  and  $D_f$  are the diameter before and after pyrolysis, respectively). The estimated shrinkage effect is plotted as a continuous line, which has a fair agreement with the experimental trend. We believe this is the first experimental attempt to link the predicted feature sizes after pyrolysis of TPP structures with the theory of voxel scaling.

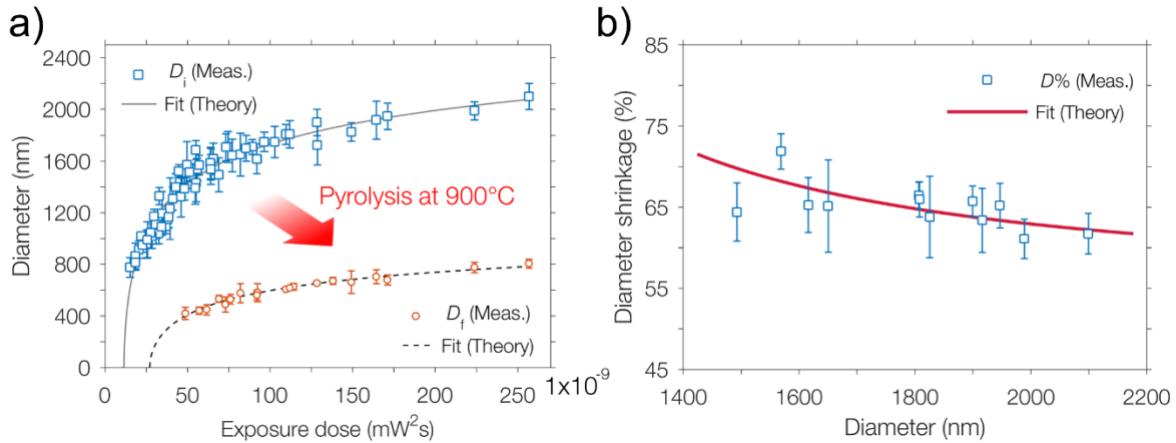


**Figure 4-12.** (a) Experimentally obtained wire diameter resulted from TPP and pyrolysis of TPP structures. (b) Percentage of diameter shrinkage in TPP structures after pyrolysis. The curve denotes a model fitting based on the theoretical voxel linewidth resolution.

The functional relationships of Figure 4-12a can be seen in SEM micrographs from Figure 4-13, where pyrolyzed CNWs produced from several experimental powers and scanning velocities are presented. These micrographs evince the voxel linewidth scaling as dosage is increased. However, for better visualization and practical application, we plot the dependence of voxel linewidth as a function of fabrication parameters in Figure 4-14. This Figure allows to determine families of curves at three different stage velocities. As expected, linewidth is reduced with increasing stage velocity.

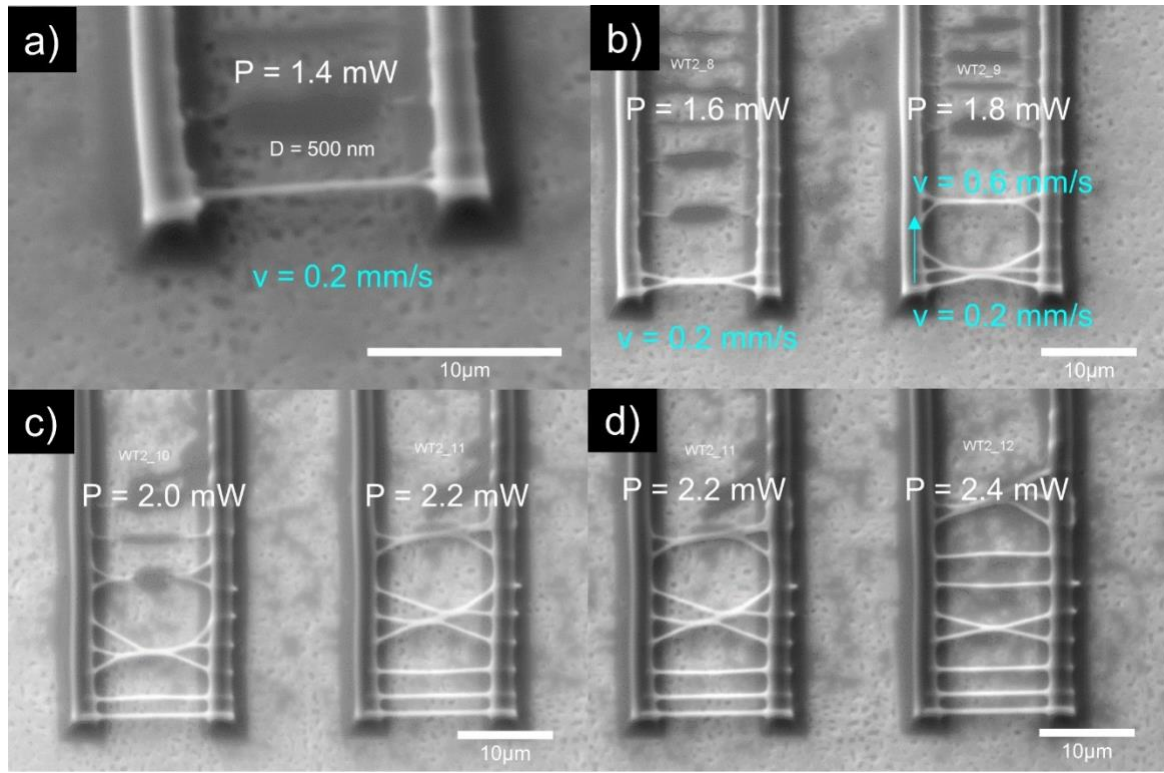


**Figure 4-13.** SEM micrographs of CNWs fabricated by pyrolysis of TPP structures. (a) Glassy carbon posts with a suspended CNW in between the structures; fabrication parameters:  $v = 0.2 \text{ mm/s}$ ,  $P = 1.4 \text{ mW}$ . (b-d) Test fields of CNWs fabricated at different average laser power and velocities (in steps of 0.1 mm/s, indicated by arrow).

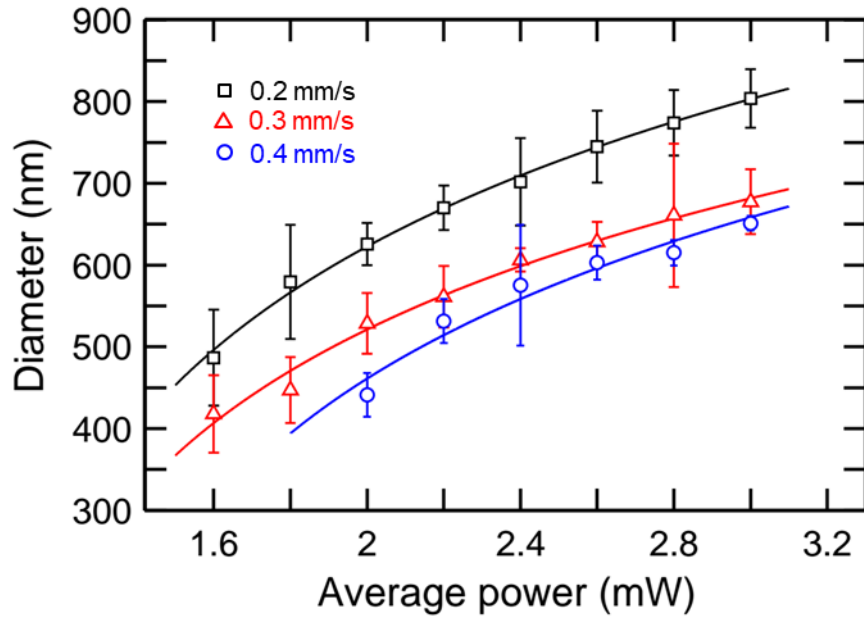


**Figure 4-14.** Dependence of the diameter (linewidth resolution) of pyrolyzed CNWs as a function of fabrication parameters (scan velocity and average power).

#### 4.6 Summary

The work presented described the theoretical aspects of a simple model for MPP of a polymeric material. It was demonstrated that there are process variables that can be divided into fabrication parameters (such as laser wavelength, repetition rate, pulse duration and average laser power) and material properties (such as the MPA cross section). Both parameters have been researched as an alternative to reduce the feature size and resolution of MPP. The theoretical derivation showed that the transition probabilities for  $N > 3$  are fundamentally low, which imply that either very high photon fluxes (often enough to optically damage the material) must be used or one must employ an efficient, chemically engineered photosensitizer with high MPA cross section.

Moreover, it was found that in the scanning configuration, the voxel lines receive a different dosage that results in smaller diameters; however, one must trade the precision of the controlled variable: in the normal exposure case, the exposure time will be controlled by the

shutter speed, while in the scanning configuration, the precision will be dependent on the movable stage.

Even though we calculated the resolution limit for a given set of fabrication parameters, the theory is imperfect in that arbitrarily small features will be predicted for a selection of parameters (for instance, one can always choose the laser power to be infinitely close to the polymerization threshold, essentially creating unrealistically small voxel sizes). In a realistic scenario, the absorption threshold is not ideally sharp, and the local inhomogeneities of the monomer/photo-initiator mixture reduce the minimum achievable resolution. Therefore, future works should improve on the presented theory by introducing stochastic model of the photo-initiation, propagation and termination processes, which could be based on the two-beam approaches and depletion theory introduced in section 4.2. While it is likely that such model would not yield analytical expressions for the voxel sizes, it would present a more complete theory which could be tackled with other computational techniques (such as finite element analysis methods).

## 5 Surface Modification of Carbon Nanostructures

Nanostructured carbons have found important application in the manufacturing next-generation biosensor and biomedical devices, owing to their unique physical and chemical properties. Biosensing in these devices requires:(i) a biological receptive element that selectively interacts with the target analyte; and (ii) a transducer element that converts the biological response into a recognition signal. A diverse range of bioactive compounds have been used in the primary element, including nucleic acids such as deoxyribonucleic acid (DNA), aptamers and peptide nucleic acid (PNA); proteins such as enzymes and antibodies; and cells, such as microorganisms, neurons, tissue, etc.<sup>145</sup> Remarkably, functionalized carbon nanomaterials have been employed as the transducing element by providing a suitable surface that translates the biological recognition process into a measurable output with high sensitivity.<sup>7,70</sup> Precise engineering of this nanomaterial-based interface is therefore of utmost importance; it performs the tasks of biomolecule attachment, via the presence of reactive functionalities at the surface, and effective transduction of the biochemical interaction between the analyte and the bioactive compound.

### 5.1 *Characteristics of the bioreceptor surface*

High performance biosensors require the correct choice of the surface at which biomolecule immobilization takes place to provide optimal sensitivity, accuracy and selectivity.<sup>146</sup> The surface chemistry and physical characteristics must be carefully designed to guarantee that proteins preserve their integrity, native conformation and biological activity.<sup>147</sup> In the following sections, the relevant physical and chemical characteristics that an effective bioreceptor surface should possess will be discussed.

### 5.1.1 Physical Characteristics

#### 5.1.1.1 Surface area

In terms of surface morphology, a bioreceptor surface should possess high surface area to maximize the chance of biomolecule interaction.<sup>148</sup> This property is routinely quantified with the specific surface area (SSA) of the material, which is defined as the surface area per unit of mass.<sup>149</sup> Adsorption and reactivity of a surface are highly dependent on SSA, making it an important parameter to consider in surface engineering.<sup>150</sup> Consequently, intensive research efforts have been focused on the engineering of materials with high SSA and surface-to-volume ratio for biosensing applications.<sup>70,145</sup>

Carbon nanomaterials have become an important alternative in biosensor design because they exhibit excellent mechanical, thermal, electrical and chemical properties, as well as high SSA.<sup>70,151</sup> These nanostructures span a wide variety of allotropes, including *one-dimensional* (1-D) structures such as single-walled carbon nanotubes (SWCNTs), multi-walled carbon nanotubes (MWCNTs),<sup>7,70</sup> carbon nanofibers (CNFs),<sup>71</sup> carbon particles,<sup>22</sup> and *two-dimensional* (2-D) graphene as well as graphene oxide.<sup>19</sup> For carbon nanotubes, Peigney et al. have reported that the theoretical SSA depends on the diameter and the number of nested walls in the structure, ranging from 50 to 1315 m<sup>2</sup>/g.<sup>152</sup> However, experimental data of the SSA of MWCNTs lies around ~10 to 500 m<sup>2</sup>/g. Remarkably, 1-D structures like SWCNTs represent the smallest dimension features that can provide efficient electron transfer and thereby are of fundamental relevance in building bioreceptor surfaces.<sup>153,154</sup>

#### 5.1.1.2 Surface topography

An object can also be characterized in terms of its surface topography, which refers to the amplitude, spacing and shape of its constituent features.<sup>155</sup> In general terms, surface topography is divided in three main components: roughness, waviness and form.<sup>155</sup> The surface roughness refers to irregularities in the surface that form its texture.<sup>155</sup> It is typically described with the average deviation from the mean height of the surface ( $R_a$ ) and the root

mean square of such deviation ( $R_q$ ).<sup>156</sup> Roughness is important in the design of biomedical materials and has been found to compromise cell adhesion.<sup>157</sup> However, greater surface roughness in the surface of biochips has also been associated with an increase in SSA accessible for biomolecular interaction.<sup>158</sup> The waviness of the structure corresponds to the variation of the surface profile where the roughness or texture is superimposed.<sup>155</sup> Finally, form is reserved for variations of the general shape of the structure, neglecting roughness and waviness.<sup>155</sup>

#### *5.1.1.3 Surface wettability*

Surface wettability also plays an important role in the adsorption of proteins and adhesion of cells to a substrate.<sup>159</sup> Remarkably, it has been found that the ultra-thinness of 2-D graphene does not significantly disrupt the wetting behavior of surfaces that exhibit wettability dominated by van der Waals forces.<sup>160</sup> Despite this behavior, SWCNTs and MWCNTs, which are essentially graphene sheets wrapped in cylindrical tubes, exhibit poor wettability (due to their hydrophobicity) and dispersibility complicating their wide application in the industry.<sup>161</sup>

### *5.1.2 Chemical characteristics*

#### *5.1.2.1 The presence of functional groups*

In a biosensor, the surface that is acting as a bioreceptor interface must have a well-defined chemical selectivity to achieve proper detection of the target biomolecule.<sup>146</sup> The overall performance of the device will be closely related to the efficiency of the protein immobilization process.<sup>162</sup> In view of this, the binding of specific and non-specific proteins should be controlled in detail by engineering of the reactive functional group present at the surface.<sup>162</sup> Some of the most common chemical functionalities that have been used for biosensor fabrication include carboxyl (-COOH), hydroxyl (-OH), amine (-NH<sub>2</sub>), carbonyl (-COOCH<sub>3</sub>), thiol (-SH), aldehyde (-CHO), phosphate (-PO<sub>4</sub><sup>3-</sup>) and silane groups.<sup>148</sup> A

schematic representation of a modified surface with carboxyl, amine and hydroxyl groups is shown in Figure 5-1.

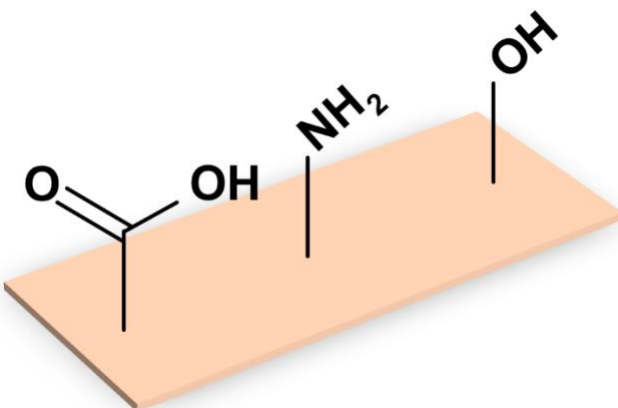


**Figure 5-1.** Examples of desirable chemical functionalities for biosensor applications, portraying carboxyl, amine and hydroxyl groups.

Unfortunately, a functionalized platform will tend to become deactivated over time due to the “aging effect”.<sup>163</sup> This phenomenon consists in the reorientation surfaces into their original state to occupy lower levels of energy, essentially losing the created reactive groups.<sup>146</sup> A sufficiently stable surface with properly formed functionalities can lessen the aging effect and improve the immobilization efficiency.<sup>162</sup> Therefore, the stability of the functionalities in a surface is a highly desired characteristic.<sup>146</sup>

To provide proper accessibility of the biomolecule’s active site in the biosensor, optimal the concentration and distribution of the chemical functionalities in the surface must be carefully controlled.<sup>162</sup> Figure 5-2 shows a schematic representation of different concentrations of functionalities and their effect on the activity of a biosensor device. As shown in Figure 5-2a, the presence of few reactive sites leaves proteins prone to entering in direct contact with the inert surface, which could induce hydrophobic denaturation of the compound.<sup>146</sup> On the other hand, an overly crowded surface with chemical functionalities (Figure 5-2b) might result in the steric repulsion of incoming biomolecules, which would hinder the overall performance of the platform.<sup>146</sup> Therefore, an optimal bioreceptor should have evenly distributed functionalities (Figure 5-2c) that allow control over the number of protein binding sites and subsequently provide efficient biomolecular immobilization.<sup>146</sup>

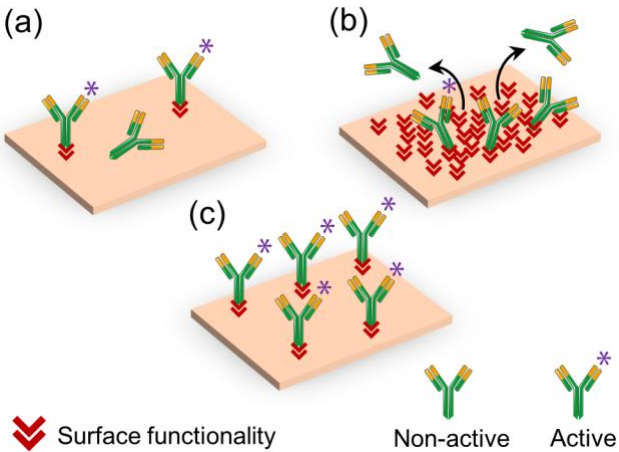


**Figure 5-2.** Effect of the distribution of functionalities on the bioactivity of the bioreceptor interface. (a) Few functionalities result in activity loss when antibodies directly encounter the substrate. (b) Crowded functionalities in the surface induce steric repulsion that prevents possible antibodies from meeting their respective bonding sites, resulting in activity loss. (c) Evenly-spaced functionalities yields an optimal configuration of active antibodies in the bioreceptor interface.

Even though reactive functional groups are greatly needed for fabrication of biosensing platforms, they are non-existent in pristine carbon nanomaterials, as carbon graphene-like surfaces possess an inert nature.<sup>31</sup> In view of the above, two generalized methods have been used to couple biomolecules and carbon nanomaterials involving covalent and noncovalent strategies of immobilization.<sup>145</sup> In general, modification of the carbon surface is required to induce reactive groups that can non-covalently or covalently (via varied types of linkers) bind to the biomolecule.<sup>145</sup> Possibly the most commonly utilized technique for covalent immobilization of proteins is by diimide-activated amidation of carboxylic acid-ended carbon nanomaterials.<sup>153</sup> This reaction involves the use of carbodiimide compounds, such as water-soluble 1-Ethyl-3-(3-dimethylaminopropyl) hydrochloride (EDC) that initiate the crosslinking to carboxylic acids (

Figure 5-3).<sup>164</sup> To increase the efficiency of the reaction, *N*-hydroxysuccinimide (NHS) or its water-soluble analog sulfo-NHS are typically associated in the conversion of the carboxyl groups to the active and unstable functional NHS-ester groups. This functional group readily forms dry-stable conjugates with amine groups, as opposed to the o-Acylisourea active esters formed in the EDC crosslinking reaction.<sup>164</sup>

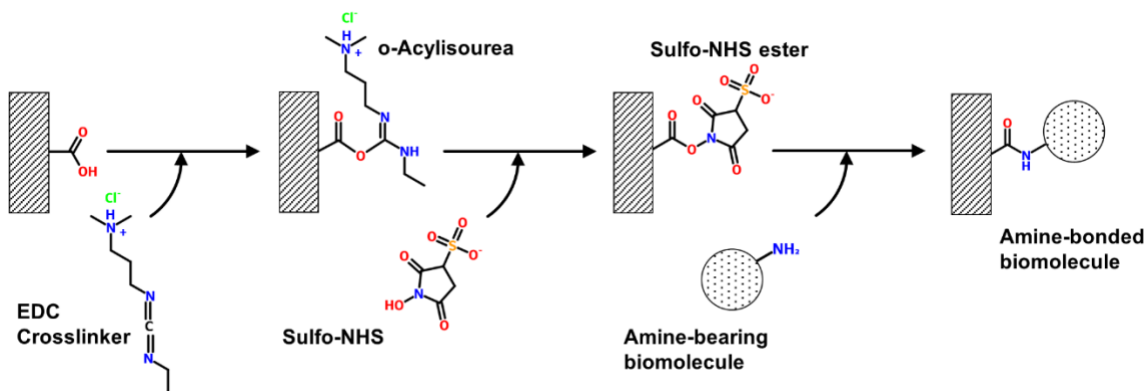


**Figure 5-3.** EDC/Sulfo-NHS protocol for the immobilization of biomolecules with amine termini on a surface containing carboxylic acid functionalities.

The EDC/NHS (or EDC/sulfo-NHS) protocol can be complemented with diamine organic spacers between the surface and the biomolecule. This separation results in a higher spatial freedom of the functionalities, allowing for further protein attachment events to occur.<sup>158</sup> Some of these amine-containing molecules include polyethyleimine (PEI), hexamethylenediamine (HMDA) and 1,2-diaminopropane (DAP).<sup>165</sup> Subsequently, a secondary reaction can be used to conjugate the amine-termini of the spacers to the biomolecules, for instance through an amine-reactive cross-linker such as glutaraldehyde (GA), typically used in biochemistry experiments.<sup>158,164</sup>

## 5.2 Biomolecular interactions

Non-covalent immobilization of a biomolecule requires the existence of driving forces resulting from the interaction between the protein and the functionalized surface. Depending on the atoms, molecular moieties or bonds present in the interaction, these forces will vary in strength and stability.<sup>166</sup> Forces involving electric charges give rise to ionic bonding, in which a negatively charged atom (anion) is attracted to a positively charged atom (cation). Alternatively, like charges will experience a repulsive force. At an adjusted pH, proteins form charged moieties that readily interact with other charged molecules (Figure 5-4a). A change in pH can therefore result in the change of the net charge of the molecules, thus altering the electrostatic interaction.<sup>167</sup>

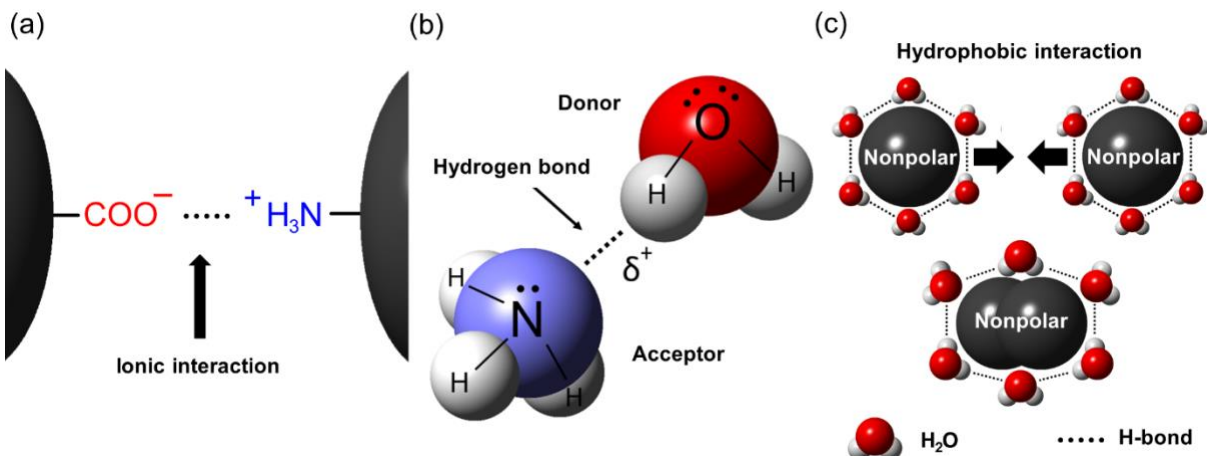


**Figure 5-4.** Physical attraction methods present in biomolecule immobilization. (a) Ionic interaction between a negatively charged carboxyl and a positively charged amino group of a protein structure. (b) Hydrogen bonding between a water molecule and an ammonia molecule. (c) Hydrophobic interaction between two nonpolar substances present in an aqueous solution.

Hydrogen bonding (hereafter H-bonding, or H-bond) is central to biosensing as it is responsible for the structure, function and dynamics in numerous chemical and biological systems.<sup>168</sup> It involves the noncovalent electrostatic interaction force between two dipoles, one of which contains a hydrogen polar bond. This polar bond is of the form X-H, where X is a highly electronegative atom such as fluorine (F), oxygen (O) or nitrogen (N).<sup>169</sup> Two groups are formed because of such bonding, namely the donor and the acceptor molecules.<sup>166</sup> The H-bond donor group is the one that results from the X-H polar compound. The high electronegativity of the donor molecule drives the electron cloud away from the nucleus of the H atom, leaving a positive partial charge ( $\delta^+$ ).<sup>166</sup> The H-bonding is then formed when this positive partial charge attracts a pair of unshared valence electrons present in another molecule (the H-bond acceptor group). This interaction is exemplified in Figure 5-4b, where a H-bond has been formed between the donor molecule ( $\text{H}_2\text{O}$ ) and the acceptor molecule ( $\text{NH}_3$ ). Compared to the ionic interaction, the effect of H-bonding is significantly stronger in protein immobilization.<sup>170</sup>

The hydrophobic effect is another kind of interaction that describes how nonpolar substances interact with polar covalent substances like water. In this case, because nonpolar compounds have an even distribution of charge, they interact poorly with water, and thus are

unable to form H-bonds.<sup>171</sup> This results in the entrapment of the nonpolar substances by the surrounding polar molecules.<sup>171</sup> Figure 5-4c (top) shows how two nonpolar solute compounds are encaged by water molecules. Nonetheless, configuration in Figure 5-4c (top) is less energetically favorable than the one in Figure 5-4c (bottom), as more water molecules are needed to contain the two nonpolar bodies. Therefore, the spontaneous aggregation of nonpolar substances into clusters tends to be favored, as it results in less exposed surface area to be covered by fixed polar molecules (increasing the entropy of the system).<sup>171</sup>

### 5.3 *Frequently used functionalization techniques*

Wet chemical treatment of surfaces is one of the most common functionalization techniques available due to its simplicity and straightforward application.<sup>146</sup> It consists in exposing the area of an inert surface interface to a liquid mixture of reagents for a defined amount of time, depending on the robustness of the substrate. For instance, carbon nanomaterials are chemically stable and hence, strong acids like sulfuric ( $H_2O_4$ ) and nitric acid ( $HNO_3$ ) have to be used to oxidize their surface and induce carboxylic groups.<sup>31</sup> This treatment is necessary, as it is known that nanocarbon materials such as single and multi-walled carbon nanotubes (SWCNT, MWCNT) require chemical modification to improve their wettability and facilitate their dispersion and manipulation.<sup>161</sup> As a result, wet chemical has allowed the straightforward integration of carbon nanomaterials into a variety of biosensing devices.<sup>22,29,172–177</sup> The reader can refer to extensive review papers that have been written on the covalent modification of carbon nanomaterials.<sup>31</sup> Nonetheless, the ease of implementation of this technique is overshadowed by its numerous disadvantages, the main one being its non-specific nature, which leads to the production of unevenly distributed functional groups in the surface.<sup>148</sup> In SWCNTs, for example, the ends of the cylindrical structure tend to be more easily functionalized due to the instability created by the fullerene-like hemispheres, as opposed to the sidewalls.<sup>31</sup> Evidently, wet chemistry of nanotubes is ineffective, since it creates randomly distributed functionalities depending on the robustness of the structure.<sup>31</sup>

Plasma-based functionalization is a widely used technique for the modification and engineering of organic polymer, ceramic and metallic surfaces without the alteration of the bulk material.<sup>178,179</sup> Plasma treatment operates in two different fashions: (i) partially ionized gas, often referred to as “low-temperature plasma” and (ii) highly ionized gas that is known as “hot plasma”.<sup>180</sup> Such plasma is typically produced by electric glow discharge and contains chemically active species that can lead to chemical reactions at the surface of the treated substrate.<sup>180</sup> In carbon modification, plasma is used to treat the structure of pristine graphitic plane structures (usually non-reactive) to induce carboxylic groups.<sup>181–183</sup>

The use of Ultra-Violet (UV) light to assist the surface modification of substrates has been extensively employed in biosensor preparation, particularly in the case of polymer materials.<sup>148</sup> By varying the wavelength of the light-source, the abortion coefficient of the material can be explored to change the depth of surface reactivity.<sup>148</sup> UV-treatment works similarly to other ionizing radiation sources such as plasma and therefore, it can initiate photochemical reactions, polymerization of monomers, free radical creation, cross-linking and graft-copolymerization.<sup>180</sup> It has mainly been employed in azide photochemistry to initiate solid-state reactions on the sidewalls of CNTs.<sup>184</sup>

Another frequently used technique for the modification of carbon surfaces involves the use of non-covalent interactions, such as  $\pi$ - $\pi$  stacking. This kind of force is based on the attraction between different aromatic species.<sup>185</sup>  $\pi$ - $\pi$  stacking mainly relies on the charge distribution and orientation of the aromatic rings.<sup>185</sup> It is known that the  $\pi$  electron density present in the aromatic structure introduces a quadrupole moment with partial negativity on the top and bottom of the ring, while creating a partial positive charge around its periphery.<sup>185</sup> This technique has been initially studied by Hunter and Sanders early as 1990.<sup>185</sup> Hunter and Sanders established qualitative conditions for the anticipation of the aromatic rings in interaction as we now know as  $\pi$ - $\pi$  stacking.<sup>185</sup> Some of the first experimental studies on  $\pi$ - $\pi$  stacking in nanocarbons involved the coating of SWCNTs with biomolecules such as single stranded DNA (ssDNA).<sup>186</sup> Based on this technique, other researchers have successfully functionalized carbon nanomaterials of different categories<sup>12,23,24,26,187–189</sup>

#### *5.4 Advantages and disadvantages of current functionalization techniques*

One of the main advantages of the wet chemistry methods is that they require no specialized equipment to perform the treatment and thus, can be readily implemented in most laboratories. Evidently, these methods offer a simple route to explore surface modification of carbon nanomaterials and other substrates, from an academic perspective.<sup>148</sup> Despite the ease of implementation offered by wet chemistry methods, they are not well suited for regio-specific functionalization because the complete wet surface of the nanomaterial is etched. Consequently, a variety of unevenly arranged oxygen groups are produced on the treated surface.<sup>148</sup> Furthermore, the degree of functionalization may not be repeatable. There is limited information in the literature about the shelf-life of the generated functionalities to properly assess the effectiveness of such techniques. In addition, it is well known that covalent modification alters some of the desired properties of nanomaterials.<sup>31</sup> Finally, the major disadvantage of this method is that it produces hazardous waste chemicals hence making it not an environmental friendly technique for mass manufacturing of the biosensor devices.<sup>148</sup>

Contrary to wet chemistry methods, plasma treatment of carbon nanomaterials has proven to be a superior functionalization technique since it does not produce any contaminant by-products.<sup>179,181,182</sup> Nonetheless, such methods typically require continuous vacuum to control the operation of plasma application, which makes the overall process costly for industrial applicability. In addition, the reproducibility of the obtained functional groups at the surface can be an issue, as the overall exposed surface is attacked by the effect of the plasma radiation.<sup>148</sup> Furthermore, the shelf-life of the functional groups produced is not guaranteed, giving this method serious disadvantages for realistic application outside the research environment.<sup>148</sup> Finally, plasma modification techniques have the critical disadvantage of leaving the surface highly susceptible to deleterious aging effects.<sup>163</sup>

An advantageous feature in light-source dependent techniques like UV treatment is that the change in wavelength can be explored as an experimental parameter to modify the depth of surface reactivity, which is highly desirable in functionalization.<sup>148</sup> Additionally, UV-

treatment can usually be performed to carry out photochemistry in a solid-state reaction, reducing the number of chemicals involved, thereby simplifying experiments and handling of pollutants. However, UV techniques can be affected by the optical properties of the treated material, affecting the consistency of functionalization results.<sup>148</sup> Furthermore, the type and concentration of the functionalities produced by this method are difficult to control.<sup>148</sup>

In wet-chemical, plasma and UV treatments, the pristine bonding configuration of the nanostructured carbon must be modified to induce the active functionalities. On the other hand, non-covalent modification strategies such as  $\pi$ - $\pi$  stacking interactions, are more promising in terms of structure preservation, since no bonds of the original structure have to be broken.<sup>12</sup> In a covalent modification scheme, either the biomolecule, the nanomaterial or both structures loose some of their pristine configuration activity and properties.<sup>190</sup> Nonetheless,  $\pi$ - $\pi$  stacking interactions have weaker bonding energies in general and are highly dependent on the orientation of the ring structures.<sup>185</sup>

Evidently, the engineering of highly efficient and evenly distributed functional groups on carbon surfaces requires alternative functionalization techniques. Not only should these techniques allow for control over the distribution of the groups, but also, they should minimize the modification of the desirable properties of the nanostructure (SWCNTs, MWCNTs, graphene, nanowires), which are greatly sought for biosensing applications. Finally, it is of equal importance that such surface modification methods provide stable functionalities that are less susceptible to aging effects.

### 5.5 *Functionalization of carbon nanomaterials*

Table 5-1 describes in detail some of the most important functionalization techniques which have been performed on carbon nanomaterials. In this Table, type of the carbon nanomaterials, functionalization reagents, employed functionalization technique and type of interaction between the surface and functionalization reagent are specified. Table. 1 also covers the functionality outcomes, the target biomolecules and the interaction types with the

biomolecular entities of interest. Moreover, the table outlines some of the major advantages and disadvantageous of the applied technique in a brief manner.

**Table 5-1.** Comparison study on different functionalization reagents and techniques employed to immobilize target biomolecules on the surface of different carbon nanomaterials, such as SWCNTs, MWCNTs, graphene, CNFs and carbon particles.

Treated surface	Functionalization reagent	Functionalization technique	Surface-reagent interaction	Functionalization outcome	Intermediate interaction	Interaction with biomolecule	Target biomolecule	Advantages and Disadvantages	References
SWCNT	H <sub>2</sub> O <sub>4</sub> , HNO <sub>3</sub> and polyelectrolyte layer	Wet chemistry (acid treatment)	Chemical (covalent)	Carboxyl groups, aldehyde groups, carbonyl groups and hydroxyl groups	Different polyelectrolyte layers were stacked with SWCNTs and Silicon nanoparticles. The outermost polymer layer interacts with the target biomolecule.	Chemical / Electrostatic interaction	Acetylcholinesterase (applied for detection of Acetylcholine)	Advantage: Ease of implementation Disadvantage: Use of strong corrosion reagents hinders large-throughput; associated with high pollution. Poor functional group specificity	172
	H <sub>2</sub> O <sub>4</sub> and HNO <sub>3</sub>	Wet chemistry (acid treatment)	Chemical (covalent)	Carboxyl groups	PEG coating (physical), followed by (EDC-NHS) to create amide bonding	Amide bond (covalent)	DNA	Advantage: Regio-specific, well oriented functional groups Disadvantages: Complex and expensive technique, not suitable large scale production	173,174
	4-amino-benzoic acid (ABA)	Electropolymerization (non-covalent)	Physical (ABA has carboxyl groups)	Carboxyl groups	DNA (amino functionalized) is covalently coupled to the carboxyl groups through amide formation after activation with carbodiimide	Chemical (covalent)	DNA	Advantage: Site-specific functionalization and minimized nonspecific binding of biomolecule on the surface. Disadvantage: Multiple steps and complex techniques are involved in the functionalization process.	25
MWCNTs	Argon plasma	Plasma treatment	-	Carbonyl and amino groups	(i) Maleic anhydride modification through plasma reaction. (ii) Epoxy nanocomposites were added via amidation reaction	-	-	Advantages: Non-polluting, scalable technique. Disadvantages: Complex technique, requires vacuum. Shelf-life of the functional groups is not guaranteed.	182
	Oxygen, nitrogen and argon plasma radiation	Plasma treatment	-	Carboxyl groups	-	Common interactions between existing functional groups on the surface of the cells and carboxyl groups	Primary humanoid fibroblast cells	Advantage: No chemical waste is generated Disadvantage: Requires vacuum and reproducibility could be a problem. Shelf-life of the functional groups is not guaranteed	181
	Azidothymidine (AZT)	UV treatment (azide-photochemistry)	Chemical (covalent)	Hydroxyl groups	Hydroxyl group reacts with phosphoramidite mononucleotide to synthesize DNA	Chemical (covalent)	ss-DNA	Advantage: Solid state reaction prevents the use of wet chemicals Disadvantage: Multiple complex steps are needed to attach the target biomolecule	184
	Azido compounds	Nitrene chemistry	Chemical (covalent)	Hydroxyl, amine, carboxyl, and bromide groups	-	-	-	Advantage: Low cost, green technology Disadvantage: Control of distribution of functionalities is not possible	161

	Azo-initiators (azonitriles, azoamides, azoamidines)	Free radical addition	Chemical (covalent)	Hydroxyl, amidine, carboxyl groups	-	-	-	Advantage: Green, simple and tunable functionalization method	191
								Disadvantage: Covalent modification weakens the surface electrical and thermal properties	
Graphene	H <sub>2</sub> O <sub>4</sub> , HNO <sub>3</sub> and chitosan solution	Wet chemistry (acid treatment)	Absorption (of glucose oxidase)	Carboxyl groups	Dispersion in chitosan solution and addition of glucose oxidase	Absorption	Glucose oxidase (used to detect glucose)	Advantage: Chitosan provides a biocompatible microenvironment for biomolecule immobilization	175
	Sodium nitrate (NaNO <sub>3</sub> ) and H <sub>2</sub> O <sub>4</sub>	Wet chemistry (acid treatment)	Chemical (covalent)	Carboxyl groups, hydroxyl groups and epoxides	Carbodiimide-assisted amidation reaction	Chemical (covalent)	Antibodies (Rotavirus)	Disadvantage: Use strong corrosion reagents hinders large-throughput; associated with high pollution. Poor functional group specificity	176,177
	(i) H <sub>2</sub> O <sub>4</sub> and phosphoric acid (H <sub>3</sub> PO <sub>4</sub> ). (ii) Potassium hydroxide (KCl) and chloroacetic acid (MCA)	Wet chemistry (acid treatment)	Chemical (covalent)	Initial functional groups: carboxyl groups. Secondary functional groups: amine, aldehyde, isocyanide groups.	Ugi four component reaction on carboxylated graphene oxide	Chemical (covalent)	Bacillus thermocatenulatus lipase	Advantage: Novel multifunctionalization of graphene oxide achieved in mild one pot reaction	29
	Oxygen plasma	Plasma treatment and UV treatment	Physical	Carboxyl groups	Anti-ErbB2 molecules are covalently coupled to the carboxyl groups through amide formation after activation with carbodiimide	Specific antigen- antibody interaction	ErbB2 gen	Advantage: Selective and stable immunosensor.  Disadvantage: Oxygen plasma treatment and wet chemistry steps could yield non-uniform distribution of functionalities. Complex fabrication steps	183
Carbon Nanofibers	Polylactide-co- glycolide	Polymer blending of graphene powder	Physical mixing of reagents	Hydroxyl groups	-	Common interactions between existing functional groups on the surface of the cells and hydroxyl groups	Mesenchymal stem cells	Advantages: Ease of fabrication, biocompatibility, exhibits neurogenical activity, mechanical flexibility.  Disadvantages: No control over nanostructured surface properties of graphene.	192
	Oxygen plasma	Ultraviolet Ozone (UVO) and oxygen plasma treatment	Physical	Hydroxyl, carbonyl, carboxyl and phenolic groups	-	Common interactions between existing functional groups	Neuroblastoma (N2a) and rat Schwann cells	Advantage: Use of UV/plasma treatment does not produce chemical waste.	72,193

					on the surface of the cells and hydroxyl groups		Disadvantage: Shelf-life of the functional groups is not guaranteed	
Carbon Particles	$H_2O_4$ and $HNO_3$	Wet chemistry (acid treatment)	Chemical (covalent)	Carboxyl groups	The surface of the carbon particles was modified with poly ethylene glycol-bis-amine. The free amino groups impaired by these molecules were used to bind IgG antibodies	Chemical (covalent)	IgG antigen	Advantage: Functionalities resist harsh conditions (thermo stable, tolerates wide pH and stable in various solvents).
								Disadvantage: Use of strong corrosion reagents hinders large-throughput; associated with high pollution. Poor functional group specificity

### 5.5.1 Common functionalization techniques for carbon nanomaterials

#### 5.5.1.1 Wet chemical treatment

In wet chemical functionalization techniques, a liquid reagent is used to chemically etch the material of interest, typically resulting in non-specific, randomly oriented oxygen-containing reactive groups.<sup>148</sup> To alleviate this regio-specificity problem, Weizmann and colleagues incubated SWCNTs in an aqueous solution of Triton X-100/poly(ethylene glycol) (PEG) after treating the structures with a concentrated sulfuric and hydrogen peroxide mixture (4:1, 98% and 30%, respectively, 30 min).<sup>173</sup> Through this process, nanotubes are wrapped with a polymer layer that prevents unwanted functionalization and nonspecific absorption (Figure 5-5a), while leaving the oxidized termini available for selective coupling with DNA strands using EDC/NHS chemistry (Figure 5-5b). Afterwards, the authors the created SWCNT network linked by oligonucleotides to hybridize with complementary DNA strands attached to gold nanoparticles (AuNP) (Figure 5-5c). Nonetheless, by changing the addressed particle to other biomolecule of interest, a variety of highly regio-specific biosensing devices can be envisioned (Figure 5-6).<sup>174</sup>

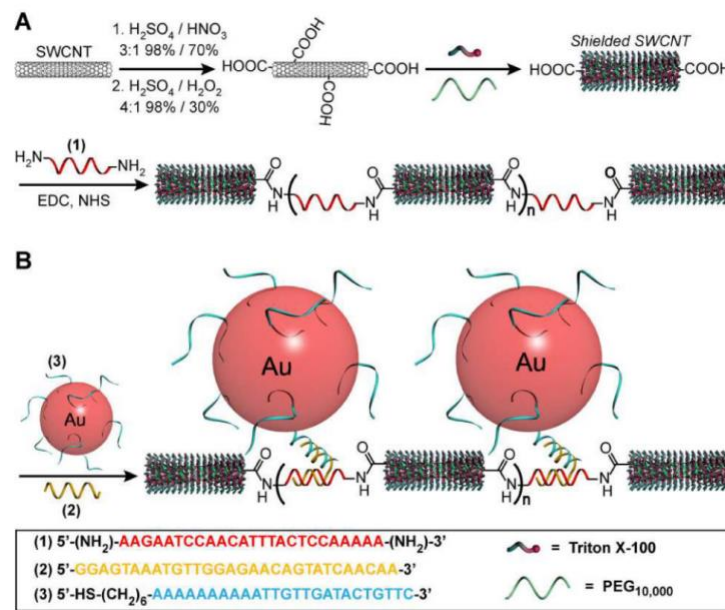


**Figure 5-5.** A) SWCNT functionalization scheme by acid treatment, followed by shielding and nanotube-DNA conjugation. B) Hybridization of DNA-SWCNT and AuNP probing. Reprinted from ref. [35], Y. Weizmann *et al.*, *J. Am. Chem. Soc.*, **132**, 2010, 14009.

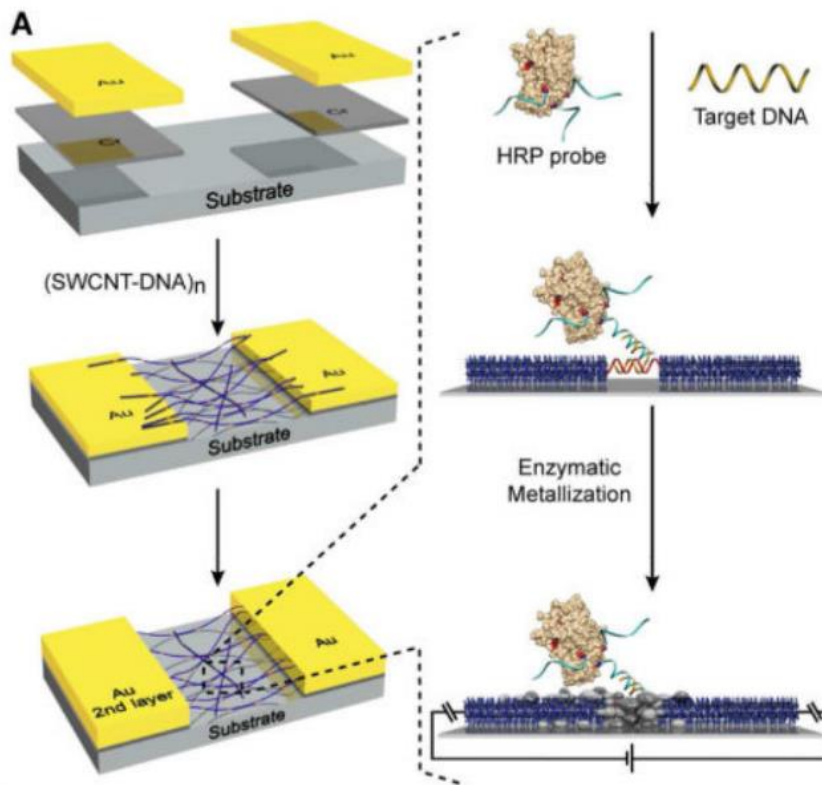


**Figure 5-6.** Proof of concept of a SWCNT-based sensor for the detection of horse radish peroxidase (HRP). The prepared SWCNT network is used to bridge the two metallic contacts. Only the specific regions connecting the tubes are functionalized to interact with the target biomolecule. Reprinted from ref. [36] Y. Weizmann *et al.*, *J. Am. Chem. Soc.*, **133**, 2011, 3238.

Xue Wei et al. used an acid treatment ( $\text{H}_2\text{O}_4$  and  $\text{HNO}_3$ ) in order to increase the solubility of SWCNTs and easily stack them in a layer-by-layer polyelectrolyte/silicon nanoparticle matrix.<sup>172</sup> By having a charged polymer sit at the outermost layer of the stacked structure, acetylcholinesterase was immobilized by means of an electrostatic interaction. This self-assembled thin film was used to build a cost-effective biosensor transistor that detected the presence of acetylcholine with sensitivity, resolution and response time of  $378.2 \mu\text{A}/\text{decade}$ ,  $10\text{nM}$ , and  $15\text{s}$ , respectively.<sup>172</sup> Acid treatment has also been widely used to induce carboxylic functionalities in graphene nanomaterials.<sup>177</sup> For instance, Jung et al. used this simple technique to prepare graphene oxide with carboxyl groups which reacted with the amine moieties present in rotavirus antibodies through carbodiimide-assisted amidation (Figure 5-7).<sup>176</sup>

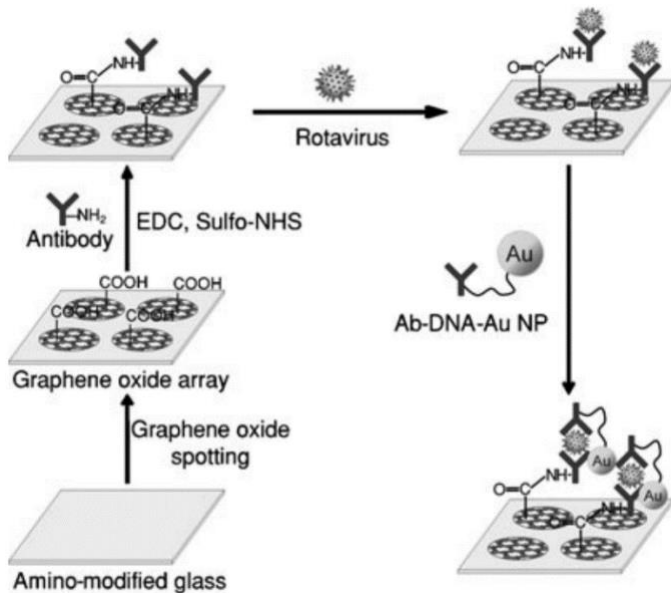


**Figure 5-7.** Functionalization scheme for the fabrication of Graphene Oxide (GO) immuno-sensors. GO is produced by acid treatment ( $\text{NaNO}_3 / \text{H}_2\text{O}_4$ ) of graphene sheets, producing carboxylic functionalities which in turn are bonded to amino groups present in antibodies through EDC/sulfo-NHS chemistry. After rotavirus immobilization, a complementary antibody bonded with a DNA-Au NP probe is used to mark the virus to effectuate the detection. Reprinted from ref. [38] J.H Jung, et al., *Angew. Chem. In. Ed. Engl.*, **49**, 2010, 5708.

The immobilized rotavirus cell was captured through the specific antigen-antibody interaction.<sup>176</sup> By linking an antibody marked with a gold nanoparticle to the other end of the antigen, researchers observed the fluorescence quenching of graphene oxide and the nanoparticles through fluorescence resonance energy transfer (FRET) between them, which served as a highly sensitive and selective detection principle.<sup>176</sup> In another study, the same radical groups were induced by acid treatment with  $\text{H}_2\text{O}_4$ ,  $\text{HNO}_3$  and  $\text{KCl}$ , which were employed to enhance the biocompatibility between graphene and chitosan polymer.<sup>175</sup> Due to the created biocompatible microenvironment, glucose oxidase can be immobilized on the surface, allowing the sensitive detection of glucose through direct electrochemistry. X. Kang and coworkers reported a much higher enzyme loading ( $1.12 \times 10^{-9} \text{ mol/cm}^2$ ) as compared with the bare glassy carbon electrode experiments, with a detection limit of 0.02 mM and a sensitivity of  $37.93 \text{ uA mM}^{-1} \text{ cm}^{-2}$ .<sup>175</sup>

### 5.5.1.2 *Plasma-assisted treatment*

Plasma assisted functionalization of carbon nanomaterials has been explored as a way of modifying the surface while preventing the detrimental damage to the structure inherent in other methods.<sup>179</sup> Vohrer et al. reported the use of glow discharge plasma to generate functional groups such as alcohol and carboxylic groups on SWCNTs, MWCNTs and carbon nanotube powder to improve their wettability using different plasma precursors (oxygen, nitrogen and argon).<sup>178</sup> Authors found that longer exposure times resulted in higher oxygen contents for both SWCNTs and MWCNTs, and reported a small, but constant, decrease in oxygen over the course of 14 days.<sup>178</sup> The improved hydrophilicity was assessed by humanoid fibroblast cell adhesion and proliferation tests on carbon nanotube sheets (bucky paper), which demonstrated the possibility of biomedical applications.<sup>178</sup>

Grafting polymerization of Maleic Acid (MA) has been achieved after argon-plasma functionalization of mwCNTs.<sup>182</sup> This procedure promoted the disentanglement and dispersion of the carbon nanostructures and provided the surface with carboxylic and amine groups. Importantly, the nanotubes retain their original length after the plasma modification, as opposed to the case of chemical acid treatments.<sup>182</sup> Further, the use of argon plasma constitutes a nonpolluting approach that is more suitable for large throughput production of functional MWCNTs.<sup>182</sup> The use of X-ray photoelectron spectroscopy detailed the chemical modification of the surface, which indicated the presence of carboxyl groups from the MA.<sup>182</sup>

Other nanostructures, such as 2D graphene has also been functionalized by plasma treatment.<sup>183,193</sup> For example, in a study by Md. Azahar et al., oxygen plasma in combination with ultra violet light exposure was used to induce carboxyl functionalities in the multilayer structure present in graphene foam (GF).<sup>183</sup> The process was then followed by EDC-NHS chemistry to covalently couple anti receptor tyrosine-protein kinase (ErbB2) molecules through amide formation.<sup>183</sup> Using a microfluidic immune-biochip ensemble, the antigen ErbB2 was detected with great selectivity at a minimal concentration of 1.0 fM. Further, the sensor utilized differential pulse voltammetry and electrochemical impedance spectroscopy to quantify the biomarkers.<sup>183</sup> These tests showed sensitivities of  $0.585 \mu\text{A}\mu\text{M}^{-1}\text{cm}^{-2}$  and  $43.7 \text{k}\Omega\mu\text{M}^{-1}\text{cm}^{-2}$  in a concentration range of the biomarker of 1.0 fM to 0.1  $\mu\text{M}$ , and 0.1 pM to

$0.1 \mu\text{M}$ , respectively.<sup>183</sup> In Figure 5-8 (top), the functionalization scheme is shown, beginning with the pristine GF structure, a scanning electron microscopy (SEM) image of the sample after plasma and UV treatment and the final antibody (ErbB2) attachment, which leads to the complete bioreceptor device.

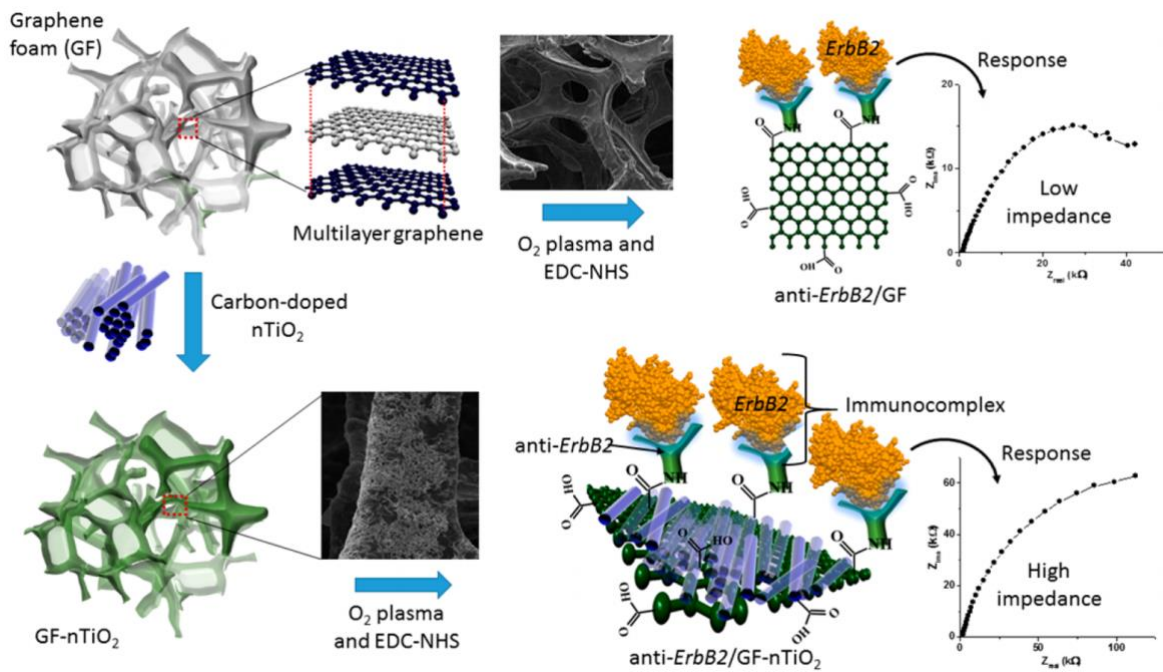


**Figure 5-8.** Oxygen plasma treatment scheme for the carboxylation graphene foam nanostructures. After the creation of carboxylic groups at their surface, multilayer sheets of graphene are treated with EDC/NHS chemistry to bind them with anti-ErbB2 antibodies. Alternatively, the foam structure can be doped with titanium dioxide ( $\text{TiO}_2$ ) nanotubes, increasing the overall impedance of the biosensor complex. Reprinted from ref. [46] M. A. Ali *et al.*, *ACS Appl. Mater. Interfaces*, **8**, 2016, 20570.

### 5.5.1.3 UV treatment

UV treatment is a functionalization technique that is used to increase the energy level at the surface, producing active sites that can react upon exposure with a substance.<sup>148</sup> In an experiment carried out by Moghaddam and colleagues, UV light has been used to initiate the etching of MWCNTs by photo-reaction of azidothymidine (AZT).<sup>184</sup> The MWCNTs were coated with a solution of AZT, which after UV irradiation created photoadducts, each with a hydroxyl group. This functionality was used to react with a phosphoramidite mononucleotide to begin synthesis of a DNA molecule, thus producing DNA coated nanotubes.<sup>184</sup>

UV treatment has also been used in combination with oxygen plasma to induce hydroxyl, carbonyl, carboxyl and phenolic groups on the surface of carbon nanofiber structures.<sup>72</sup> This hybrid modification was used to increase the wettability and biocompatibility of SU-8 and polyacrylonitrile-derived carbon fibers.<sup>193</sup> Such nanofibers have been used in the cytocompatibility assessment experiments with mouse neuroblastoma (N2a) and rat Schwann cells, suggesting that amorphous carbon nanofibrous scaffolds with favorable functionality are suitable for adhesion and proliferation of neuronal cells.

#### 5.5.1.4 $\pi$ - $\pi$ stacking

The  $\pi$ - $\pi$  stacking interaction is a relevant technique in the noncovalent surface modification of carbon allotropes such as SWCNTs<sup>13</sup> and graphene.<sup>19</sup> Using this method, Staii and colleagues reported the absorption of single stranded DNA oligomers on the surface of SWCNTs.<sup>23</sup> They described the interaction as a  $\pi$ - $\pi$  stacking between the aromatic groups present at sidewalls of the SWCNTs and the ring structure present in the bioengineered DNA sequence.<sup>23</sup> By engineering the specific sequence as the chemical recognition component in the biosensor, authors demonstrated the detection of dimethyl methylphosphonate (DMMP), 2,4-dinitrotoluene (DNT), methanol, trimethoxyamines (TMA) and propionic acid.<sup>23,188</sup> Similarly, Kim et al. demonstrated the physical functionalization of SWCNTs with human taste receptors 2, member-38 (hTASR38), to create a transistor structure, using conventional microfabrication facilities.<sup>194</sup> The device exhibited high sensitivity and human tongue-like selectivity. The same procedure had been used by this research team to produce a biosensor that mimicked the human olfactory process by immobilization of human olfactory receptor 2AG1 (hOR2AG1).<sup>195</sup> Authors claimed that such system is useful for overcoming the selectivity problems found in chemical sensors, as the receptors portrait ultrahigh specific selectivity and the nanomaterial selection provided the high sensitivity.<sup>194</sup>

There are other techniques that also involve the noncovalent interaction of a linking molecule between the nanostructured surface and the biomolecule of interest. For example, 1-pyrenebutanoic acid succinimidyl ester has been used as a crosslinker, which physically interacts with SWCNTs  $\pi$ - $\pi$  stacking means and covalently binds to the biomolecule of

interest.<sup>12</sup> Li et al. used this method to immobilize prostate specific antigen (PSA) antibodies on the surface of SWCNTs to detect the presence of PSA antigens.<sup>187</sup> Importantly, developed functionalities impaired by the succinimidyl ester are highly reactive towards nucleophilic substitution primary and secondary amines present in most biomolecules and thus, this functionalization technique can be considered as a universal strategy in the fabrication of biosensing platforms.<sup>187</sup>

### 5.5.2 *Alternative functionalization techniques*

In this section, some novel techniques for the modification of SWCNT/MWCNT, graphene and carbon particles are presented. There are promising methods for the facile, green and tunable functionalization of MWCNTs using techniques such as free-radical addition.<sup>191</sup> For example, Yang and coworkers reported on the one-step strategy for the covalent modification of MWCNTs with hydroxyl, amidine and carboxyl groups using azo-initiators (azo-nitriles, azoamides and azoamidines) in water media.<sup>191</sup> This work demonstrated that the functional group coverage density can be controlled by adjusting the feed ratio of azo initiators to MWCNTs.<sup>191</sup> An additional advantage of this method is that azo-type initiators are commercially available and inexpensive.

Another technique used for the polymer functionalization of nanotubes is via electro-polymerization. Kurkina et al. demonstrated the electro-polymerization of 4-amino-benzoic acid (ABA) on the surface of SWCNTs, which resulted in the noncovalent wrapping of the nanotubes with carboxyl functionalities.<sup>25</sup> By applying +0.7 V versus the silver chloride electrode (Ag/AgCl) reference electrode, a sufficiently thin (2-3 nm) polymer coating was achieved. Afterwards, EDC/NHS chemistry was used to link the carboxyl functionalities to the amine-terminated ends of DNA probe, resulting in a structure capable of sensing the complementary DNA probe.

Recently, there has been an increased interest in studying the surface modification of nanostructured graphene due to its exceptional physical and chemical properties.<sup>19-21,196,197</sup> For instance, Rezaei et al. presented an efficient one-pot multi-functionalization technique to

modify the surface of nanographene oxide with aldehyde, isocyanide and amine groups.<sup>29</sup> First, graphene oxide (GO) was prepared using flake graphite and potassium permanganate ( $\text{KMnO}_4$ ) added to a 9:1 mixture of concentrated  $\text{H}_2\text{SO}_4/\text{H}_3\text{PO}_4$ . This structure was then carboxylated by subjecting the GO to a potassium hydroxide (KOH) solution and chloretic acid, transforming the hydroxyl groups into carboxyl. In the last step, the Ugi four component reaction was carried out by magnetically stirring the carboxylated graphene (G-COOH) suspension with amine, cyclohexylisocyanide and aldehyde in water at 25°C, which yielded the multiple functionalities at the surface.<sup>29</sup> This functionalization technique, for the first time, was used to study the activity and immobilization of lipase using the Ugi four component scheme.

Polymer functionalization represents an attractive alternative to the improvement of exfoliation, solubility and biocompatibility of CNTs, particularly in the case of protein/enzyme immobilization.<sup>14</sup> Zhan et al. reported the non-covalent attachment of myoglobin to the surface of the functionalized MWCNTs to develop an electrochemical biosensor.<sup>14</sup> In this strategy, poly(methacrylic acid co-acrylamide) (P(MAA-co-AAM)) was blended with MWCNTs in order to attract biomolecules towards the platform via hydrophobic interaction, H-bonding or electrostatic interaction.<sup>14</sup> The use of a polymer matrix nanocomposite facilitated the stabilization of the model protein myoglobin by encapsulating the protein, thus supporting its biocatalytic activity in the developed amperometric biosensor. The developed platform was able to detect hydrogen peroxide with a fast response of less than 3s, a wide linearity range and a considerably low limit of detection.<sup>14</sup>

The modified surface of graphene has also been extensively used in biomedical applications.<sup>19</sup> For instance, Jakus and colleagues demonstrated the 3D printing of a graphene-containing ink (3DG) by blending polylactide-co-glycolide (a highly biocompatible elastomer) and graphene powder.<sup>192</sup> This procedure is represented schematically in Figure 5-9, where the first panel shows the solution blending, deposition preparation and design, followed by 3D scaffold printing and finally, the possible electronic and biomedical applications.<sup>192</sup> The resulting structures were mechanically robust and

flexible, while showing higher conductivities than previously reported 3D-printed carbon materials. To assess the biocompatibility of the created structures, *in vitro* experiments were carried out, revealing that 3DG promotes human mesenchymal stem cell adhesion, viability, proliferation and neurogenic differentiation.<sup>192</sup> Furthermore, *in vivo* experiments were performed in a mouse subcutaneous implant model, showing promising biocompatibility after 30 days of implantation. This favorable behavior could be attributed to the hydroxyl content of the polymer blended graphene, which promoted common interactions between the existing functional groups on the surface of the cells and tissue and the modified graphene surface.<sup>192</sup>

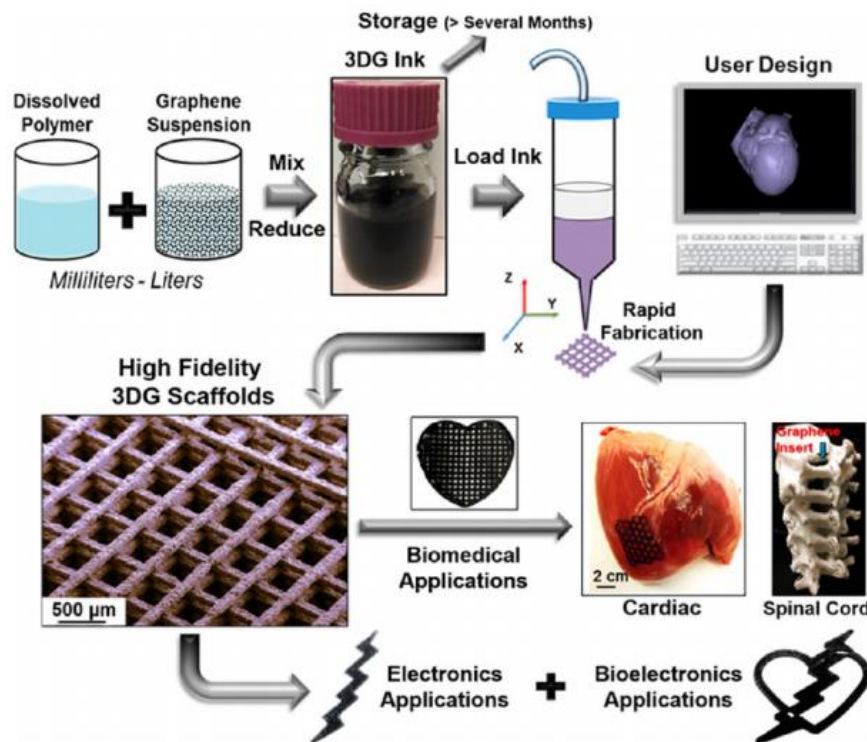


**Figure 5-9.** Production of 3DG ink by polymer blending of polylactide-co-glycolide (a highly biocompatible elastomer) and graphene powder. After mixing, the solution can be scaled up for polymer printing applications. Potential applications of 3DG built architectures include energy storage, bioelectronics, tissue and organ engineering. Reprinted from ref. [65] A. E. Jakus *et al.*, *ACS Nano*, **9**, 2015, 4636.

Surface modification of carbon has allowed other interesting biomedical applications such as *in vivo* delivery of multimodal bioimaging agent nanoparticles (NPs). Rammohan et al. demonstrated the grafting of PEG on the surface of mesoporous carbon nanometer sized

particles (referred to as *nanocapsules*).<sup>22</sup> In a first step, the prepared nanocapsules were loaded with a wide range of bioimaging NPs by *in situ* synthesis methods. The NPs-loaded carbon capsules were then treated with a mixture of H<sub>2</sub>SO<sub>4</sub> and HNO<sub>3</sub> to induce carboxyl groups. The surface of the particles was further modified with thionyl chloride (SOCl<sub>2</sub>) in dimethylformamide (DMF), followed by addition of bis-amino PEG into the mixture. The grafting of PEG provided the surface of the nanocapsules with amino functionalities that were subsequently used to bind immunoglobulin G (IgG) antibodies. The developed nanocapsules served as vehicles for the delivery of pristine hydrophobic and hydrophilic NPs which allowed the bioimaging of many organs in rats, including liver, heart, spleen, lungs, blood pool and muscles.<sup>22</sup> It is important to mention that the biocompatibility, biodistribution and cellular uptake of the nanocapsules were governed by the PEGylation and the presence of antibodies of their surface.<sup>22</sup>

Atomic layer deposition (ALD) can also be used as an interesting alternative technique for the deposition of a fine layer of functionalized materials on the supporting substrate.<sup>198–202</sup> This deposition technique can induce fabrication of the coated substrate with polymer materials that contain reactive functional groups. Therefore, ALD is an indirect strategy for functionalizing different platforms. ALD has also been used for the fabrication of CNT field effect transistor biosensors.<sup>203</sup> Presence of reactive functional groups can facilitate biomolecular attachment to the surface via known different means, such as ionic attraction, covalent bonding, hydrogen bonding or hydrophobic interaction. Furthermore, this technique (ALD) was reported for its application in producing zinc oxide (ZnO) coated MWCNTs to study its health risk effects on humans.<sup>198</sup>

Through the same strategy, nano-layers of different compounds can be deposited on various types of supporting substrates such as carbon nanomaterials through chemical vapor deposition (CVD). In particular, CVD can be used for local coating/functionalization of the carbon materials.<sup>6,78</sup> It is of a great importance to locally deposit substrate on the surface of the supporting material. Local functionalization can be obtained by proper coverage of the surface to leave the section of interest exposed to the CVD. The masking process could be performed by coating the platform with wax or other substitutes prior to the exposure to

coating components used in CVD.<sup>204</sup> In particular, local CVD can be achieved by heating the region of interest up to the cracking temperature of the precursor.<sup>6,78,205</sup> Once the desirable functional groups are generated on the surface, protein immobilization can be successfully done via different forces involved in biomolecular interaction.

## 5.6 *Experimental methods*

To produce gold coated (GC) CNWs, a positive photoresist sacrificial layer was deposited on top of the device in order to select the suspended wire exclusively for deposition. A droplet of positive photoresist (MicroPosit SC1827®) was thoroughly and carefully distributed over the wafer manually using a glass slide. This approach was preferred over spin coating, as samples would occasionally break due to the strong accelerations and viscosity of the resin. Positive photoresist coating: scotch tape was used to protect the regions of the substrate that did not require coating. The layer of photoresist had approximately 60  $\mu\text{m}$ +/-1 $\mu\text{m}$  in height.

After deposition of the photoresist layer, samples were exposed using a rapid prototyping lithography platform (SF-100 XTREME) from Intelligent Micro Patterning LLC. The photolithography parameters were: 7min soft-bake, 6 sec exposure (g-line, 435 nm), and developing time of 45 sec. The exposure pattern consisted of 10 px by 200 px rectangles, which were used to expose the sacrificial layer and uncover each suspended CNW (Figure 5-10a-d).

### 5.6.1 *Gold coating of CNWs*

After coating the samples with the Positive Photoresist Sacrificial layer, samples were covered with a ~10 nm gold layer via conventional gold sputtering using a Q150R ES - Quorum platform (see Figure 5-10d).

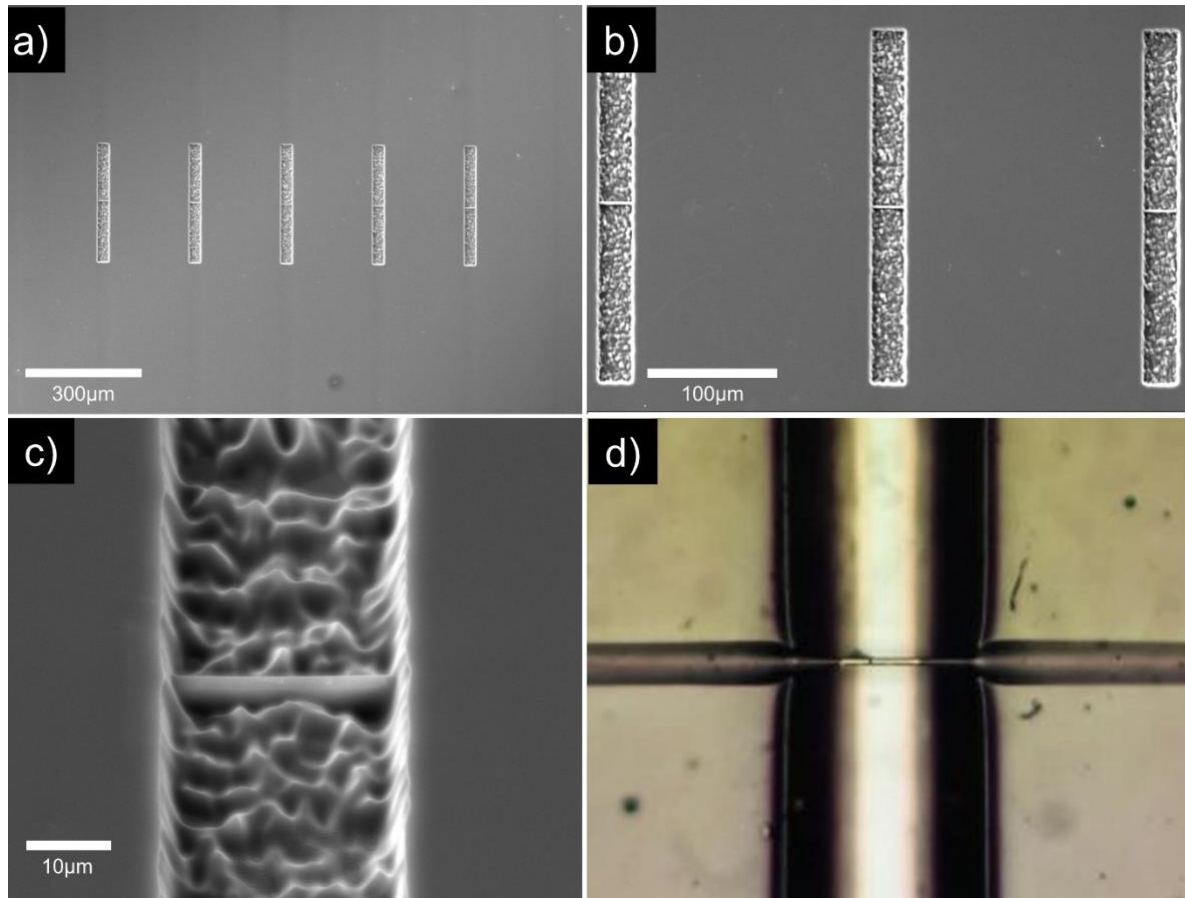


Figure 5-10. SEM micrographs of suspended CNWs with a protective layer of positive photoresist, used for gold coating surface modification. (a) Overview of five samples with rectangular apertures created by exposing the zones of the photoresist where the wires are. (b) Zoom in of the image presented in (a). (c) Further magnification reveals a granular pattern of the photoresist that was not fully developed. (d) Optical Microscope image of a resulting suspended CNW after removing the positive photoresist sacrificial layer.

### 5.6.2 Electrochemical Modification of Carbon Electrodes and Carbon Nanowires

CNWs were subjected to an electrochemical modification (ECM) treatment that consisted in electrooxidizing a chemical compound known as 4-Aminobenzoic acid, which is a bifunctional molecule with an amine and a carboxylic group.<sup>25</sup> Via electrochemical stimulation, this compound can be either grafted on the surface of GC electrodes or electropolymerized as a nanometric layer of functional polymer on the surface of the carbon material. The general scheme for 4-ABA grafting on GC is presented in **Figure 5-11**. Briefly, by applying a positive voltage vs. Ag/AgCl reference electrode (0.7 to 1.2 V),<sup>30</sup> the free

electrons of the amine functionality will be forced to jump into the positive GC interface, effectively occupying the Lowest Unoccupied Molecular Orbital (LUMO) in the  $\pi$ -orbitals of the graphitic material (**Figure 5-11 I,II**). By effect of this electron transfer, the formed amine cation will be prone to deprotonation, as one of the bonding hydrogens will tend to give its bonding electron (**Figure 5-11 II,III**). After this regrouping, the nitrogen atom will form a covalent bond with the GC interface, leaving the carboxylic functionality facing away from the surface.

### Grafting of 4-ABA on Glassy Carbon

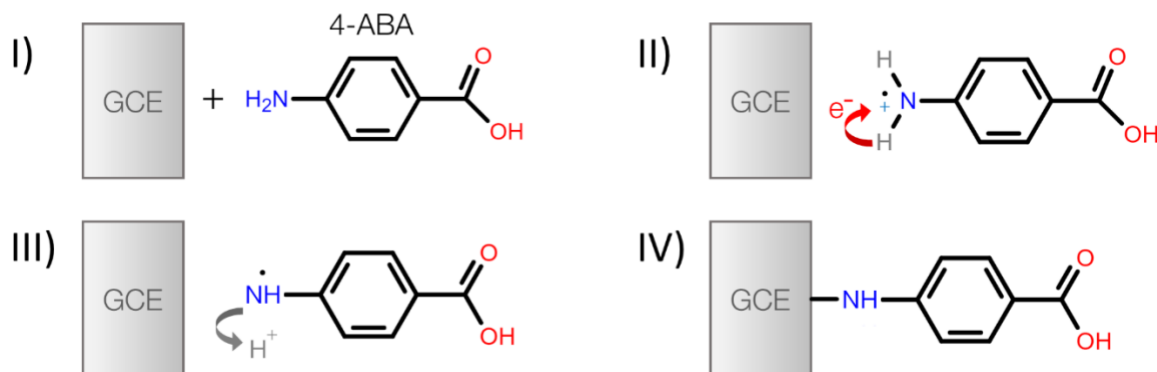


**Figure 5-11.** Scheme showing the covalent attachment of 4-ABA into a GC surface.

The protocol for ECM was the following: carbon microelectrodes were brought into contact with a solution of 4-ABA (3mM) and LiClO<sub>4</sub> (0.1M) in reagent grade ethanol (99.98%). Using four electrodes, we were able to test two pairs of electrodes per experiment. We labeled the electrodes WE1,2 and CE1,2 to denote the working electrodes and counter electrodes, respectively (**Figure 5-12**). The case of the first pair (WE1, CE1) was identified as the working sample to be modified. Similarly, the contiguous pair (WE2, CE2) was used as a control for experiment, which would be in contact with the solution containing the grafting compound, but was not probed electrically (so that in theory, it should not suffer any surface alteration whatsoever). Using WE1CE1, voltage was swept five times from -0.1 to 1.2 V in a cyclic voltammogram, at a speed of 100 mV/s.

Furthermore, the degree of surface functionalization was studied in a qualitative way by introducing a redox couple as an electrochemical probe. Before introducing the 4-ABA solution, a mixture of  $K_3[Fe(CN)_6]$  (1mM) and  $K_4[Fe(CN)_6]$  (1 mM) and KCl 0.5 M was used to analyze the voltammogram of the probe with the unmodified system. After probing, the sample was cleaned using deionized water (MilliQ water), followed by thorough drying. Following the cleaning step, the 4-ABA compound was immobilized electrochemically. Afterwards, rinsing and drying was performed again. Finally, readings of the probe were evaluated after this functionalization procedure to evaluate the qualitative change in the aspect of the cyclic voltammograms and the Electrochemical Impedance Spectroscopy (EIS) values.

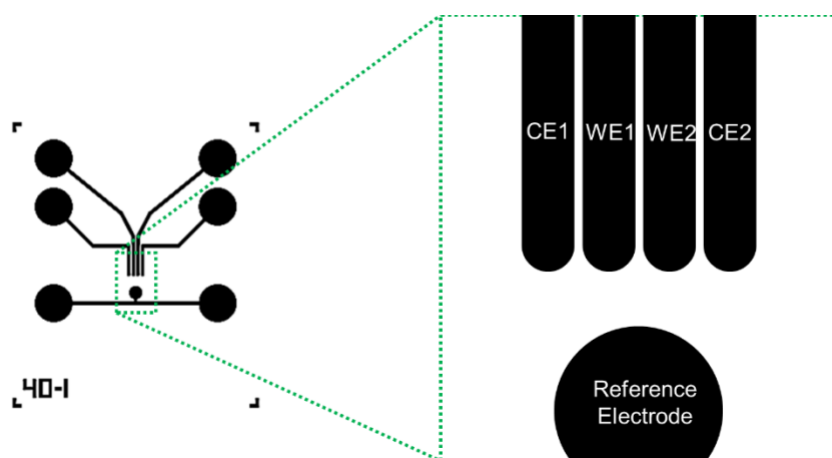


**Figure 5-12.** Schematic of a G40T20.RE electrode, which has 4 digit electrode and a reference electrode. This structure was used to perform the ECM experiments.

## 5.7 Results and discussion

### 5.7.1 Sputtering of CNW samples

In Figure 5-13 an SEM micrograph of a successfully surface modified CNW is shown. This sample shows a clear surface roughness difference from that of a normal CNW. To quantitatively estimate the degree of deposition of gold atoms on the surface of the samples, EDS analysis was performed. It should be noted, however, that this analysis is in the limits of the minimum required thickness of sample [refer to Eq.(2.1) in Chapter 2.2]. EDS analysis

revealed that no modification with gold happened in any region outside the selected window by the positive photoresist sacrificial layer. Several regions within the device were analyzed. Figure 5-14a shows the spectrum reading at one of the ends of the CNW, revealing no metallic content and a predominant carbon composition 95.89%. Indeed, this result is consistent with our previous characterization from Figure 2-5. For that matter, Figure 5-14b and Figure 5-14c were also evaluated, where we show the EDS spectrum at the silicon substrate and the carbon pads, respectively. No evidence of gold was found in those cases. Nonetheless, when the analysis was performed at the middle portion of the wire, the peaks for gold were revealed, as expected (Figure 5-14d). Even though the atomic percentage was low (1.01%), this coating is enough to be easily perceivable under the microscope (Figure 5-10d). The experimentation in this case was limited, but the general scheme should involve the functionalization via known chemistry such as with Mercapto-propionic acid (MPA) incubation.

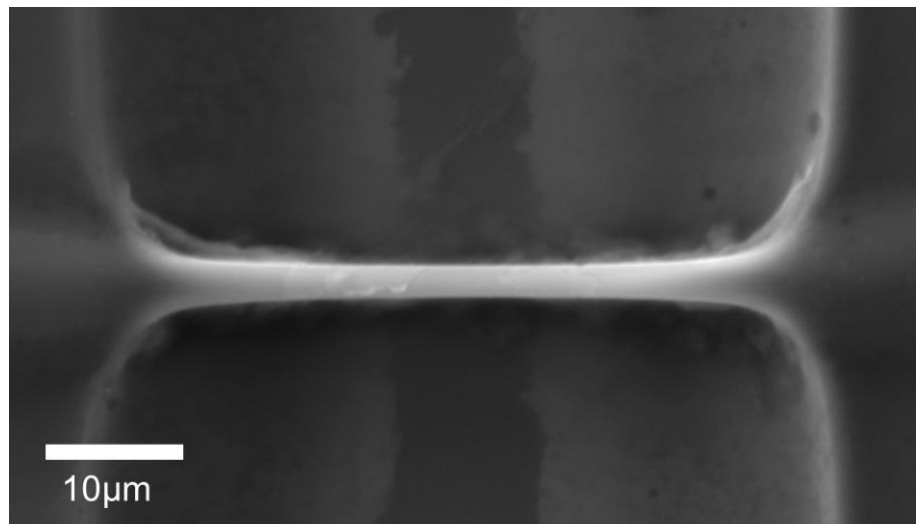


**Figure 5-13.** SEM micrograph of a suspended CNW with a layer of sputtered gold. A different surface morphology is slightly visible in the region coated by gold.

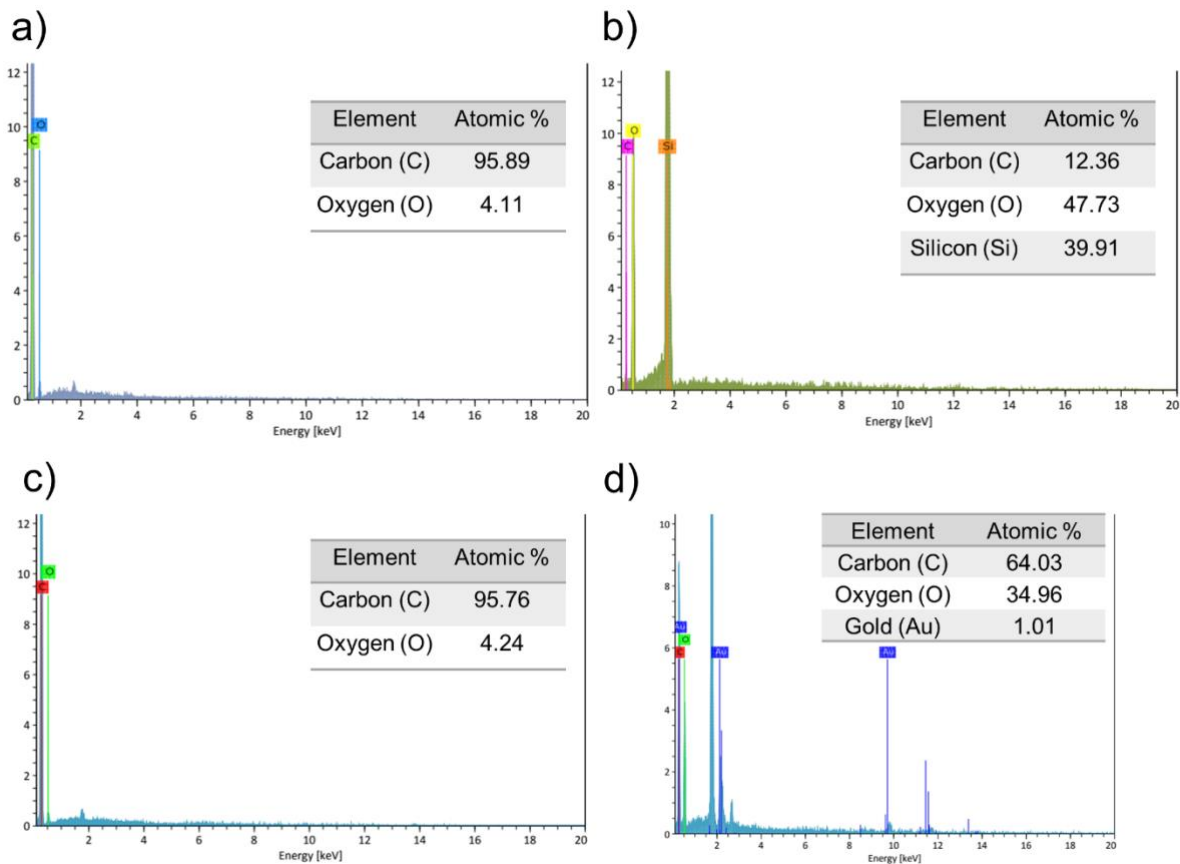


**Figure 5-14.** EDS spectrum of different sections of the C-MEMS device. (a) EDS of a region nearby the end of the CNW. (b) EDS spectrum taking at the surface of the supporting substrate. (c) Spectra obtained at one of the supporting C-MEMS electrodes. (d) EDS at the central portion of the CNW.

### 5.7.2 Electrochemical modification of GC microelectrodes

The results from the ECM experiments are summarized in Figure 5-16a-d. The first experiment consisted in registering the cyclic voltammogram (CV) of the ferri/ferrocyanide redox couple. In Figure 5-16a, the initial profile scanned in the cathodic direction is shown with a continuous line plot. This graph is almost identical to that registered for the control group (cont. line in Figure 5-16b). However, after performing the Electrochemical Modification scheme described above (Figure 5-15), the probe reading is significantly altered. Surface modification of the GC microelectrodes can be concluded as the distance  $\Delta E$  between peak maxima is widened and their intensity reduced, which are evidence of an irreversible modification taking place. This is consistent with the progressive current density drop seen

in Figure 5-15. These two observations led us to believe that the capacitance of the overall electrochemical cell is changing. To verify this claim, we evaluated the EIS response of the electrodes, for an amplitude 10mV and a frequency sweep from 0.01 Hz to 1 MHz. It was found that in the range presented in Figure 5-16c, the magnitude of the real and complex components of the impedance are significantly changed. As expected, the control group experienced a slight modification, but it is not as dramatic as the one produced by the electrochemically modified sample. The same trend is identified in Figure 5-16b, where the peak distance did not change significantly, nor the intensity of the CV current. The slight changes in the EIS spectrum could be due to chemisorption of species in between the ECM and washing steps.

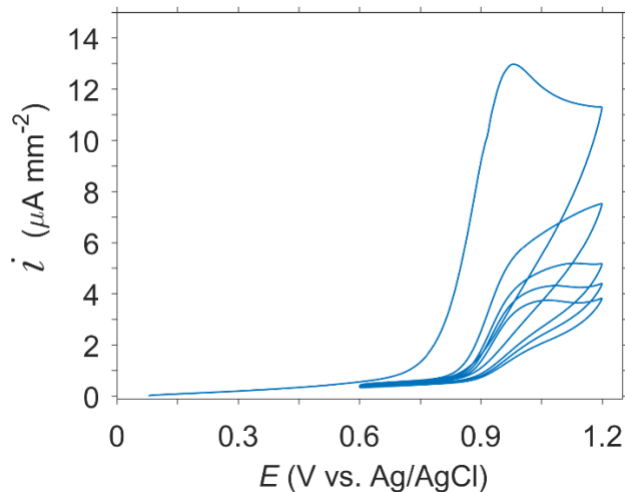


**Figure 5-15.** Cyclic voltammograms of a GC microelectrode in  $\text{LiClO}_4$  solution (100mM) with 3mM 4-ABA, showing the progressive cycles (reducing peak intensity). Scan rate: 100mV/s.

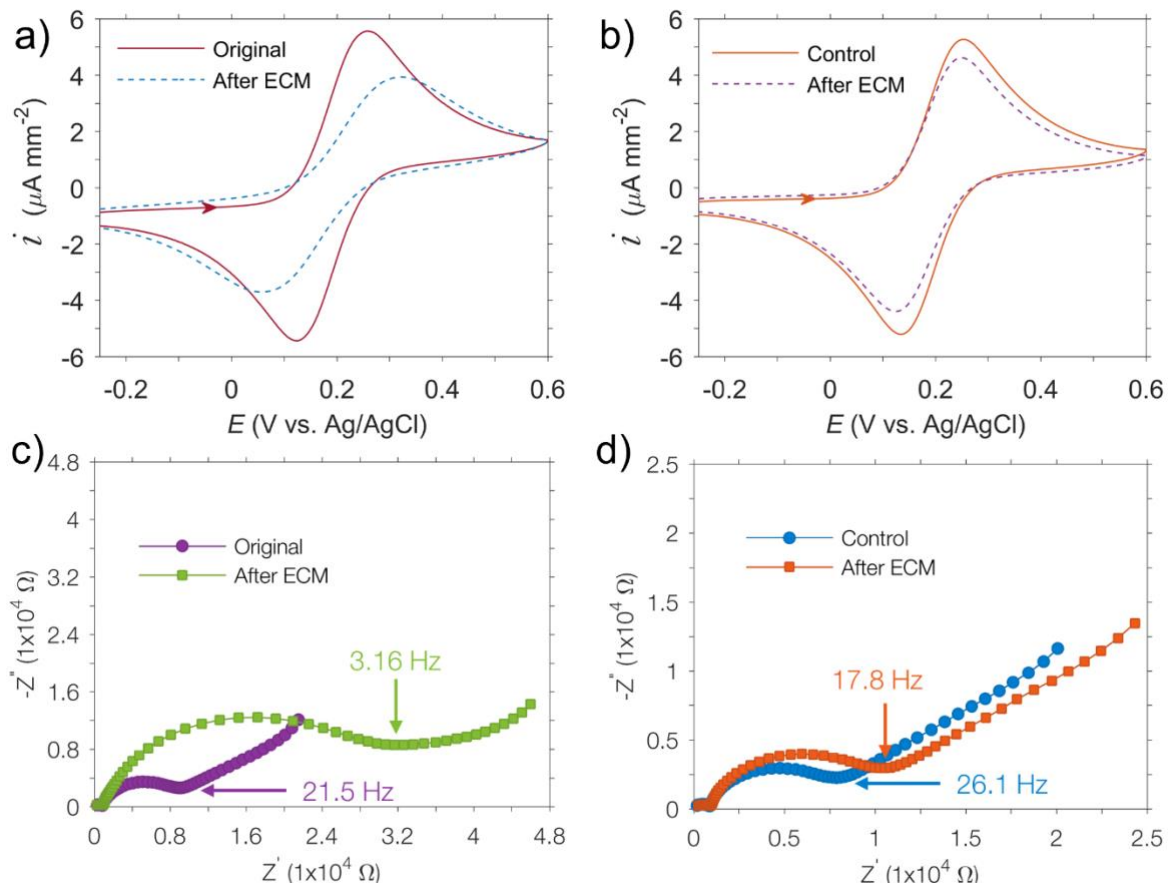


**Figure 5-16.** (a) [Continuous line] Cyclic voltammogram of the probe solution  $\text{K}_3[\text{Fe}(\text{CN})_6]$  (1 mM) and  $\text{K}_4[\text{Fe}(\text{CN})_6]$  (1 mM) and  $\text{KCl}$  0.5 M, obtained at a scan rate of 100 mV/s, in the cathodic direction. Electrodes consisted of GC microelectrodes, in the aforementioned solution. [Dashed-line] Cyclic voltammogram evaluated at the same conditions, after the 4-ABA functionalization. (b) Cyclic voltammogram of the same solution in (a), for the control group before and after 4-ABA functionalization. (d) EIS diagram of the original sample before and after ECM. (d) EIS diagram of the control group, before and after 4-ABA modification.

## 5.8 Summary

Carbon nanostructures have established a paradigm in biosensor platform fabrication owing to their structural properties and versatile electrochemical interface. The use of these materials has paved the way for new applications in diverse fields. Nonetheless, this general concept requires the functionalization in order for the biological recognition event to happen. This chapter attempts to summarize some of the most common techniques for covalent modification of CNWs, as well as some novel methods that have potential in manufacturing.

The experimental results were focused on studying a special kind of modification, electrochemical, which is a logical step when working with GC based materials. As was argued in previous chapters, the microstructures here presented are mostly glassy in composition. The first method that was presented studies the use of advanced manufacturing using a DMD array device to make a sacrificial layer of positive photoresist as a template for gold coating. The second method was studied in greater detail; however, conclusions must be extrapolated for CNW surfaces as these were not directly tested. For any of the two cases, better characterization techniques will have to be employed. The central objective should be to characterize the outermost nanometric layers of the devices in search for useful functional groups that will allow the immobilization of a biomolecule of interest.

## 6 Nanogap Fabrication by Joule Heating of Carbon Nanowires

### 6.1 *Background and motivation*

Nanogaps are a kind of nanostructure that have found application in the fundamental study of micro/nano-particles and molecules.<sup>206–208</sup> Due to their nanometric separation, these structures have also been applied in the manipulation of sub-micrometric particles and biomolecules.<sup>209</sup> The minimum requirement to fulfill these tasks is that the distance between electrodes is in an order of magnitude comparable to that of the probed particles.<sup>210</sup> For instance, electrical probing of single bases of DNA molecules has been proposed by using sub-20 nm nanogaps.<sup>211</sup> Particle manipulation, on the other hand, is usually achieved by application of high electric fields between the nanogap tips to generate trapping through dielectrophoretic forces.<sup>209</sup> Some applications of this principle include assembly of DNA fragments (~27 nm),<sup>211</sup> nanoparticles (20 nm)<sup>212</sup> and micron-long CNTs.<sup>32</sup> In view of the importance of obtaining these structures, researchers have explored several fabrication techniques such as focused-ion beam (FIB),<sup>213</sup> mechanical break junction,<sup>214–216</sup> electron beam lithography (EBL),<sup>217</sup> electron-beam induced oxidation,<sup>218</sup> electrochemical synthesis<sup>219</sup> and oblique angle deposition.<sup>220</sup> Nonetheless, the aforementioned techniques still suffer from poor scalability, low throughput and/or complex processing that requires costly equipment.<sup>217</sup> Thus, few methods have the capability of routinely producing sub-50 nm nanogaps<sup>221</sup>, and even fewer offer the ability to readily integrate them into MEMS.

Another nanogap fabrication strategy consists in inducing the electrical breakdown of metallic nanowires, usually prepatterned by 2D lithographic techniques (EBL, for instance).<sup>208</sup> Even though this technique allows the precise positioning and integration of individual nanowires, EBL has low throughput and is inherently a 2D fabrication method that does not allow the manufacturing of 3D structures. In view of this, an important alternative to such metal-interconnects are one-dimensional CNTs and CNWs which can be used to fabricate nanogaps by electrical field-induced breakdown in order to produce freely-standing gaps.<sup>208,222</sup> In these devices, the resulting nanogaps are dependent on the structural configuration of the electrodes and the substrate that supports them. Therefore, it is desirable

that the position and orientation of CNWs be controlled within a circuit, and that they be connected to metallic electrodes with robust and reproducible ohmic contacts.<sup>36</sup> However, the conventional fabrication schemes for CNTs fail to achieve this task, as NWs must be synthesized, isolated and placed afterwards on the flat substrate, followed by deposition of metallic contacts.<sup>33–35</sup>

In this Chapter, we describe a relatively simple and inexpensive fabrication method of nanogaps based on the electrical breakdown of CNWs by Joule Heating techniques. These nanogap electrodes are fabricated using the CNWs described in Chapters 2 and 3. We observed that at high electric bias CNWs present considerable Joule heating that leads to non-linear current-voltage behavior, gradual thinning and eventually, CNW breakdown, splitting them in half. The maximum current density before breakdown was registered for all samples, and it was estimated to be in the order of  $10^5 \text{ A/cm}^2$ , a magnitude consistent with previous studies on heat diffusion of CNWs.<sup>223–225</sup> Furthermore, a computer simulation was used to study the joule heating temperature distribution that arises in CNWs; it was found that the rate of change of the temperature profile is closely related with the portion of the wire that undergoes sublimation and eventual breaking. The current application allowed us to routinely obtain sub 50 nm carbon nanogaps, with a minimum gap sample of 12 nm.

## 6.2 *Experimental methods*

### 6.2.1 *CNW arrays*

UV photolithography was used to pattern SU-8 2025 (MicroChem Inc., MA, USA) in supporting wall patterns ranging in thickness from 2 to 30  $\mu\text{m}$  and separation from 3 to 50  $\mu\text{m}$ . Afterwards, EMS was used to deposit an SU-8 2002 microfiber over the created walls as described in Chapter 3, section 3.5.1. In order to obtain multiple fibers with similar composition (of length  $L$  and diameter  $D$ ), six supporting walls were fabricated per device, and during the EMS step a single polymer fiber was deposited (see Figure 6-1a).

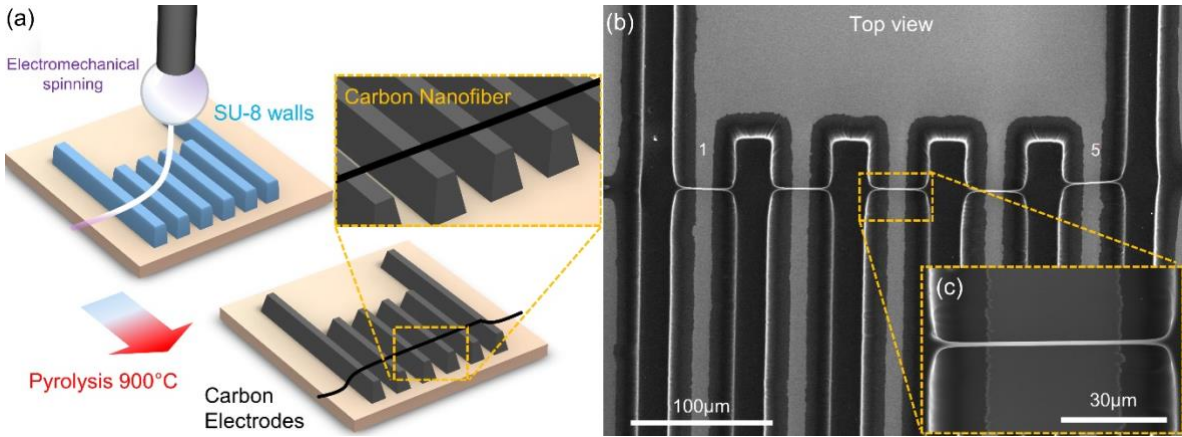


**Figure 6-1.** (a) Fabrication scheme used to produce CNW arrays, combining EMS and carbonization of the structures by pyrolysis. (b) SEM micrograph of the six-wall structure containing five CNWs (top view, numbered 1 through 5). (c) Close-up of an individual suspended CNW between two carbon electrodes.

Once the SU-8 fiber/SU-8 wall compound was obtained, it was converted into GC material by pyrolysis at 900°C in an inert environment (as described in Chapter 2, Section 2.1.2); this process resulted in a monolithic carbon structure with five suspended CNWs of equal  $L$  and  $D$  (Figure 6-1b,c). A total of forty CNWs ranging in  $L$  from 5 to 65  $\mu\text{m}$  and  $D$  from 233 to 2200 nm were produced and tested for nanogap fabrication.

### 6.2.2 Nanogap fabrication

Electrical characterization and joule heating breakdown experiments were performed using a Keithley 2636B source meter and a Kleindiek probe system.<sup>46</sup> For all samples, voltage was varied, starting from 0V to a voltage at which samples experience noticeable heating (evinced by a drop in resistance). Afterwards, samples were left at this constant voltage, to begin joule heating induced breaking. At that moment, the temperature increase due to Joule heating was significantly high at that point to induce the eventual breakdown of CNWs. This failure point revealed itself as a stiff and sudden increase in resistance (producing an open-circuit), resulting in the splitting of the wire in half. Experiments were conducted both at air and

vacuum conditions ( $8 \times 10^{-6}$  Torr) to test atmosphere effects in nanogap fabrication. All geometric measurements ( $D$  and  $L$ ) were performed using a FEI Magellan 400 XHR SEM and a FEI Quanta 3D FEG Dual Beam SEM.<sup>46</sup>

### 6.2.3 *Simulation of Joule Heating effects in CNWs*

A computational model (COMSOL Multiphysics 5.0<sup>©</sup>) was built to estimate the heat transferred to the carbon wires by effect of Joule heating phenomena. In the simulation, CNWs and GC electrodes were identified as different domains. The geometry of CNW was estimated with a cylinder of diameter  $D = 1\mu\text{m}$  and five different lengths were tested (5, 10, 20, 40 and 65  $\mu\text{m}$ ). The geometry of the contacting GC electrodes consisted of rectangular blocks (10  $\mu\text{m}$  thick, 40  $\mu\text{m}$  wide and 120  $\mu\text{m}$  long) to approximate the devices presented in Figure 6-1b,c. The conductivity of GC blocks was set to 100 S/cm as reported earlier,<sup>5</sup> and a value of 300 S/cm was selected based on average conductivity values observed in the forty produced samples.<sup>46</sup> For the thermal conductivity, a value of 6.4 W/m·K was used for GC and 12 W/m·K, for CNWs.<sup>226,227</sup> Furthermore, a diffuse surface boundary condition was set at all the exposed surfaces in the geometry to the ambient, using an emissivity value of 0.8.<sup>228</sup> Only the faces of the GC blocks that contact the substrate were unexposed to the ambient, and their temperature was set to 293.15 K for all simulation purposes.

## 6.3 *Results and discussion*

### 6.3.1 *Electrical testing of CNWs and nanogap fabrication*

A two-probe I-V method, rather than a four-probe technique, was used to test the resistance of the samples. Approximations for this have also been assumed in previously reported experiments, as contact resistance and spreading resistance can be neglected in the devices due to the large geometric difference between the CNW and GC electrodes.<sup>3,38,44</sup> In Figure 6-2a the I-V curve plots for three CNWs of different diameters (all with  $L=44\mu\text{m}$ ) are presented. Due to their diameter difference, different values of  $V_{\max}$  were used (as smaller

CNWs cannot sustain the same voltage that bigger CNWs can). A typical linear response is expected at low voltages (at approximately  $V/V_{\max} < 0.4$ ). Furthermore, heating effects are noticeable when  $V/V_{\max} \sim 0.4$ . This thermal behavior is evinced as a resistance drop in Figure 6-2b (and therefore current increase in the I-V plot of Figure 6-2a). Further increase of the applied voltage ( $V/V_{\max} \geq 0.4$ ) results in the breaking of the CNWs; this event reveals itself as a sudden increase in the resistance curve of Figure 6-2b. As expected, thicker wires are able to sustain higher voltages before breaking. When stimulating wires at voltage  $V_{\max}$ , we can identify two temperature related mechanisms that compete over the effect in the resistance: i) the conductivity of CNWs will tend to be increased as a result of the temperature increase, thereby lowering device resistance;<sup>38,56,100</sup> ii) towards the end of the CNW lifetime, a high resistance reading is observed due to the reduction of the available cross-section for conduction, resulting in thermal runaway of the sample, which reaches temperatures high enough to sublimate carbon.<sup>229,230</sup>

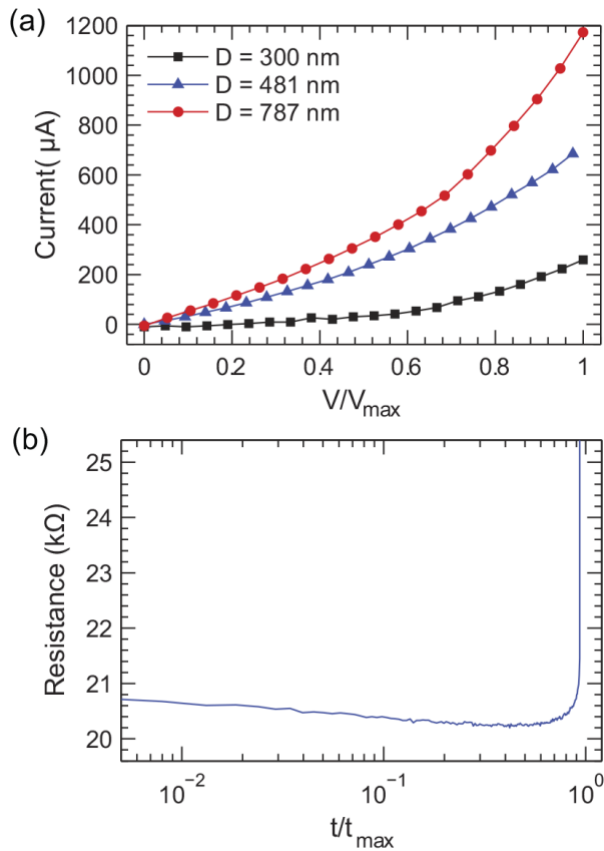


**Figure 6-2.** a) I-V curves for three CNWs of different  $D$  and same length ( $L = 44 \mu\text{m}$ ).  $V_{max} = 3.4 \text{ V}, 5.2 \text{ V}, 3.0 \text{ V}$  and  $t_{max} = 21 \text{ ms}, 43 \text{ ms}$  and  $380 \text{ ms}$  for CNWs with  $D = 300 \text{ nm}, 481 \text{ nm}$  and  $787 \text{ nm}$ , respectively. (b) Resistance evolution in the case  $L = 44 \mu\text{m}$  and  $D = 300 \text{ nm}$ .

Using the procedure detailed above, the 40 samples were stimulated with constant voltages that ranged from 2 to 6V and current density ( $J_M$ ) was registered at the point of breaking. No clear trend was observed in this variable as a function of  $D$ . However, an inverse proportionality dependence on  $L$  was identified (Figure 6-3a), consistent with results for carbon nanofibers produced by other methods and with one-dimensional heat diffusion models.<sup>224,231</sup> The CNW breaking tests confirmed that the breakdown current density for CNWs was in the magnitude of  $\sim 10^5 \text{ A/cm}^2$ , which is a value close to those reported for amorphous CNWs.<sup>232</sup> Such values, however, are lower than those reported for perfectly crystalline structures like CNTs ( $\sim 10^8 \text{ A/cm}^2$ ).<sup>15</sup> This deviation from crystalline structures is expected, given that CNWs in this work are photoresist-derived and thus, are likely to have a predominantly glassy carbon composition.<sup>2</sup> Even if samples would appear to have a low ampacity, the fact that  $J_M$  is dependent on the length of the conductor channel should be

emphasized.<sup>231</sup> In general, short CNWs will have higher  $J_M$  values due to the Joule heating effects in the conductor.<sup>224</sup> We verified such behavior for shorter samples ( $L = 5.0 \mu\text{m}$ ), which placed  $J_M \sim 10^6 \text{ A/cm}^2$ , which are close to those reported for micron-ranged CNWs fabricated by plasma enhanced CVD (with ampacity ranging from  $1 \times 10^6 \text{ A/cm}^2$  to  $5 \times 10^6 \text{ A/cm}^2$ ).<sup>231</sup>

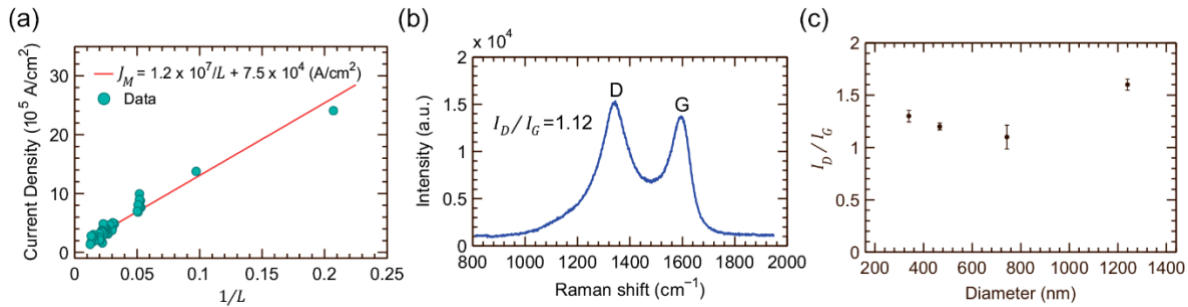


**Figure 6-3.** (a) Dependence of maximum current density at point of CNW breakage with length of CNWs. (b) Raman spectra for CNW with geometry  $D = 467 \text{ nm}$  and  $L = 36.7 \mu\text{m}$ . (c) Scattering plot of the  $I_D/I_G$  ratio for CNWs of different diameters; the error bars represent the standard deviation.

In a material like GC, electric properties are a consequence of the  $\text{sp}^2/\text{sp}^3$  ratio and the overall crystallinity present in the structure. In this work, the pyrolysis temperatures tested (900°C) are expected to yield glassy samples in composition.<sup>233</sup> To evince the crystallinity of the produced CNWs, we decided to evaluate the Raman Spectra of the samples (inVia Qontor, Renishaw plc, UK), as shown in Figure 6-3b. This Figure shows the Raman spectrum of a sample with  $D = 467 \text{ nm}$ , with a higher intensity D-band near  $1350 \text{ cm}^{-1}$  for disordered carbons, compared with the G-band. The peak intensity ratio of the samples  $I_D/I_G$  appears indicated in Figure 6-3b, which is evidence of a higher amorphous carbon microstructure.<sup>84</sup> From 20 CNW samples, we measured  $I_D/I_G$ , finding no significant relationship with the sample diameter (Figure 6-3c). Points are distributed in the  $1 < I_D/I_G < 1.7$  and no clear trend could be identified. While other works on ES have linked the graphitic content of samples with the degree of polymer chain alignment during the spinning process before carbonization,<sup>3</sup> the work here presented did not evince a significant degree crystallization in the samples. Furthermore, the Raman spectra of the samples is consistent with the observations made for  $J_M$  shown in Figure 6-3c. This adds to the fact that the I-V curves obtained for the samples tested show a drop in the resistance which is characteristic of GC

materials, caused by the thermally activated hopping conduction.<sup>4,56,234,235</sup>. Therefore, we conclude that the ampacity of the samples here presented is a consequence of the predominantly GC microstructure.

### 6.3.2 Reduction Nanogap size with CNW length

In Figure 6-4a,b, SEM micrographs of two CNWs with different lengths are shown, along with their produced nanogaps in Figure 6-4c,d. For the 40 samples tested, SEM imaging was used to analyze and measure the average nanogap size and standard deviation. As seen from Figure 6-4c,d, the size of nanogap is downscaled from  $G=140$  nm to  $\sim 12$  nm as  $L$  is reduced from 39.2  $\mu\text{m}$  to 5.0  $\mu\text{m}$ . Figure 6-4e summarizes these findings, showing the nanogap size dependence on the length of CNWs, with a clear trend of longer wires producing increasingly bigger nanogaps. The curve fitting presented in Figure 6-4e portrays the nonlinear relationship between the gap size and the length of the wire. In fact, the ratio between the gap size and the length of CNWs ( $G/L$ ) was found to remain below 0.5% for all the fabricated nanogaps, with a value of 0.24% for the shortest gap (Figure 6-4d). It can be estimated according to that relation that a 5  $\mu\text{m}$  would be needed to create smaller than 12 nm gaps. Moreover, no clear relation between the diameter of CNWs and the nanogap size was detected. This behavior can be explained by the fact that the temperature gradient along the radial direction in one-dimensional nanowires is negligible.<sup>9</sup>

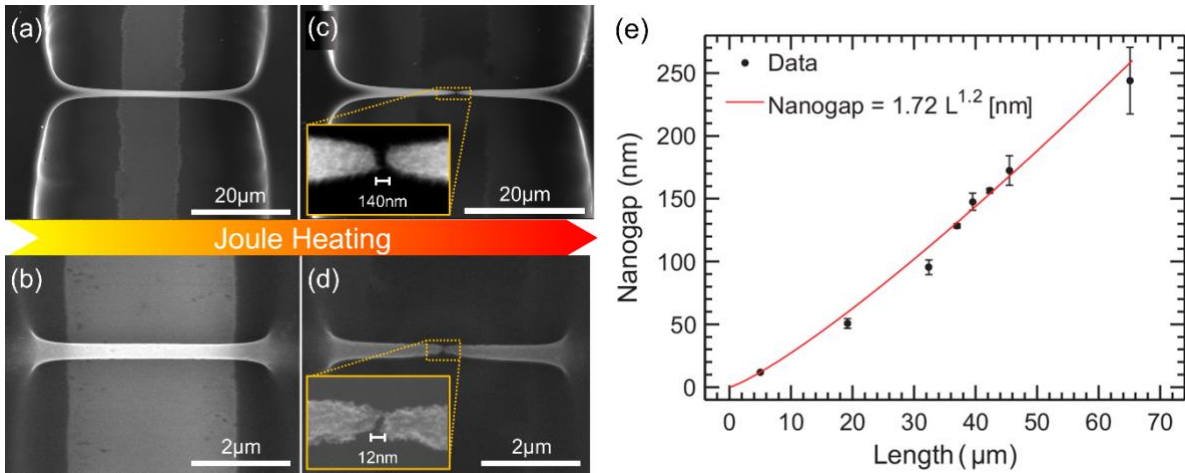


**Figure 6-4.** Nanogaps size dependence on the downscaling of CNWs. (a,b) SEM micrographs of suspended CNWs before electrical breakdown: (a)  $L = 39.2 \mu\text{m}$ ,  $D = 1180 \text{ nm}$  and (b)  $L = 5 \mu\text{m}$ ,  $D = 289 \text{ nm}$ . (c,d) Nanogaps produced after applying the Joule heating current, with gap size of: (c) 140 nm and (d) 12 nm. (e) Dependence of the size of nanogaps with the lenght of the CNW. In this graph, each point represents fibers of similar length and error bars represent the standard deviation of the nanogap size in each case. In the case of the left-most point, only one fiber was tested ( $L = 5 \mu\text{m}$ ).

### 6.3.3 Atmosphere effects on nanogaps

Figure 6-5a shows a CNW ( $L = 65 \mu\text{m}$ ,  $D = 1.06 \mu\text{m}$ ) broken in air and is compared with an adjacent CNW of similar dimensions ( $L = 65 \mu\text{m}$ ,  $D = 1.10 \mu\text{m}$ ) broken in vacuum is shown in (Figure 6-5b). CNWs present very different surface morphology, suggesting that gases present during the breaking event play an important role in the nanogap formation mechanism. Previously, it has been reported how MWCNTs broken in air<sup>33</sup> and SWCNTs heated in atmospheres with different oxygen concentrations presented larger gaps,<sup>222</sup> compared to samples tested in high vacuum; however, our study is not conclusive enough to support this claim in the case of CNWs, and more tests are needed to analyze the effects and dependence nanogap size with the O<sub>2</sub> partial pressure. Nonetheless, I-V tests conducted in CNWs under different atmospheres allowed us to study their ampacity in a qualitative manner. It has been previously reported that Joule heating stimulation activated desorption of gas molecules on CVD grown fibers, that are responsible in part for charge carrier trapping.<sup>34</sup> This desorption mechanism leads to a temporary or permanent alteration of the CNW, depending on whether the fiber was electrically biased in air conditions or in high

vacuum, respectively. We noticed the same trend in our experiments for EMS produced CNWs. Figure 6-5c shows the resistance change in a CNW sample after four successive bias cycles in air for the wire presented in Figure 6-5a. As expected, after each heat application, the resistance decreases (due to the increased current), and after cooling down, the next heating–cooling cycle starts at the same resistance value as the previous experiment. Figure 6-5d shows four successive voltage sweep cycles for the same wire without breaking the sample, operated in a vacuum. For this case, after each cycle, resistance underwent a slight permanent resistance reduction. In addition, it was observed that CNWs stimulated in air conditions support only a fraction (~35%) of the power required to break the sample in a vacuum (see for instance Figure 6-5e). These observations agree with those performed in carbon nanofibers electrically stressed in air conditions, which support lower electrical power before the failure point is reached.<sup>33</sup> Therefore, experiments should be ideally conducted in vacuum conditions to ensure the stability and purity of the nanogap fabrication process.

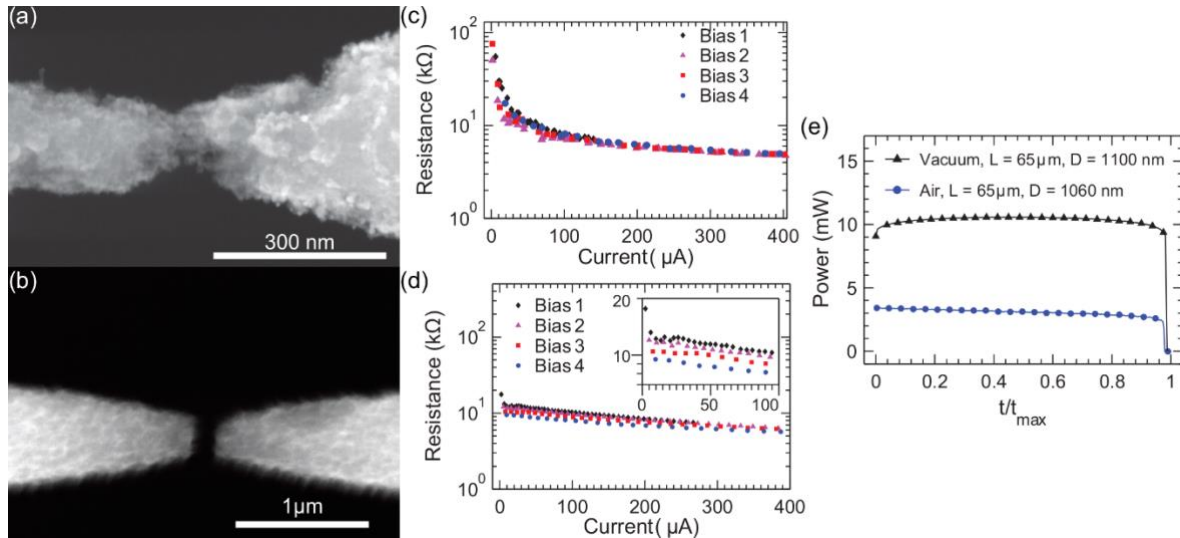


**Figure 6-5.** (a) SEM micrograph of a CNW fabricated in air atmosphere conditions ( $L = 65 \mu\text{m}$  and  $D = 1.06 \mu\text{m}$ ). (b) SEM micrograph of a CNW produced in a high vacuum ( $L = 65 \mu\text{m}$  and  $D = 1.10 \mu\text{m}$ ). (c) Change in resistance of the CNW presented in (a) after application of successive voltage sweeps. (d) Resistance change after successive voltage cycles in vacuum to the CNW presented in (b); the inset of (d) shows a close-up view evidencing the resistance reduction after each stressing cycle. (e) Change in the critical stimulation power in atmosphere and vacuum conditions.

### 6.3.4 Finite Element simulation of CNW Joule heating

In order to study the dependence of electric heating on CNW geometry, we studied the change in the temperature distribution for different values of  $L$  using a 3D finite element simulation. The model was set to solve the electric field and current density from the imposed boundary conditions to derive the steady state temperature distribution in the entire geometric entities by treating the electric current as the heat source. The boundary conditions established for the model were: i) the electric potential across the carbon electrodes was set to  $V_0$ ; ii) the base of the supporting walls (rectangular blocks), which are in contact with the silicon substrate, remain at room temperature (293.15 K). Radiative heat losses were considered, as high temperatures are reached, however, other loss sources such as convective heat transport were neglected, given that samples are considered to be in high vacuum conditions. Figure 6-6a illustrates the temperature distribution ( $L=40 \mu\text{m}$ ), where the central region of the CNW can be seen to be at significantly higher temperature compared to the ends of the wires. Such result is in qualitative agreement with the observation of CNW breaking at their center. Moreover, Figure 6-6b summarizes the effect of length decrease in the temperature profile along the central axis line of the cylindrical wire (bounded by the carbon electrodes). As seen from these plots, a large parabolic temperature variation is contained within progressively shorter lengths, with electrodes acting as heat sinks that cool down the two ends of the CNWs.

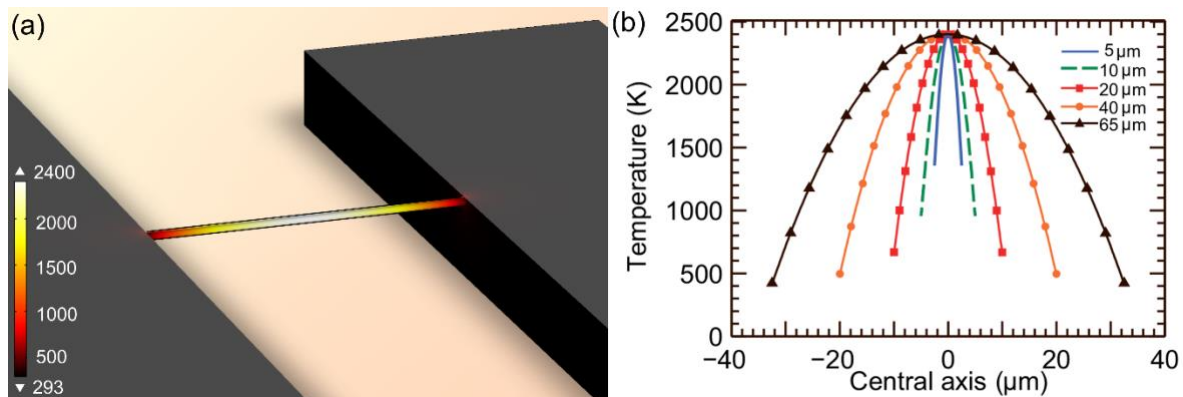


**Figure 6-6.** Finite element simulations of the temperature distribution in CNWs heated by electric currents. (a) A colormap graph of the temperature profile for a CNW with length  $L = 40 \mu\text{m}$  and  $D = 1 \mu\text{m}$ . (b) Cutline profile of the temperature along the axis of the CNW.

The previous model allowed us to study the minimum voltage required to break CNWs. The problem of defining the exact boundary conditions and stimulation parameters (applied voltage) at which a given CNW with a specific geometry will break is non-trivial. Indeed, CNWs are expected to withstand a certain critical temperature  $T_m$  depending upon the conditions of the atmosphere and the stimulation parameters. In other carbon allotropes, such as MWCNTs, this critical temperature has been estimated to be around 2400 K,<sup>16</sup> and 3200 K in high vacuum conditions.<sup>33,236</sup> For that lower bound, the value corresponds to the sublimation temperature of graphite in vacuum conditions.<sup>237</sup> Because the electrospun CNWs presented in this work have been shown to be mixture of glassy and graphitic carbons,<sup>3,44</sup> we expect them to be less thermodynamically stable than MWCNTs, therefore suggesting that their breaking point lies around 2400 K in a vacuum (or less). Moreover, we predict that for a given CNW with specific geometry, there will be a certain minimum threshold voltage  $V_m$  that will cause the structure to heat up uncontrollably to maximum temperature  $T_m$ ; our experiments place such value in the range between 2 and 6 V. Evidently, any higher bias  $V_0 \geq V_m$  would also break, perhaps even with a more sudden breaking due to excessive Joule heating and thermal runaway effects.

Taking into account the specified problem, the applied voltage boundary condition,  $V_0$ , was estimated so that wires of the different  $L$  would reach the same critical temperature, as shown in Figure 6-6b. In the simulation, these values were found to be 2.372, 2.468, 2.539, 2.606 and 2.682 V for fibers with lengths  $L = 5, 10, 20, 40$  and  $65\text{ }\mu\text{m}$ , respectively. Comparison of these points to the values where nonlinearity starts in I-V curves presented in Figure 6-2 suggests that the calculated voltages provide a fair estimation of the voltage conditions necessary to begin electrical breakdown. The presented parametric study on length can be used to compare directly the temperature gradient that is known to cause electric breakdown in samples of different  $L$ . It is clear from Figure 6-6b that length has an impact on the temperature gradient, with shorter samples featuring narrower temperature profiles. This length dependency becomes apparent if we consider that CNWs follow the classical Joule heating heat equation. According to the theory, an approximately one-dimensional cylindrical wire system with constant cross-sectional area  $A$ , will experience a temperature distribution of the form:<sup>236</sup>

$$A\nabla(\kappa \nabla T) + (I \cdot V)/L = 0 \quad (6.1)$$

where  $\kappa$  is the thermal conductivity,  $T$  the temperature,  $I$  the applied current at the applied voltage  $V$  and  $L$  the length. It can be shown that the solution to Eq.(6.1) is given by <sup>16</sup>:

$$T(x) = T_m + (T_0 - T_m) \left( \frac{2x}{L} \right)^2 \quad (6.2)$$

where  $T_0$  is the temperature at the ends of the CNW,  $T_m$  the maximum temperature reached at the center, given by  $T_m = T_0 + \frac{L}{8\kappa A}(I \cdot V)$ , and  $x \in [-L/2, L/2]$ . Notice that in Eq. (6.2), the dependence of the thermal and electrical conductivities with  $T$  has been neglected in the first order approximation. Considering the case in which CNWs have the same cross-sectional area  $A$  and break at the same critical temperature  $T_{m,0}$ , Eq. (6.2) evinces that the temperature gradient is directly related to the geometrical features of the wire. In the case of shorter CNWs, the second term of Eq.(6.2) will increase in value, resulting in a stiff temperature gradient solution. This behavior is associated with a high temperature region in the middle of the CNW that will lead to smaller nanogaps. In short, these results, along with the computed temperature distributions are consistent with the experimental evidence of nanogap scaling with length illustrated in Figure 6-4e.

#### 6.4 Summary

In Chapter 6, the simple and inexpensive manufacturing technique for the fabrication of single suspended CNWs via Joule Heating was presented. This technique can be used to create  $\sim 12$  nm nanogap by merging of EMS and UV-photolithography. Such methods allowed us to control the length, positioning and orientation of suspended CNWs, as well as the fabrication of devices with multiple wires. Furthermore, CNWs were integrated with carbon electrodes through ohmic contacts, which obviated the use of complex metallic bonding steps. We found that the nanogap dimensions and the maximum current density in CNWs ( $\sim 10^5$  A/cm<sup>2</sup>) are length dependent. Moreover, samples tested in ambient conditions

experienced a 65% reduction in supported power when compared to samples tested in vacuum with similar geometries.

A computational model was developed to study the length dependence of nanogaps, which suggested that the temperature distribution of Joule heated wires is parabolic, with increasingly steeper temperature distributions for samples below  $L = 20 \mu\text{m}$ . Following the observed experimental trend, to obtain smaller gaps, as required for most molecular electronics applications, CNWs shorter than  $5 \mu\text{m}$  would be needed. Nonetheless, the challenge in obtaining shorter nanogaps with the proposed methodology lies in the limitations of the conventional UV-photolithography used to prepare the contacting electrodes. Indeed, the fabrication of supporting SU-8 walls becomes increasingly complex and delicate for smaller features. Therefore, optimization and improvement of photolithography will be required to produce short enough CNWs by Joule Heating.

## 7 Concluding Remarks

With the advent of nanotechnology, the fundamental study of nanostructures has become a paradigm of modern research. As scientists strive to integrate these structures into relevant applications, new unmet challenges emerge that require the merging of multidisciplinary fields in hopes of producing new solutions. The realistic integration of structures such as the presented CNWs into highly sensitive impedance nanobiosensors will require the development of not only surface chemistry engineering, but also relevant manufacturing procedures that will catapult these nanodevices into out-of-the-lab applications. The presented dissertation explored AdAM techniques with relevant application in contemporary research that have promising characteristics over current CNW fabrication techniques. These techniques (EMS and MPP) are in general more amenable to manufacturing and automated fabrication, which are key aspects on the grounds of industrial applications. Nonetheless, their merging into C-MEMS is a newborn field that will require the investigation of their compatibility with pyrolysis techniques.

In the presented work, the influence of the fabrication variables was studied in detail for both EMS and MPP. The electrical properties of CNWs produced by EMS showed advantageous characteristics, such as: 1) Ohmic contacts to the CNW structure; 2) high reproducibility in the order of  $D = 204$  nm and 3) high aspect ratio (~321). These structures were found to be composed mostly out of GC according to the obtained Raman Spectroscopy data and the thermal-dependent resistance measurements. Furthermore, an application of such structures was explored, which consisted in the use of Joule Heating currents to routinely produce sub-50nm nanogaps, relevant in the study of microfluidic trapping. The size of nanogaps was found to be dependent on the length of CNWs, a parameter that can be controlled with the precision of the used photolithography equipment.

MPP experimentation allowed us to determine a functional relationship between laser power, scan velocity and linewidth resolution (diameter of structures), before and after pyrolysis. This was achieved through a detailed theoretical derivation of linewidth resolution as a function of fabrication parameters, which was later compared to the experimental

measurements of voxel linewidth. We believe this is the first systematic study that attempts to analyze these variables after carbonization of the structures. Even though pyrolyzed photoresists are expected to suffer a semi-isometric shrinkage of their features, no experimental attempt had been performed to finely analyze this behavior for MPP structures. Thus, the work is relevant in that: 1) a new material for MPP is being explored (pyrolyzed SU-8) and 2) a careful study is presented over the optimization of fabrication parameters.

The detailed study of the modification of carbon nanostructures allowed us to pin down some of the fundamental requirements that these materials require to become relevant biosensor platforms in the field of analytical devices: 1) the composition of the surface chemistry, and in particular the presence of desirable functionalities (-COOH, -OH and -NH<sub>2</sub>); 2) the surface-to-volume ratio and surface roughness; 3) wettability of the surface and 4) the electrochemical activity of the surface in relevant media (buffer). As found in the literature review, the electrochemical interface of Carbon allows a remarkable sensitivity towards electron transfer transduction. It is of particular interest to evaluate the effects that different surface functionalities will have on the efficiency of interfacial electronic transfer. Additionally, a surface modification scheme based on electrochemical modification of GC through the use of a bifunctional molecule (4-Aminobenzoic Acid) was tested. A qualitative interpretation of the data was presented, which can be complemented with specific surface characterization techniques in future dissertations.

### 7.1 *Future work*

Although significant progress was made on the grounds of AdAM optimization for CNW production, the present dissertation opens unanswered questions and pending research that will need to be investigated to complete the application of CNWs as impedance biosensors. Additionally, more studies will be required to fully understand EMS and MPP techniques from a control engineering point of view. The following is a list of suggested future work that could be carried out taking this dissertation as a starting point:

### *7.1.1 EMS of CNWs*

- The presented EMS protocol yielded better results than those reported in the literature in terms of repeatability and minimum CNW dimensions. However, this improvement was not analyzed in terms of the rheological properties of the new polymeric solution. A thorough study on these properties would elucidate why this mechanism is advantageous over previous methodologies.
- The soft-baking of SU-8 microwires was explored as a way of linewidth/diameter reduction. However, it is necessary to determine exactly why these microwires were not successfully pyrolyzed. Can the pyrolysis protocol be modified to optimize for soft-baked SU-8 microwires?
- While the conductivity of the CNWs obtained with EMS “Method 2” offered a fair reproducibility, it is significantly lower in magnitude than those reported for CNWs produced by FFES and EMS. More electrical testing of CNW samples should be carried out to draw a proper conclusion.
- The specific constituents of the SU-8 materials are known to affect the cross-linking mechanism. A detailed study of the polymerization mechanics as a function of variables such as photo-initiator concentration, solvent content, etc, could help minimize feature size and optimize the exposure procedure.

### *7.1.2 MPP of CNWs*

- A study of the possibility of surface modification of CNWs fabricated by MPP is necessary to evaluate their possible applications in nanobiosensors and functional devices.
- A thorough material characterization of CNWs produced by MPP is in order. No scientific studies have been carried out on the mechanical properties of CNWs

derived by pyrolysis of MPP photoresins. Determination of atomic percentages (carbon, oxygen) could help evince the conformation of these structures.

- The GC derived by MPP has not been studied in terms of its electrical properties, although it is expected to be highly similar to microscopic, photoresist derived GC. To address this task, an effective way of making electrical contacts to the CNWs is in order. One way of achieving this could be the use of hybrid lithography, by which micro-to-mesoscale interfacing could be built using conventional UV-photolithography. MPP can then be used to fabricate the SU-8 nanowires exclusively.<sup>47</sup>
- The present dissertation studied a special case of MPP, which is Two Photon Absorption (2PA). Nonetheless, if the proper equipment is available, 3PA can be performed in theory. The analysis of the polymerization thresholds and minimum linewidth resolution should be investigated to reduce the size of voxels.
- The present work did not study the relationship between voxel length and voxel axial diameter. It is expected that the aspect ratio between these features will change as a function of fabrication parameters. Furthermore, the difference in size between these amounts could impact the mechanical properties of the produced CNW structures.
- Another relevant study would be to test the limits of the hypothesis of semi-isometric shrinkage during pyrolysis. This could be examined by creating SU-8 supporting structures of different heights that would result in more dramatic shrinkage in the axial direction of the wires. Material properties of GC could be altered as a result of this shaping procedure. Furthermore, testing of other pyrolysis temperatures could also have an impact on device conductivity and mechanical properties.
- A thorough examination of the threshold pyrolysis conditions should be performed. In this study, TPP structures did not survive in general for  $D < 1400$  nm. Such limit should be evaluated for other temperature conditions, for instance.

### *7.1.3 CNWs as biosensing structures*

- In order to create a biosensor platform from suspended CNWs, it will be necessary to test the surface modification scheme here proposed on such structures. Testing should be carried out at each step of the modification to evaluate and confirm the functionalization. Techniques that could be used to this end include Electrochemical Impedance Spectroscopy (EIS), Cyclic voltammetry (CV), Differential Pulse Voltammetry (DPV), Chronoamperometry, amongst others.
- The impedance spectrum of CNWs should be analyzed under relevant buffer media. Buffers could be tested, such as Phosphate Buffered Saline. In general, the impedance magnitude of the devices is expected to be pH dependent.
- Before carrying out a biosensing application, it would be advantageous to perform substantial surface characterization of the structures (both GC electrodes and CNWs). Techniques that could be used to this end include X-ray Photoelectron Spectroscopy (XPS), Fourier Transform Infrared Spectroscopy (FTIR), Water contact angle (WCA), Atomic Force Microscopy (AFM) and Raman Spectroscopy.
- In the case of a biosensing application for CNWs, for example, the antibody/antigen complex should be studied in detail. Moreover, the immobilization protocol that will be followed to attach the proteins should be studied as a function of analyte concentrations to perform calibration curves. Afterwards, the principle should be tested on the suspended CNWs, to check for measurable changes in the impedance spectrum.

### *7.1.4 Nanogaps in CNWs*

- In order to reduce the size nanogaps produced by Joule heating, the length of the conductor channel must be reduced. This can be achieved by more sophisticated

lithography techniques or advanced lithography, such as MPP. In this way, sub-5 nm nanogaps could find potentially find application in the field of molecular electronics.

- The Joule heating procedure used in this thesis was relatively simple, using only constant stimulation (voltage or current) to create the nanogaps. A complex routine could be used to control the stimulation current/voltage as a function of the probed resistance at a given time. Furthermore, voltage/current pulses could be used instead of DC to produce a highly concentrated amount of heat at the central portion of the wire, thus reducing the size of the generated nanogap.

## References

- 1 M. J. Madou, *Fundamentals of microfabrication: the science of miniaturization*, CRC press, 2002.
- 2 C. Wang and M. Madou, *Biosens. Bioelectron.*, 2005, **20**, 2181–2187.
- 3 S. Sharma, A. Sharma, Y. K. Cho and M. Madou, *ACS Appl. Mater. Interfaces*, 2012, **4**, 34–39.
- 4 A. A. Balandin, *Nat. Mater.*, 2011, **10**, 569–581.
- 5 O. J. A. Schueller, S. T. Brittain, C. Marzolin and G. M. Whitesides, *Chem. Mater.*, 1999, **9**, 1399–1406.
- 6 M. J. Madou, V. H. Perez-Gonzalez and B. Pramanick, *Carbon: The Next Silicon?: Book 2--Applications*, Momentum Press, 2016.
- 7 A. Le Goff, M. Holzinger and S. Cosnier, *Analyst*, 2011, **136**, 1279–1287.
- 8 F. Patolsky, G. Zheng and C. M. Lieber, 2006, **1**, 51–65.
- 9 F. Lonard, *Appl. Phys. Lett.*, 2011, **98**, 2009–2012.
- 10 G. Zheng and C. M. Lieber, *Methods Mol. Biol.*, 2011, **790**, 223–237.
- 11 X. Guo, A. A. Gorodetsky, J. Hone, J. K. Barton and C. Nuckolls, *Nat. Nanotechnol.*, 2008, **3**, 163–7.
- 12 R. J. Chen, Y. Zhang, D. Wang and H. Dai, *J. Am. Chem. Soc.*, 2001, **123**, 3838–3839.
- 13 A. Star, Y. Liu, K. Grant, L. Ridvan, J. F. Stoddart, D. W. Steuerman, M. R. Diehl, A. Boukai and J. R. Heath, *Macromolecules*, 2003, **36**, 553–560.
- 14 K. Zhan, Y. Chen, H. Liu, H. Zhang, Y. Chen, H. Ni, M. Wu and D. Sun, *J. Electroanal. Chem.*, 2014, **724**, 80–86.
- 15 S.-B. Lee, K. B. K. Teo, L. a. W. Robinson, A. S. Teh, M. Chhowalla, D. G. Hasko, G. a. J. Amaratunga, W. I. Milne and H. Ahmed, *J. Vac. Sci. Technol. B*, 2002, **20**, 2773–2776.
- 16 S. B. Singer, M. Mecklenburg, E. R. White and B. C. Regan, *Phys. Rev. B - Condens. Matter Mater. Phys.*, 2011, **84**, 1–8.
- 17 C. Schönenberger and L. Forro, *Phys. World*, 2000, **13**, 37–41.
- 18 V. Georgakilas, M. Otyepka, A. B. Bourlinos, V. Chandra, N. Kim, K. C. Kemp, P.

- Hobza, R. Zboril and K. S. Kim, *Chem. Rev.*, 2012, **112**, 6156–6214.
- 19 V. Georgakilas, J. N. Tiwari, K. C. Kemp, J. A. Perman, A. B. Bourlinos, K. S. Kim and R. Zboril, *Chem. Rev.*, 2016, **116**, 5464–5519.
- 20 A. Bonanni, A. H. Loo and M. Pumera, *TrAC - Trends Anal. Chem.*, 2012, **37**, 12–21.
- 21 M. S. Artiles, C. S. Rout and T. S. Fisher, *Adv. Drug Deliv. Rev.*, 2011, **63**, 1352–1360.
- 22 A. Rammohan, G. Mishra, B. Mahaling, L. Tayal, A. Mukhopadhyay, S. Gambhir, A. Sharma and S. Sivakumar, *ACS Appl. Mater. Interfaces*, 2016, **8**, 350–362.
- 23 C. Staii, A. T. Johnson, M. Chen and V. Pennsyl, *Nano Lett.*, 2005, **5**, 1774–1778.
- 24 K. Besteman, J.-O. Lee, F. G. M. Wiertz, H. A. Heering and C. Dekker, *Nano Lett.*, 2003, **3**, 727–730.
- 25 T. Kurkina, A. Vlandas, A. Ahmad, K. Kern and K. Balasubramanian, *Angew. Chem. Int. Ed. Engl.*, 2011, **50**, 3710–4.
- 26 X. Dong, Y. Shi, W. Huang, P. Chen and L. J. Li, *Adv. Mater.*, 2010, **22**, 1649–1653.
- 27 N. Yang, X. Chen, T. Ren, P. Zhang and D. Yang, *Sensors Actuators, B Chem.*, 2015, **207**, 690–715.
- 28 F. Patolsky, G. Zheng and C. M. Lieber, *Anal. Chem.*, 2006, **78**, 4260–4269.
- 29 A. Rezaei, O. Akhavan, E. Hashemi and M. Shamsara, *Chem. Mater.*, 2016, **28**, 3004–3016.
- 30 J. Liu, L. Cheng, B. Liu and S. Dong, 2000, 7471–7476.
- 31 S. Banerjee, T. Hemraj-Benny and S. S. Wong, *Adv. Mater.*, 2005, **17**, 17–29.
- 32 A. Vijayaraghavan, S. Blatt, D. Weissenberger, M. Oron-Carl, F. Hennrich, D. Gerthsen, H. Hahn and R. Krupke, *Nano Lett.*, 2007, **7**, 1556–1560.
- 33 P. G. Collins, M. Hersam, M. Arnold, R. Martel and P. Avouris, *Phys. Rev. Lett.*, 2001, **86**, 3128–3131.
- 34 S. Maeda, P. Wilhite, N. Kanzaki, T. Yamada and C. Y. Yang, *AIP Adv.*, 2011, **1**, 22102.
- 35 P. G. Collins, M. S. Arnold and P. Avouris, *Science (80-)*, 2001, **292**, 706–709.
- 36 A. Vijayaraghavan, M. Oron-Carl, S. Blatt, A. Vijayaraghavan, S. Blatt, D. Weissenberger, M. Oron-Carl, F. Hennrich, F. Hennrich, D.

- Gerthsen, H. Hahn, D. Gerthsen, H. Hahn and R. Krupke, *Nano Lett.*, 2007, **7**, 1556–60.
- 37 M. M. Shulaker, G. Hills, N. Patil, H. Wei, H. Y. Chen, H. S. Wong and S. Mitra, *Nature*, 2013, **501**, 526–530.
- 38 Y. Lim, J. Heo, M. Madou and H. Shin, *Nanoscale Res. Lett.*, 2013, **8**, 1–9.
- 39 W. S. Lee, Y. S. Park and Y. K. Cho, *ACS Appl. Mater. Interfaces*, 2014, **6**, 12189–12195.
- 40 S. K. Nataraj, K. S. Yang and T. M. Aminabhavi, *Prog. Polym. Sci.*, 2012, **37**, 487–513.
- 41 G. Canton, G. Bisht, L. Kulinsky and M. Madou, *Adv. Mater. Res.*, 2012, **628**, 43–49.
- 42 D. Sun, C. Chang, S. Li and L. Lin, *Nano Lett.*, 2006, **6**, 839–842.
- 43 Y. Huang, Y. Duan, Y. Ding, N. Bu, Y. Pan, N. Lu and Z. Yin, *Sci. Rep.*, 2014, **4**, 1–9.
- 44 G. Canton, T. Do, L. Kulinsky and M. Madou, *Carbon N. Y.*, 2014, **71**, 338–342.
- 45 G. Canton, L. Kulinsky and M. J. Madou, in *2013 IEEE International Symposium on Advanced Packaging Materials*, IEEE, 2013, pp. 230–239.
- 46 A. Salazar, B. Cardenas-Benitez, B. Pramanick, M. J. Madou and S. O. Martinez-Chapa, *Carbon N. Y.*, 2017, **115**, 811–818.
- 47 C. Eschenbaum, D. Großmann, K. Dopf, S. Kettlitz, S. Valouch and U. Lemmer, 2013, **21**, 29921–29926.
- 48 T. Baldacchini, *Three-Dimensional Microfabrication Using Two-Photon Polymerization*, 2015, vol. 1542.
- 49 J. Bauer, A. Schroer, R. Schwaiger and O. Kraft, *Nat. Mater.*, 2016, **15**, 438–443.
- 50 J. Bauer, A. Schroer, R. Schwaiger and O. Kraft, *Nat Mater*, 2016, **15**, 438–443.
- 51 Y. Daicho, T. Murakami, T. Hagiwara and S. Maruo, *Opt. Mater. Express*, 2013, **3**, 875.
- 52 A. Zakhurdaeva, P.-I. Dietrich, H. Hölscher, C. Koos, J. G. Korvink and S. Sharma, *Micromachines*.
- 53 R. Martinez-Duarte, *Micromachines*, 2014, **5**, 766–782.
- 54 O. J. A. Schueller, S. T. Brittain and G. M. Whitesides, *Adv. Mater.*, 1997, **9**, 477–

- 55 A. Mardegan, R. Kamath, S. Sharma, P. Scopece, P. Ugo and M. Madou, *J. Electrochem. Soc.*, 2013, **160**, B132–B137.
- 56 B. A. Samuel, R. Rajagopalan, H. C. Foley and M. A. Haque, *Nanotechnology*, 2008, **19**, 275702.
- 57 D. Guyomard, T. Osaka and M. Datta, *New trends in electrochemical technology: energy storage systems for electronics*, 2000.
- 58 R. Martinez-duarte, R. Gorkin and M. J. Madou, *Lab Chip*, 2010, **10**, 1030–1043.
- 59 J. I. Heo, D. S. Shim, G. T. Teixidor, S. Oh and M. J. Madou, *J. Electrochem. Soc.*, 2011, **158**, 76–80.
- 60 D. Sharma, J. Lee, J. Seo and H. Shin, *Sensors*.
- 61 S. Sharma and M. Madou, *Bioinspired, Biomim. Nanobiomaterials*, 2012, **1**, 252–265.
- 62 S. Ranganathan, R. McCreery, S. M. Majji and M. Madou, *J. Electrochem. Soc.*, 2000, **147**, 277.
- 63 C. S. Sharma, S. Patil, S. Saurabh, A. Sharma and R. Venkataraghavan, *Bull. Mater. Sci.*, 2009, **32**, 239–246.
- 64 R. R. Kamath and M. J. Madou, *Anal. Chem.*, 2014, **86**, 2963–2971.
- 65 B. Pramanick, A. Salazar, S. O. Martinez-Chapa and M. J. Madou, *Carbon N. Y.*, 2017, **113**, 252–259.
- 66 S. Sharma, R. Kamath and M. Madou, *J. Anal. Appl. Pyrolysis*, 2014, **108**, 12–18.
- 67 D. Benoit, J.-F. Bresse, L. Van't Dack, H. Werner and J. Wernisch, *Microbeam and nanobeam analysis*, Springer Science & Business Media, 2012, vol. 13.
- 68 S. K. Nataraj, K. S. Yang and T. M. Aminabhavi, *Prog. Polym. Sci.*, 2012, **37**, 487–513.
- 69 G. S. Bisht, G. Canton, A. Mirsepassi, L. Kulinsky, S. Oh, D. Dunn-Rankin and M. J. Madou, *Nano Lett.*, 2011, **11**, 1831–1837.
- 70 A. Chen and S. Chatterjee, *Chem. Soc. Rev.*, 2013, **42**, 5425–38.
- 71 L. Zhang, A. Aboagye, A. Kelkar, C. Lai and H. Fong, *J. Mater. Sci.*, 2014, **49**, 463–480.
- 72 C. S. Sharma, R. Vasita, D. K. Upadhyay, A. Sharma, D. S. Katti and R. Venkataraghavan, *Ind. Eng. Chem. Res.*, 2010, **49**, 2731–2739.

- 73 G. M. Jenkins and K. Kawamura, *Nature*, 1971, **231**, 175–176.
- 74 R. E. Franklin, *Proc. R. Soc. London A Math. Phys. Eng. Sci.*, 1951, **209**, 196–218.
- 75 P. J. F. Harris, *J. Mater. Sci.*, 2013, **48**, 565–577.
- 76 T. W. Odom, J. L. Huang and C. M. Lieber, *J. Phys. - Condens. Matter*, 2002, **14**, R145.
- 77 M. Madou and S. Sharma, *Bioinspired, Biomim. Nanobiomaterials*, 2012, **1**, 252–265.
- 78 M. J. Madou, V. Perez-Gonzalez and B. Pramanick, *Carbon: The Next Silicon?: Book 1-Fundamentals*, Momentum Press, 2016.
- 79 J. K. Steach, J. E. Clark and S. V. Olesik, *J. Appl. Polym. Sci.*, 2010, **118**, 405–412.
- 80 E. C. S. Transactions and T. E. Society, 2016, **72**, 125–134.
- 81 M. Kurek, F. K. Larsen, P. E. Larsen, S. Schmid, A. Boisen and S. S. Keller, *Sensors*, 2016, **16**, 1–11.
- 82 C. S. Sharma, A. Sharma and M. Madou, *Langmuir*, 2010, **26**, 2218–2222.
- 83 S. Sharma, A. Khalajhedayati, T. J. Rupert and M. J. Madou, *ECS Trans.*, 2014, **61**, 75–84.
- 84 C. S. Sharma, H. Katepalli, A. Sharma and M. Madou, *Carbon N. Y.*, 2011, **49**, 1727–1732.
- 85 W. S. Lee, Y.-S. Park and Y.-K. Cho, *ACS Appl. Mater. Interfaces*, 2014, **6**, 12189–12195.
- 86 Y. Chen, M. Yue, Z. H. Huang and F. Kang, *Chem. Eng. J.*, 2014, **252**, 30–37.
- 87 B. M. Eick and J. P. Youngblood, *J. Mater. Sci.*, 2009, **44**, 160–165.
- 88 H. A. Liu and K. J. Balkus, *Mater. Lett.*, 2009, **63**, 2361–2364.
- 89 C. Niu, J. Meng, X. Wang, C. Han, M. Yan, K. Zhao, X. Xu, W. Ren, Y. Zhao, L. Xu, Q. Zhang, D. Zhao and L. Mai, *Nat. Commun.*, 2015, **6**, 7402.
- 90 H. Xu, X. Hu, Y. Sun, W. Luo, C. Chen, Y. Liu and Y. Huang, *Nano Energy*, 2014, **10**, 163–171.
- 91 L. Ji and X. Zhang, *Electrochem. commun.*
- 92 Z.-L. Xu, B. Zhang, Z.-Q. Zhou, S. Abouali, M. Akbari Garakani, J. Huang, J.-Q. Huang and J.-K. Kim, *RSC Adv.*, 2014, **4**, 22359–22366.
- 93 Y. Chen, X. Li, K.-S. Park, J. Hong, J. Song, L. Zhou, Y.-W. Mai, H. Huang and J.

- B. Goodenough, *J. Mater. Chem. A*, 2014, **2**, 10126.
- 94 Q. Lu, G. S. Hutchings, Y. Zhou, H. L. Xin, H. Zheng and F. Jiao, *J. Mater. Chem. A*, 2014, **2**, 6368–6373.
- 95 Y. Bai, C. Wu, R. Xu, F. Wu, Y. Liu, H. Li, Y. Li, J. Lu and K. Amine, .
- 96 B. Pant, H. R. Pant, M. Park, Y. Liu, J. W. Choi, N. A. M. Barakat and H. Y. Kim, *Catal. Commun.*, 2014, **50**, 63–68.
- 97 J. Mitra, S. Jain, A. Sharma and B. Basu, *Carbon N. Y.*, 2013, **65**, 140–155.
- 98 C. M. Lentz, B. A. Samuel, H. C. Foley and M. A. Haque, *J. Nanomater.*, 2011, **2011**, 9:1--9:8.
- 99 P. J. F. Harris, *Int. Mater. Rev.*, 1997, **42**, 206–218.
- 100 Z. Wang, Z. Lu, Y. Huang, R. Xue, X. Huang and L. Chen, *J. Appl. Phys.*
- 101 G. Canton, L. Kulinsky and M. J. Madou, *Proc. - Int. Symp. Adv. Packag. Mater.*, 2013, **4**, 230–239.
- 102 A. W. COATS and J. P. REDFERN, *Analyst*, 1963, **88**, 906–924.
- 103 A. Singh, J. Jayaram, M. Madou and S. Akbar, *J. Electrochem. Soc.*, 2002, **149**, 78–83.
- 104 T. Takeichi, Y. Eguchi, Y. Kaburagi, Y. Hishiyama and M. Inagaki, *Carbon N. Y.*, 1999, **37**, 569–575.
- 105 MicroChem Corporation, SU-8 2000.5-2015 datasheet,  
[http://www.microchem.com/pdf/SU-82000DataSheet2000\\_5thru2015Ver4.pdf](http://www.microchem.com/pdf/SU-82000DataSheet2000_5thru2015Ver4.pdf).
- 106 MicroChem Corporation, SU-8 2025-2075 datasheet, <http://microchem.com/pdf/SU-82000DataSheet2025thru2075Ver4.pdf>.
- 107 G. Von Freymann, A. Ledermann, M. Thiel, I. Staude, S. Essig, K. Busch and M. Wegener, *Adv. Funct. Mater.*, 2010, **20**, 1038–1052.
- 108 M. Malinauskas, M. Farsari, A. Piskarskas and S. Juodkazis, *Phys. Rep.*, 2013, 533, 1–31.
- 109 M. Deubel, G. von Freymann, M. Wegener, S. Pereira, K. Busch and C. M. Soukoulis, *Nat. Mater.*, 2004, **3**, 444–7.
- 110 H.-B. Sun, S. Matsuo and H. Misawa, *Appl. Phys. Lett.*, 1999, **74**, 786–788.
- 111 J. Serbin, A. Egbert, A. Ostendorf, B. N. Chichkov, R. Houbertz, G. Domann, J. Schulz, C. Cronauer, L. Fröhlich and M. Popall, *Opt. Lett.*, 2003, **28**, 301.

- 112 M. Deubel, M. Wegener, A. Kaso and S. John, *Appl. Phys. Lett.*, 2004, **85**, 1895–1897.
- 113 K. K. Seet, V. Mizeikis, K. Kannari, S. Juodkazis, H. Misawa, N. Tétreault and S. John, *IEEE J. Sel. Top. Quantum Electron.*, 2008, **14**, 1064–1073.
- 114 K. K. Seet, V. Mizeikis, S. Matsuo, S. Juodkazis and H. Misawa, *Adv. Mater.*, 2005, **17**, 541–545.
- 115 M. Thiel, M. Decker, M. Deubel, M. Wegener, S. Linden and G. von Freymann, *Adv. Mater.*, 2007, **19**, 207–210.
- 116 M. Thiel, M. S. Rill, G. Von Freymann and M. Wegener, *Adv. Mater.*, 2009, **21**, 4680–4682.
- 117 A. Ledermann, L. Cademartiri, M. Hermatschweiler, C. Toninelli, G. a Ozin, D. S. Wiersma, M. Wegener and G. von Freymann, *Nat. Mater.*, 2006, **5**, 942–945.
- 118 K. S. Lee, R. H. Kim, D. Y. Yang and S. H. Park, *Prog. Polym. Sci.*, 2008, **33**, 631–681.
- 119 C. N. LaFratta, J. T. Fourkas, T. Baldacchini and R. A. Farrer, *Angew. Chemie - Int. Ed.*, 2007, **46**, 6238–6258.
- 120 L. Li and J. T. Fourkas, *Mater. Today*, 2007, **10**, 30–37.
- 121 M. Rumi, S. Barlow, J. Wang, J. W. Perry and S. R. Marder, *Adv. Polym. Sci.*, 2008, **213**, 1–95.
- 122 J. Fischer and M. Wegener, *Laser Photonics Rev.*, 2013, **7**, 22–44.
- 123 Y. Cao, Z. Gan, B. Jia, R. A. Evans and M. Gu, *Opt. Express*, 2011, **19**, 19486.
- 124 J. T. Fourkas and J. S. Petersen, *Phys. Chem. Chem. Phys. Phys. Chem. Chem. Phys.*, 2014, **16**, 8731–8750.
- 125 S. Ushiba, S. Shoji, K. Masui, J. Kono and S. Kawata, *Adv. Mater.*, 2014, **26**, 5653–5657.
- 126 I. Testa, E. D’Este, N. T. Urban, F. Balzarotti and S. W. Hell, *Nano Lett.*, 2015, **15**, 103–106.
- 127 R. Wollhofen, J. Katzmüller, C. Hrelescu, J. Jacak and T. A. Klar, *Opt. Express*, 2013, **21**, 10831–40.
- 128 J. Fischer and M. Wegener, *Adv. Mater.*, DOI:10.1002/adma.201103758.
- 129 L. Li, R. R. Gattass, E. Gershgoren, H. Hwang and J. T. Fourkas, *Science (80-. ).*,

- 2009, **324**, 910–913.
- 130 T. F. Scott, B. A. Kowalski, A. C. Sullivan, C. N. Bowman and R. R. McLeod, *Science*, 2009, **324**, 913–917.
- 131 W.-E. Lu, X.-Z. Dong, W.-Q. Chen, Z.-S. Zhao and X.-M. Duan, *J. Mater. Chem.*, 2011, **21**, 5650.
- 132 I. Sakellari, E. Kabouraki, D. Gray, V. Purlys, C. Fotakis, A. Pikulin, N. Bityurin, M. Vamvakaki and M. Farsari, *ACS Nano*, 2012, **6**, 2302–2311.
- 133 R. W. Boyd, *Nonlinear Optics*, Academic Press, 2008.
- 134 E. G. Gamaly, S. Juodkazis, V. Mizeikis, H. Misawa, A. V. Rode and W. Krolikowski, *Phys. Rev. B - Condens. Matter Mater. Phys.*, , DOI:10.1103/PhysRevB.81.054113.
- 135 M. Drobizhev, A. Karotki, A. Rebane and C. W. Spangler, *Opt. Lett.*, 2001, **26**, 1081–1083.
- 136 E. G. Gamaly, S. Juodkazis, K. Nishimura, H. Misawa, B. Luther-Davies, P. Nicolai and V. T. Tikhonchuk, *Phys. Rev. B - Condens. Matter Mater. Phys.*, 2006, **73**, 214101.
- 137 K. S. Lee, D. Y. Yang, S. H. Park and R. H. Kim, *Polym. Adv. Technol.*, 2006, **17**, 72–82.
- 138 I. Wang, M. Bouriau, P. L. Baldeck, C. Martineau and C. Andraud, *Opt. Lett.*, 2002, **27**, 1348–1350.
- 139 S. Juodkazis, V. Mizeikis, K. K. Seet, M. Miwa and H. Misawa, *Nanotechnology*, 2005, **16**, 846.
- 140 C. Eschenbaum, 2016.
- 141 T. Woggon, T. Kleiner, M. Punke and U. Lemmer, 2009, **17**, 211–217.
- 142 T. Woggon, 2011.
- 143 H. B. Sun, K. Takada, M. S. Kim, K. S. Lee and S. Kawata, *Appl. Phys. Lett.*, 2003, **83**, 1104–1106.
- 144 D. B. Burckel, C. M. Washburn, A. K. Raub, S. R. J. Brueck, D. R. Wheeler, S. M. Brozik and R. Polsky, *Small*, 2009, **5**, 2792–2796.
- 145 S. H. Lee, J. H. Sung and T. H. Park, *Ann. Biomed. Eng.*, 2012, **40**, 1384–1397.
- 146 S. Hosseini, F. Ibrahim, I. Djordjevic and L. H. Koole, *Analyst*, 2014, **139**, 2933–43.

- 147 Y. Liu, H. Wang, J. Huang, J. Yang, B. Liu and P. Yang, *Anal. Chim. Acta*, 2009, **650**, 77–82.
- 148 J. M. Goddard and J. H. Hotchkiss, *Prog. Polym. Sci.*, 2007, **32**, 698–725.
- 149 C. Eaborn, *J. Organomet. Chem.*, 1988, 356, C76–C77.
- 150 A. W. Adamson and A. P. Gast, *Physical chemistry of surfaces*, Interscience New York, 1967.
- 151 W. Feng and P. Ji, *Biotechnol. Adv.*, 2011, **29**, 889–895.
- 152 A. Peigney, C. Laurent, E. Flahaut, R. R. Bacsa and A. Rousset, *Carbon N. Y.*, 2001, **39**, 507–514.
- 153 A. K. Wanekaya, W. Chen, N. V. Myung and A. Mulchandani, *Electroanalysis*, 2006, 18, 533–550.
- 154 S. Cagnin, M. Caraballo, C. Guiducci, P. Martini, M. Ross, M. Santaana, D. Danley, T. West and G. Lanfranchi, *Sensors (Basel)*., 2009, **9**, 3122–48.
- 155 I. Sherrington and E. H. Smith, *Precis. Eng.*, 1986, **8**, 79–87.
- 156 D. Whitehouse, in *Surfaces and Their Measurement*, 2002, pp. 48–95.
- 157 N. Faucheuix, R. Schweiss, K. Lützow, C. Werner and T. Groth, *Biomaterials*, 2004, **25**, 2721–2730.
- 158 S. Hosseini and F. Ibrahim, 2016, pp. 23–37.
- 159 D. J. Kim, J. M. Lee, J. G. Park and B. G. Chung, *Biotechnol. Bioeng.*, 2011, **108**, 1194–1202.
- 160 J. Rafiee, X. Mi, H. Gullapalli, A. V. Thomas, F. Yavari, Y. Shi, P. M. Ajayan and N. a. Koratkar, *Nat. Mater.*, 2012, **11**, 217–222.
- 161 C. Gao, H. He, L. Zhou, X. Zheng and Y. Zhang, *Chem. Mater.*, 2009, **21**, 360–370.
- 162 P. Jonkheijm, D. Weinrich, H. Schröder, C. M. Niemeyer and H. Waldmann, *Angew. Chemie - Int. Ed.*, 2008, 47, 9618–9647.
- 163 S. Hosseini and F. Ibrahim, *Novel Polymeric Biochips for Enhanced Detection of Infectious Diseases*, Springer Singapore, Singapore, 2016.
- 164 G. T. Hermanson, in *Bioconjugate Techniques*, 2013, pp. 229–258.
- 165 Y. Bai, C. G. Koh, M. Boreman, Y.-J. Juang, I.-C. Tang, L. J. Lee and S.-T. Yang, *Langmuir*, 2006, **22**, 9458–9467.
- 166 E. D. Glowacki, M. Irimia-Vladu, S. Bauer and N. S. Sariciftci, *J. Mater. Chem. B*,

- 2013, **1**, 3742–3753.
- 167 E. Sahin, A. O. Grillo, M. D. Perkins and C. J. Roberts, *J Pharm Sci*, 2010, **99**, 4830–4848.
- 168 T. Steiner, *Angew. Chem. Int. Ed.*, 2002, **41**, 49–76.
- 169 E. Arunan, G. R. Desiraju, R. A. Klein, J. Sadlej, S. Scheiner, I. Alkorta, D. C. Clary, R. H. Crabtree, J. J. Dannenberg, P. Hobza, H. G. Kjaergaard, A. C. Legon, B. Mennucci and D. J. Nesbitt, *Pure Appl. Chem*, 2011, **83**, 1637–1641.
- 170 J.-Y. Yoon, H.-Y. Park, J.-H. Kim and W.-S. Kim, *J. Colloid Interface Sci.*, 1996, **177**, 613–620.
- 171 N. T. Southall, K. A. Dill and A. D. J. Haymet, *J. Phys. Chem. B*, 2002, **106**, 521–533.
- 172 W. Xue and T. Cui, *Sensors Actuators, B Chem.*, 2008, **134**, 981–987.
- 173 Y. Weizmann, D. M. Chenoweth and T. M. Swager, *J. Am. Chem. Soc.*, 2010, **132**, 14009–14011.
- 174 Y. Weizmann, D. M. Chenoweth and T. M. Swager, *J. Am. Chem. Soc.*, 2011, **133**, 3238–41.
- 175 X. Kang, J. Wang, H. Wu, I. A. Aksay, J. Liu and Y. Lin, *Biosens. Bioelectron.*, 2009, **25**, 901–905.
- 176 J. H. Jung, D. S. Cheon, F. Liu, K. B. Lee and T. S. Seo, *Angew. Chem. Int. Ed. Engl.*, 2010, **49**, 5708–11.
- 177 W. S. Hummers and R. E. Offeman, *J. Am. Chem. Soc.*, 1958, **80**, 1339–1339.
- 178 M. Loos, J. Nahorny and L. Fontana, *Curr. Org. Chem.*, 2013, **17**, 1880–1893.
- 179 Q. D. Chen, L. M. Dai, M. Gao, S. M. Huang and a Mau, *J. Phys. Chem. B*, 2001, **105**, 618–622.
- 180 H. Yasuda, *Radiat. Phys. Chem.*, 1977, **9**, 805–817.
- 181 U. Vohrer, N. P. Zschoerper, Y. Koehne, S. Langowski and C. Oehr, in *Plasma Processes and Polymers*, 2007, vol. 4.
- 182 C. H. Tseng, C. C. Wang and C. Y. Chen, *Chem. Mater.*, 2007, **19**, 308–315.
- 183 M. A. Ali, K. Mondal, Y. Jiao, S. Oren, Z. Xu, A. Sharma and L. Dong, *ACS Appl. Mater. Interfaces*, 2016, **8**, 20570–20582.
- 184 M. J. Moghaddam, S. Taylor, M. Gao, S. Huang, L. Dai and M. J. McCall, *Nano*

- Lett.*, 2004, **4**, 89–93.
- 185 C. R. Martinez and B. L. Iverson, *Chem. Sci.*, 2012, **3**, 2191.
- 186 M. Zheng, A. Jagota, E. D. Semke, B. A. Diner, R. S. Mclean, S. R. Lustig, R. E. Richardson and N. G. Tassi, *Nat. Mater.*, 2003, **2**, 338–342.
- 187 C. Li, M. Curreli, H. Lin, B. Lei, F. N. Ishikawa, R. Datar, R. J. Cote, M. E. Thompson and C. Zhou, *J. Am. Chem. Soc.*, 2005, **127**, 12484–12485.
- 188 A. T. C. Johnson, S. M. Khamis, G. Preti, J. Kwak and A. Gelperin, *IEEE Sens. J.*, 2010, **10**, 159–166.
- 189 Y. Lu, B. R. Goldsmith, N. J. Kybert and A. T. C. Johnson, *Appl. Phys. Lett.*, 2010, **97**, 8–11.
- 190 W. Feng and P. Ji, *Biotechnol. Adv.*, 2011, **29**, 889–895.
- 191 Y. Yang, S. Qiu, X. Xie, X. Wang and R. K. Y. Li, *Appl. Surf. Sci.*, 2010, **256**, 3286–3292.
- 192 A. E. Jakus, E. B. Secor, A. L. Rutz, S. W. Jordan, M. C. Hersam and R. N. Shah, *ACS Nano*, 2015, **9**, 4636–4648.
- 193 S. Jain, A. Sharma and B. Basu, *J. Biomed. Mater. Res. B. Appl. Biomater.*, 2013, **101**, 520–31.
- 194 T. H. Kim, H. S. Song, H. J. Jin, S. H. Lee, S. Namgung, U. Kim, T. H. Park and S. Hong, *Lab Chip*, 2011, **11**, 2262–7.
- 195 T. H. Kim, S. H. Lee, J. Lee, H. S. Song, E. H. Oh, T. H. Park and S. Hong, *Adv. Mater.*, 2009, **21**, 91–94.
- 196 M. Pumera, *Mater. Today*, 2011, **14**, 308–315.
- 197 E. Morales-Narváez and A. Merkoçi, *Adv. Mater.*, 2012, **24**, 3298–3308.
- 198 E. C. Dandley, A. J. Taylor, K. S. Duke, M. D. Ihrie, K. A. Shipkowski, G. N. Parsons and J. C. Bonner, *Part. Fibre Toxicol.*, 2015, **13**, 29.
- 199 D. B. Farmer and R. G. Gordon, *Nano Lett.*, 2006, **6**, 699–703.
- 200 D. M. King, X. Liang and A. W. Weimer, *Powder Technol.*, 2012, **221**, 13–25.
- 201 S. M. George, *Chem. Rev.*, 2010, **110**, 111–131.
- 202 R. J. Narayan, S. P. Adiga, M. J. Pellin, L. a Curtiss, A. J. Hryni, S. Stafslien, B. Chisholm, C.-C. Shih, C.-M. Shih, S.-J. Lin, Y.-Y. Su, C. Jin, J. Zhang, N. a Monteiro-Riviere and J. W. Elam, *Philos. Trans. A. Math. Phys. Eng. Sci.*, 2010,

- 368**, 2033–2064.
- 203 Y. Nakashima, Y. Ohno, S. Kishimoto, M. Okochi, H. Honda and T. Mizutani, in *2007 Digest of papers Microprocesses and Nanotechnology*, IEEE, 2007, pp. 488–489.
- 204 I. Park, Z. Li, A. P. Pisano and R. S. Williams, *Nano Lett.*, 2007, **7**, 3106–3111.
- 205 B. D. Sosnowchik, L. Lin and O. Englander, *J. Appl. Phys.*, 2010, **107**, 51101.
- 206 T. Li, W. Hu and D. Zhu, *Adv. Mater.*, 2010, **22**, 286–300.
- 207 X. Chen, Z. Guo, G. M. Yang, J. Li, M. Q. Li, J. H. Liu and X. J. Huang, *Mater. Today*, 2010, **13**, 28–41.
- 208 A. Cui, H. Dong and W. Hu, *Small*, 2015, **11**, 6115–6141.
- 209 A. Kuzyk, *Electrophoresis*, 2011, **32**, 2307–2313.
- 210 A. Fursina, S. Lee, R. G. S. Sofin, I. V. Shvets and D. Natelson, *Appl. Phys. Lett.*, , DOI:10.1063/1.2895644.
- 211 S. Roy, H. Vedala, A. D. Roy, D.-H. Kim, M. Doud, K. Mathee, H. Shin, N. Shimamoto, V. Prasad and W. Choi, *Nano Lett.*, 2008, **8**, 26–30.
- 212 D. Cheon, S. Kumar and G. H. Kim, *Appl. Phys. Lett.*, , DOI:10.1063/1.3280859.
- 213 T. Nagase, K. Gamo, T. Kubota and S. Mashiko, *Thin Solid Films*, 2006, **499**, 279–284.
- 214 W. Lee, K. Kim, W. Jeong, L. A. Zotti, F. Pauly, J. C. Cuevas and P. Reddy, *Nature*, 2013, **498**, 209–212.
- 215 D. R. Strachan, D. E. Smith, D. E. Johnston, T. H. Park, M. J. Therien, D. A. Bonnell and A. T. Johnson, *Appl. Phys. Lett.*, 2005, **86**, 43109.
- 216 M. L. Perrin, C. J. O. Verzijl, C. a. Martin, A. J. Shaikh, R. Eelkema, J. H. Van Esch, J. M. van Ruitenbeek, J. M. Thijssen, H. S. J. van der Zant and D. Dulić, *Nat. Nanotechnol.*, 2013, **advance on**, 282–287.
- 217 D. J. Beesley, J. Semple, L. Krishnan Jagadamma, A. Amassian, M. a McLachlan, T. D. Anthopoulos and J. C. deMello, *Nat. Commun.*, 2014, **5**, 3933.
- 218 C. Thiele, M. Engel, F. Hennrich, M. M. Kappes, K. P. Johnsen, C. G. Frase, H. V. Lhneysen and R. Krupke, *Appl. Phys. Lett.*, , DOI:10.1063/1.3656736.
- 219 J. H. Kim, H. Moon, S. Yoo and Y. K. Choi, *Small*, 2011, **7**, 2210–2216.
- 220 S. Kubatkin, A. Danilov, M. Hjort, J. Cornil, J.-L. Brédas, N. Stuhr-Hansen, P.

- Hedegård and T. Bjørnholm, *Nature*, 2003, **425**, 698–701.
- 221 H. Zhang, S. W. Chung and C. A. Mirkin, *Nano Lett.*, 2003, **3**, 43–45.
- 222 C. W. Marquardt, S. Grunder, A. Błaszczyk, S. Dehm, F. Hennrich, H. v. Löhneysen, M. Mayor and R. Krupke, *Nat. Nanotechnol.*, 2010, **5**, 863–867.
- 223 J. Y. Huang, S. Chen, Z. F. Ren, G. Chen and M. S. Dresselhaus, *Nano Lett.*, 2006, **6**, 1699–1705.
- 224 H. Kitsuki, T. Yamada, D. Fabris, J. R. Jameson, P. Wilhite, M. Suzuki and C. Y. Yang, *Appl. Phys. Lett.*, 2008, **92**, 173110.
- 225 T. Saito, T. Yamada, D. Fabris, H. Kitsuki, P. Wilhite, M. Suzuki and C. Y. Yang, *Appl. Phys. Lett.*, 2008, **93**, 102108.
- 226 Y. S. Virgil&apos;ev and I. G. Lebedev, *Inorg. Mater.*, 2002, **38**, 668–673.
- 227 C. Yu, S. Saha, J. Zhou, L. L. Shi, A. M. A. M. Cassell, B. A. B. a. Cruden, Q. Ngo and J. Li, *J. Heat Transfer*, 2006, **128**, 234–239.
- 228 M. Balat-Pichelin, J. F. Robert and J. L. Sans, *Appl. Surf. Sci.*, 2006, **253**, 778–783.
- 229 A. Barreiro, F. Börrnert, M. H. Rümmeli, B. Büchner and L. M. K. Vandersypen, *Nano Lett.*, 2012, **12**, 1873–1878.
- 230 J. Y. Huang, F. Ding, B. I. Yakobson, P. Lu, L. Qi and J. Li, *Proc. Natl. Acad. Sci.*, 2009, **106**, 10103–10108.
- 231 M. Suzuki, Y. Ominami, Q. Ngo, C. Y. Yang, A. M. Cassell and J. Li, *J. Appl. Phys.*, 2007, **101**, 114307.
- 232 C. H. Jin, J. Y. Wang, Q. Chen and L. M. Peng, *J. Phys. Chem. B*, 2006, **110**, 5423–5428.
- 233 B. Y. Park, L. Taherabadi, C. Wang, J. Zoval and M. J. Madou, *J. Electrochem. Soc.*, 2005, **152**, J136.
- 234 C. M. Lentz, B. A. Samuel, H. C. Foley and M. A. Haque, *J. Nanomater.*, 2011, **2011**, 1–8.
- 235 A. Tibrewala, E. Peiner, R. Bandorf, S. Biehl and H. Lüthje, *Appl. Surf. Sci.*, 2006, **252**, 5387–5390.
- 236 G. E. Begtrup, K. G. Ray, B. M. Kessler, T. D. Yuzvinsky, H. Garcia and A. Zettl, *Phys. Rev. Lett.*, 2007, **99**, 155901.
- 237 F. P. Bundy, *Phys. A Stat. Mech. its Appl.*, 1989, **156**, 169–178.

## Appendix A

### *MatLab routine for CNW diameter measurement*

```
clear all;
close all;

%% Objetivo del programa
% Detectar una estructura nanométrica(nanofibra de carbono) en una
% micrografía SEM (scanning electron microscopy) para caracterizarlas
% geométricamente de manera automática.

%% Aplicación y relevancia del problema:

% La medición de objetos desde micrografías SEM tiene una gran relevancia
% para la caracterización de estructuras en esas escalas micro/nano-métricas.
% A pesar de que se cuenta con estos equipos de alta resolución,
% la interpretación de dichas imágenes muchas veces depende del tiempo
% disponible del microscopista para su análisis, su percepción y criterio.
% Una de estas tareas incluye la medición del diámetro de estructuras
% como nanofibras, la cual es de suma importancia para definir sus
% aplicaciones en la ciencia. La medición de dichas distancias conlleva un
% error humano por los factores mencionados anteriormente.

% Por lo anterior, es importante el desarrollo de una rutina computacional
% que realice un procesamiento de las imágenes obtenidas, a fin segmentar
% la imagen para resaltar la estructura nanométrica de interés y
% automatizar la tarea de medición. Esto reducirá el error humano, y
% aumentará la fidelidad de los datos de medición obtenidos.

%% Objetivos de Programación:

%1) Crear un algoritmo que obtenga como entrada una micrografía .tif y logre
%   generar una salida (x,y) tipo impulso en la que se tenga un 1 donde se
%   encuentra el objeto de interés y un 0 donde no se encuentre.

%2) Deterctar el perímetro de dicha estructura para indicar la presencia de
%la estructura de interés.

%3) Utilizar este resultado para realizar una medición de la orientación
% (ángulo) y diámetro de la estructura.

%% Paso 1: Abrir el archivo de imagen y convertir a grises:

% direc = 'C:\Users\Braulio\Desktop\Proyecto Medio Termino Mate\TestImages\' ;
% Para las imágenes de test
% direc = 'C:\Users\Braulio\Desktop\Fibras Con Marca Zoom\' ;

% Número de muestra:
sampleNum = '1' ;
```

```

% Nombre del archivo completo:
% filename = ['F' sampleNum '.tif'];
% filename = ['c5f' '.jpg'];
% filename = ['theta45' '.tif'];
% filename = 'NW31-5.tif';

filename = 'Curso007.tif';

% Index del vector de escala que se va a utilizar corresponde al num. de
% muestra:

sampleIdx = str2double(sampleNum);

% Este vector contiene los pixeles de la escala de medición:
pixsc=[86,824,824,824,824,824,989,989,824,1098,824,989,550,824,550];
% Este vector contiene las mircas que mide la escala:
microns=[1,3,3,3,3,5,3,3,2,1,3,3,1,2,1];

% Razón de la escala de cada muestra:
micron2pixelRatio=microns./pixsc;

% Imagen original:
% Iorig = imread([pwd direc filename]);
Iorig = imread([pwd '\TestImages\' filename]);

% Se despliega la imagen original:

% Conversión a escala de grises:
% Igray = rgb2gray(Iorig); %IF NOT IN GRayscale

[Iorig,map] = imread([pwd '\TestImages\' filename]);
if ~isempty(map)
    Im = ind2rgb(Iorig,map);
end

% Igray = Iorig;
Igray = rgb2gray(Im);

figure, imshow(Im), title('Original Image');

%% Paso 2: Crop básico de la imagen para eliminar datos de la escala:

% Ix = Igray(300:end-300,1:end);

% Primero hacemos el recorte y lo guardamos en Ix:
Ix = Igray(1:end-185,1:end); %
%
% Ix = Igray;

% Luego guardamos esa versión y la dejaremos intacta hasta el final:
% El archivo que manejaremos será Ix, y Icropped se usará para efectos de

```

```

% visualización:

Icropped = double(Ix);

%% Paso 3: Filtro Gaussiano de la imagen:

% Para eliminar el ruido de la imagen, hacemos un filtrado gaussiano de 5x5

% i) declaramos la matriz gaussiana:

B = (1/159)*[2 4 5 4 2; 4 9 12 9 4; 5 12 15 12 5; 4 9 12 9 4; 2 4 5 4 2];

% ii) Luego convolucionamos dicha matriz con nuestra imagen recortada:

Ix = conv2(B,double(Ix));

% Desplegamos el resultado:

figure,imshow(Ix,[]), title('Cropped and Filtered Image');

%% Paso 4: Convolución con matriz derivada (Sobel) para resaltar bordes:

% Ahora aplicamos un operador de derivada sobre la imagen filtrada. Esto se
% hace utilizando la matriz de transferencia tipo Sobel:

% Llamamos a la subrutina Sobel, que nos devuelve nuestra misma imagen con
% sus bordes resaltados:

[Mx,My] = Sobel(Ix);

% La respuesta de llamar Sobel(imagen) es que nos regresa la matriz Mx con
% bordes horizontales resaltados y la matriz My con bordes verticales
% resaltados. Para sacar la magnitud de los bordes, se elevan al cuadrado
% estas componenentes y se obtiene la raíz cuadrada del resultado:

Mag = sqrt(Mx.^2 + My.^2);

% Desplegamos el resultado de esta operación:

figure, imshow(Mag,[]), title('Sobel M magnitude');

%% Paso 5: Threshold de la matriz de magnitudes Sobel:

% Algunos bordes no tienen intensidad suficiente para ser considerados el
% borde principal de interés. Se procede a eliminar aquellos bordes cuya
% intensidad sea menor al 10% de la máxima intensidad de la imagen de
% bordes:

M = (Mag>=0.05*max(max(Mag))) ;

% El resultado es una imagen binaria (1's y 0's) de los valores que cumplen
% y no cumplen esta restricción.

```

```

% Resultado:

figure, imshow(M, []), title('Thresholded Sobel Matrix');

%% Paso 6: Delineado del cuadro de trabajo:

% Si se observan las figuras de las fibras, se notará que no se pueden
% apreciar los extremos de la fibra, es decir, contamos únicamente con dos
% bordes idealmente paralelos que van a lo largo de nuestro fotograma
% rectangular. El objetivo final de nuestro programa es segmentar la imagen
% para generar una respuesta impulso (1's y 0's) donde se encuentre la
% figura de interés. Por lo anterior, es necesario realizar cerrar la
% imagen en los extremos, colocando un perímetro de 1's en el recuadro de la
% imagen
% De esta forma se va a poder llenar la imagen con 1's a partir de su
% perímetro.

% Colocando 1's en el margen (10pixeles en cada arista):
M(1:10,:) = 1;
M(end-10:end,:)= 1;
M(:,1:10) = 1;
M(:,end-10:end) = 1;

% A fin de que el algoritmo no rellene las estructuras que quedan arriba
% y abajo de la fibra, se abren las esquinas de la figura colocando
% cuadros de 0's (20x20 pixeles). De esta forma, no se llenarán las
% figuras de arriba y abajo.

M(1:20,1:20) = 0;
M(end-20:end,end-20:end) = 0;
M(1:20,end-20:end) = 0;
M(end-20:end,1:20) = 0;

%% Paso 7: Eliminación de figuras cerradas pequeñas y relleno de la imagen
binaria:

% A pesar de realizar la segmentación, quedarán estructuras que no estén
% conectadas con nuestra imagen de interés (puntos, basura, etc).
% Se pueden eliminar dichas estructuras borrando las figuras dentro de la
% imagen que sean más pequeñas que alguna cantidad. Utilizamos una rutina
% de matlab para realizar esta tarea, bwareaopen, la cual admite la imagen
% binaria M y elimina las estructuras conectadas con menos de 5000 pixeles

BW = bwareaopen(M, 5000); % El resultado se almacena en BW = black n' white

% Ahora se llenan las estructuras cerradas:

BWdfill = imfill(BW, 'holes'); % Se almacena en BWdfill = llenado

% Cuando terminamos esta tarea, ya no nos interesan los bordes blancos, así
% que los borramos colocando un 0:

```

```

BWdfill(1:10,:) = 0;
BWdfill(end-10:end,:) = 0;
BWdfill(:,1:10) = 0;
BWdfill(:,end-10:end) = 0;

% BWdfill = bwareaopen(BWdfill, 5000);

% Desplegamos el resultado:

figure, imshow(BWdfill, []), title('Filled Perimeter');

%% Paso 8: Ajuste del la imagen final

% Para suavisar el perímetro de la imagen obtenida, se utiliza la librería
% imerode de Matlab, la cual toma una imagen binaria y se erosiona dos veces
% con una estructura predefinida (en este caso, un diamante binario). El
% diamante se obtiene con la función strel de Matlab.

seD = strel('diamond',4);
se180 = strel('line',30,180);
se90 = strel('line',4,90);
BWdfill = imerode(BWdfill,se180);
BWdfill = imerode(BWdfill,se90);
BWfinal = imerode(BWdfill,seD);

% Luego obtenemos las dimensiones de la imagen final, pues estas han sido
% modificadas ligeramente por el algoritmo de convolución.

[Ypix,Xpix] = size(BWfinal);

% Borramos los extremos que fueron agregados por el algoritmo de conv2:

BWfinal([1,2,3,Ypix-2,Ypix-1,Ypix],:) = [];
BWfinal(:,[1,2,3, Xpix-2,Xpix-1 ,Xpix]) = [];

% Y presentamos el resultado final:

figure, imshow(BWfinal), title('segmented image');

% Dado que ya tenemos una estructura de la fibra en forma de rombo, nos
% interesa el contorno de esta figura para efectos de visualización:

% Por ello ,evaluamos el contorno del resultado final BWfinal con la
% librería bwperim:

BWoutline = bwperim(BWfinal);
% Para efectos de visualización, hacemos que los pixeles del contorno se
% hagan blancos en la imagen original recortada:

Segout = Icropped;
Icropped(BWoutline) = 255;

```

```

% Y mostramos el resultado:
figure,imshow(Icropped), title('Result (perimeter in white)');

%% Paso 9: Caracterización geométrica.

% Hasta el paso 9 ya se obtuvo la segmentación de la micrografía SEM,
% cumpliendo con los objetivos de programación 1 y 2. Ahora hace falta
% realizar las mediciones.

%% Obtención del centroide:

% usando la función de matlab regionprops, introducimos una imagen binaria
% y nos devuelve su centroide:

centroid = regionprops(BWfinal,'Centroid');

% Coordenadas del centroide: (deben redondearse para obtener los valores de
% los pixeles)

% [CauxX,CauxY]=centroid.Centroid;

Cx = round(centroid.Centroid(1));
Cy = round(centroid.Centroid(2));
clc;

%% Identificación de la orientación de la fibra:

% Una vez que contamos con el centroide, nos interesa saber el ángulo que
% hace la fibra con el eje horizontal. La función regionprops puede darnos
% dicho ángulo de orientación, sin embargo, las figuras que generamos no
% son simétricas con respecto a los ejes x y y del centroide. Para corregir
% esto y obtener el ángulo adecuado, segmentamos la imagen nuevamente
% haciendo una selección de un radio alrededor del centroide. La figura
% obtenida será simétrica respecto a los ejes del centroide y permitirá
% obtener el ángulo correctamente.

% 1) Indicamos el radio de corte:

% Se fijará este radio como 80% de la mitad de la dimensión de la foto en Y
Rad = 0.8*round(Ypix/2);

% Llamamos a la función realizada por nosotros radiusPixel, la cual toma
% imagen binaria final para medir sus dimensiones únicamente y luego genera
% un círculo de radio Rad, centrado en el pixel Cx, Cy de la imagen.

[bwnew] = radiusPixel(BWfinal,Cx,Cy,Rad);

% Se hace un AND entre este círculo y la imagen binaria que teníamos para
% segmentar la fibra en el radio de interés:

circleSample = (bwnew&BWfinal);

% Mostramos el resultado:

```

```

figure,imshow(circleSample), title('Circular Crop of Binary Image');

% Y finalmente calculamos correctamente la orientación con la función
% regionprops:

orientation = regionprops(circleSample,'Orientation');

% Extraemos el ángulo:
theta = orientation.Orientation

%% Centrado y Rotación de la imagen:

% Para medir el diámetro de la estructura, se rotó la imagen para eliminar
% el grado de orientación que tenía. Contando con una imagen binaria con
% orientación horizontal, la tarea de medir el diámetro se reduce a contar
% los pixeles que se tienen verticalmente.

% Primero centramos la imagen binaria usando la función imageCentering, la
% cual acepta una imagen y la centra desplazando la imagen a Xpix/2,Ypix/2

Sample = imageCentering(circleSample,Cx,Cy);

% Una vez centrada, se rota la imagen (usando el ángulo de orientación
% obtenido en negativo):

rotatedSample = imrotate(Sample,-theta);

% Desplegamos el resultado:

figure,imshow(rotatedSample), title('Centered and Rotated Circular Crop');

%% Medición del diámetro:

% Con la imagen rotada y centrada, contamos la cantidad de pixeles blancos
% verticalmente y esto nos dará el diámetro en pixeles de la imagen
% binaria. Usando la razón micron2pixelRatio, se convierte esta medida a
% micras:
% D = sum(rotatedSample);
D = sum(rotatedSample).*micron2pixelRatio(sampleIdx);

% Se despliega el diámetro en micras en función del eje horizontal (o bien,
% el eje que pasa por el centroide).

% Eje paralelo y que pasa por el centro de la fibra:
z = 1: numel(D);
% Centrado en el Cx,Cy:
Nhalf = round(numel(D)/2);
z = z-Nhalf;
% En micras:
z = z*micron2pixelRatio(sampleIdx);

```

```

%% Promedios y desviación estándar:

% Del procedimiento anterior se toman 1000 valores del diámetro para
% realizar un promedio y obtener la desviación estándar de la medición.

avgNumTotal = 500;

avgDiameter= mean(D(Nhalf-round(avgNumTotal/2):Nhalf+round(avgNumTotal/2)-1))

stdDiameter = std(D(Nhalf-round(avgNumTotal/2):Nhalf+round(avgNumTotal/2)-1))

% avgDiameter= mean(D(Nhalf-400:Nhalf+400-1))
%
% stdDiameter = std(D(Nhalf-400:Nhalf+400-1))

centralDiameter = D(round(numel(D)/2))

theta

RelativePercentError = 100*3/(avgDiameter/micron2pixelRatio(sampleIdx))

% %% PLOTTING:
figure;
hold all;
plot(z,D);

```